Department of Physics and Astronomy
Heidelberg University

Master's thesis
in
Physics
submitted by
Lennart Nikolai Resch
born in
Freiburg im Breisgau, Germany

2025

Evaluation of Ground-Based Spectral Imaging Capabilities for Detecting and Quantifying Landfill Methane Emissions

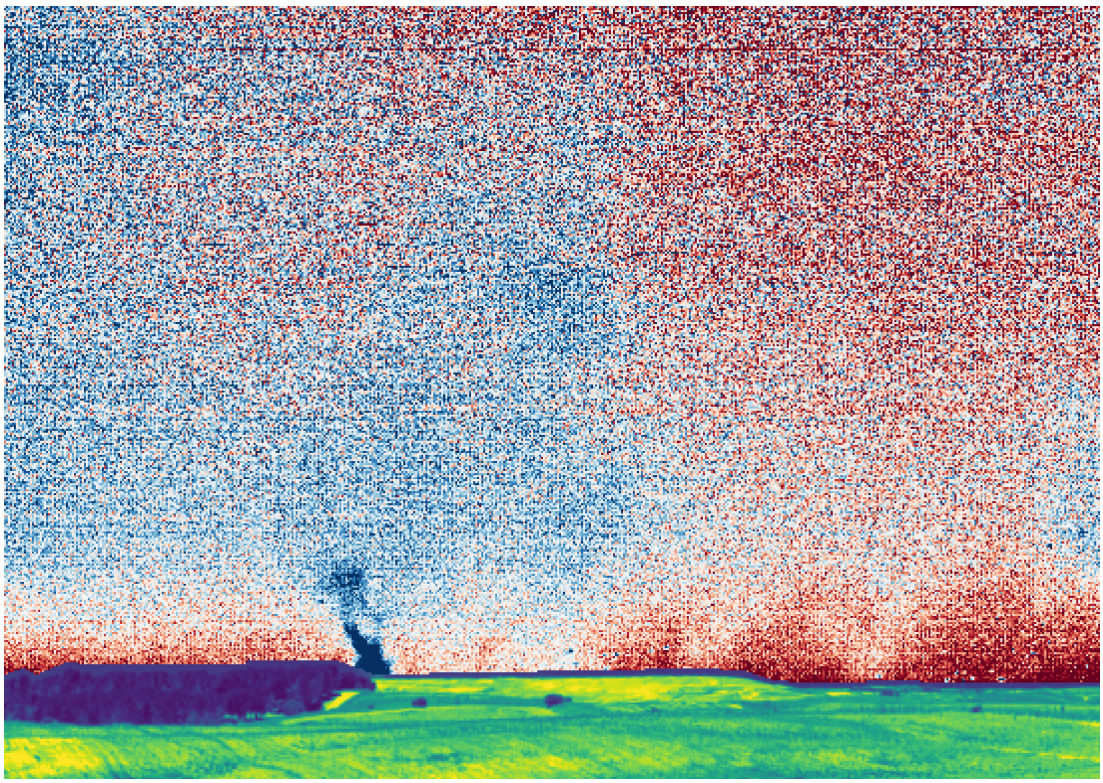

This master's thesis was carried out by

Lennart Nikolai Resch

at the

Institute of Environmental Physics

under the supervision of

Prof. Dr. André Butz

Abstract

Methane (CH_4) is the second most important anthropogenic greenhouse gas, contributing significantly to climate change. Landfills are major anthropogenic sources of methane, but these emissions are subject to significant uncertainty. Due to their substantial mitigation potential, accurate and independent detection and quantification of landfill methane emissions is vital for assessing emission mitigation efforts.

This thesis evaluates the capabilities of ground-based spectral imaging for detecting and quantifying the methane emissions of the Pinto landfill near Madrid, Spain. The Pinto landfill is one of the landfills with the largest methane emissions in Europe. Over the course of two weeks in the summer of 2024, hyperspectral images were collected from a distance of 2 km to 7 km and with a scanning frequency of approximately one minute. A matched filter was used to retrieve methane column enhancements from the 2.3-µm spectral region of these observations. Various matched filters were compared, and the lognormal matched filter (LMF) was found to perform best. Therefore, it was used for all retrievals in this thesis.

Diffuse enhanced methane concentrations were detected over the landfill on both days analyzed, with concentrations decreasing with altitude and increasing throughout the day. The hot and dry summer climate in Madrid causes a lot of dust in the atmosphere. Dust clouds shorten the light path and thus appear as negative methane enhancements, affecting the amount of detected methane in an image. Observing the movement of a dust cloud enables the calculation of the transport wind velocity. A one-box model was used to derive emission rates using wind data from a co-deployed wind lidar. There is a strong correlation between the emission rates and the wind velocity, indicating that the short-term emission rate variability stems from the wind variability and suggesting inaccuracies in the model. Temporally averaged emission rates range from $1\,\mathrm{t\,h^{-1}}$ to $5\,\mathrm{t\,h^{-1}}$ and are of the same order of magnitude as those found in previous studies and as those listed in emission registers, although uncertainties remain high.

Zusammenfassung

Methan (CH_4) ist das zweitwichtigste anthropogene Treibhausgas und trägt erheblich zum Klimawandel bei. Mülldeponien sind bedeutende anthropogene Methanquellen, allerdings sind diese Emissionen mit erheblichen Unsicherheiten behaftet. Aufgrund ihres beträchtlichen Minderungspotenzials ist eine genaue und unabhängige Erkennung und Quantifizierung der Methanemissionen von Deponien für die Bewertung von Emissionsminderungsmaßnahmen von entscheidender Bedeutung.

In dieser Arbeit wird das Potenzial der bodengestützten spektralen Bildgebung zur Erkennung und Quantifizierung der Methanemissionen der Mülldeponie Pinto bei Madrid in Spanien untersucht. Die Pinto-Deponie zählt zu den Deponien mit den höchsten Methanemissionen in Europa. Während zweier Wochen im Sommer 2024 wurden aus einer Entfernung von 2 km bis 7 km Hyperspektralbilder mit einer Scanfrequenz von etwa einer Minute aufgenommen. Mittels eines Optimalfilters wurden die Methansäulenüberhöhungen aus dem 2,3-µm-Spektralbereich dieser Aufnahmen ermittelt. Es wurden verschiedene Optimalfilter verglichen, wobei sich der lognormale Optimalfilter als am leistungsfähigsten erwies. Daher wurde dieser für alle Auswertungen in dieser Arbeit verwendet.

An beiden analysierten Tagen wurden über der Deponie diffuse erhöhte Methankonzentrationen festgestellt. Dabei nahmen die Konzentrationen mit zunehmender Höhe ab und im Laufe eines Tages zu. Das heiße und trockene Sommerklima in Madrid verursacht viel Staub in der Atmosphäre. Staubwolken verkürzen den Lichtweg, erscheinen daher als negative Methanüberhöhungen und beeinträchtigen so die Gesamtmenge des nachgewiesenen Methans in einem Bild. Durch die Beobachtung der Bewegung einer Staubwolke kann die Transportwindgeschwindigkeit ermittelt werden. Mithilfe eines Ein-Box-Modells und unter Verwendung von Winddaten eines gleichzeitig stationierten Wind-Lidars wurden Emissionsraten abgeleitet. Es besteht eine starke Korrelation zwischen den Emissionsraten und der Windgeschwindigkeit. Dies deutet darauf hin, dass die kurzfristigen Schwankungen der Emissionsraten auf Windschwankungen zurückzuführen sind und das Modell Ungenauigkeiten aufweist. Die zeitlich gemittelten Emissionsraten reichen von $1\,\mathrm{t\,h^{-1}}$ bis $5\,\mathrm{t\,h^{-1}}$ und liegen in der gleichen Größenordnung wie die in früheren Studien ermittelten und in Emissionsregistern aufgeführten Emissionsraten. Allerdings sind die Unsicherheiten weiterhin groß.

Contents

List of Abbreviations

CH_4	Methane
CO_2	Carbon dioxide
CMF	Classic matched filter
FOV	Field of view
FWHM	Full width at half maximum
ILMF	Iterative lognormal matched filter
ILS	Instrument line shape
LMF	Lognormal matched filter
PRTR-España	Spanish Register of Emissions and Pollutant Sources
RAA	Relative azimuth angle
RWL1MF	Reweighted $\ell 1$ matched filter
SNR	Signal-to-noise ratio
SSD	Spectral sampling distance
SWIR	Short wave infrared
SZA	Solar zenith angle
UAS	Unit absorption spectrum
USCB	Upper Silesian Coal Basin
VAA	Viewing azimuth angle
VEA	Viewing elevation angle
VZA	Viewing zenith angle

1 Introduction

Since the beginning of industrialization, humanity has released immense amounts of greenhouse gases into the atmosphere. Due to the greenhouse effect, this has caused a dramatic rise in the Earth's average temperature, which reached 1.09 °C during the period 2011–2020 compared to the reference period 1850–1900 (IPCC, 2021). In 2024, the 1.5 °C threshold established in the "Paris Agreement" (2015) was exceeded for the first time (Copernicus Climate Change Service, 2025). This temperature increase comes with many consequences, changing the atmosphere, ocean, cryosphere, and biosphere. It impacts people's lives all around the world, for example, by a rise in frequency of extreme weather events like heatwaves, droughts, and floods, making climate change mitigation a critical political issue (IPCC, 2021).

The two most important anthropogenic greenhouse gases driving this climate change are carbon dioxide (CO_2) and methane (CH_4). In 2023, their concentrations in the atmosphere reached (419.32 ± 0.10) ppm CO_2 (Lan et al., 2024a) and (1921.76 ± 0.46) ppb CH_4 (Lan et al., 2024b), compared to (278.3 ± 2.9) ppm CO_2 and (729.2 ± 9.4) ppb CH_4 in the preindustrial year of 1750 (Gulev et al., 2021). Their contributions to the total global warming are depicted in Fig. 1.1.

Methane contributes about 23% to the anthropogenic radiative forcing, which is the change in net radiative flux received by the Earth, quantified, e.g., in $\mathrm{W\,m^{-2}}$ (Etminan et al., 2016). While this is a lower absolute contribution to global warming than that of carbon dioxide, the global warming potential of methane is 81.2 for a 20-year time horizon and 27.9 for a 100-year time horizon, meaning the emission of 1 kg CH_4 contributes to the warming of the Earth as much as the emission of 81.2 kg CO_2 or 27.9 kg CO_2, respectively[1] (Smith et al., 2021). This is why undesired methane release, e.g., in the oil and gas industry, is often flared, converting the methane into carbon dioxide. If emitted into the atmosphere, most of the methane is broken down by reaction with hydroxyl radicals, and through a long chain of further reactions most carbon atoms will in the end be incorporated into a carbon dioxide molecule. The reaction of methane with a hydroxyl radical defines its lifetime, which is 11.8 years on average[2] (Smith et al., 2021).

[1] These numbers do not account for the carbon that enters the carbon cycle after the methane is broken down. Including this fact changes the numbers presented here by a few percent, depending on the methane source and model assumptions.

[2] This is the perturbation lifetime, which characterizes the decay of a one-time emission. The overturning time of a gas in the atmosphere is characterized by the global atmospheric lifetime, which is (9.1 ± 0.9) years for methane (Prather et al., 2012). The different durations are due to emitted methane adding to

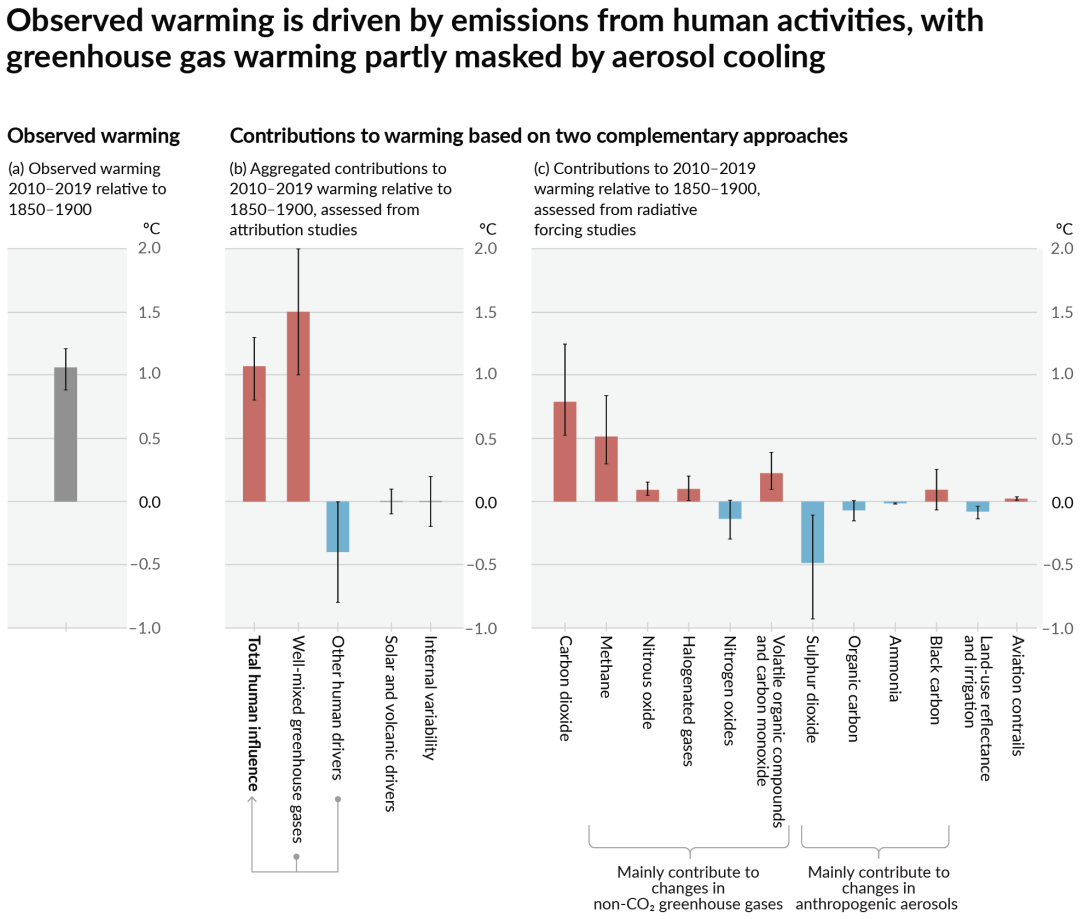

Fig. 1.1. (a) Observed average global warming 2010–2019 in relation to 1850–1900. (b) Different human and non-human contributions to this warming. (c) Contributions of greenhouse gases, aerosol-inducing chemicals, and other anthropogenic factors to global warming. Figure taken from IPCC, 2021.

This comparatively short lifetime is also the reason why methane has different global warming potentials when regarding different timescales.

Due to its relatively short lifetime, reducing methane emissions is an effective way to contribute to climate change mitigation in the short and medium term (Shindell et al., 2012). If no carbon dioxide were emitted from now on, the carbon dioxide concentration in the atmosphere would stay well above preindustrial levels for centuries (Solomon

the atmospheric methane concentration, which depletes the atmosphere in hydroxyl radicals, which, in turn, reduces the methane depletion rate and results in an increase of background methane (Denman et al., 2007).

et al., 2009)[3], whereas stopping methane emissions would result in a drastic reduction of atmospheric methane concentration in a matter of a few decades (Saunois et al., 2024), thus strongly reducing the radiative forcing.

From 2010 to 2019, global direct anthropogenic methane emissions amounted to $(358 \pm 29)\,\mathrm{Tg\,CH_4\,yr^{-1}}$, according to (Saunois et al., 2024). Of this, 19% ($69^{+11}_{-13}\,\mathrm{Tg\,CH_4\,yr^{-1}}$) came from the waste sector, which includes managed and non-managed landfills, as well as wastewater handling. There, methane is produced in the process of biological decomposition of the organic materials in the waste. Methane emissions from solid waste ranging from $37\,\mathrm{Tg\,CH_4\,yr^{-1}}$ to $42\,\mathrm{Tg\,CH_4\,yr^{-1}}$ are reported by the GAINS model and CEDS and EDGAR inventories for the year 2019. This corresponds to 10.3%–11.7% of total global direct anthropogenic methane emissions (Saunois et al., 2024).

In the United States, landfills were found to contribute almost 26% to the total direct anthropogenic methane emissions in 2014 (USEPA, 2016). In the European Union, the EU Landfill Directive (1999) imposes that no more than 10% of municipal solid waste may be landfilled by 2035. Additionally, biodegradable waste is directed away from landfills, and landfills have been required to have a gas collection system since 2009 (Saunois et al., 2024).

There is a wide variety of quantitative techniques for the measurement of landfill methane emissions, ranging from different variants of single or multiple point gas concentration measurements through tracer gas dispersion measurements and differential absorption lidar to mass balance methods using aerial and satellite measurements (Huang et al., 2022; Mønster et al., 2019). Recently, satellite spectral imagers like TROPOMI, GHGSat, EnMAP, and PRISMA have been used to map methane column densities above and around landfills for emission quantification, providing an emission assessment independent of pollutant release registers (Maasakkers et al., 2022; Roger et al., 2024b).

For this thesis, measurements were conducted at the Pinto landfill[4], situated a few kilometers south of the city of Madrid, Spain. The landfill receives ∼1800 t of waste daily. Historically, the waste was deposited in an area called Phase III. The process of closing, sealing, and equipping this area with a degassing system was completed in February 2024. Since then, new waste has been deposited in the Phase IV area, located at the northeast end of the landfill (see Chapter 5 for an aerial view of the landfill). Typically, landfill gas emissions begin two or three months after waste deposition (Personnel of the Pinto landfill, personal communication, June 27, 2024). Thus, the methane detected during our measurements in summer 2024 likely originates predominantly from Phase IV.

[3]The carbon dioxide concentration after 1000 years would be approximately 40% of the previous peak concentration enhancement above preindustrial values (Solomon et al., 2009).

[4]The official name of the Pinto landfill is "Landfill of the Mancomunidad del Sur" ("Vertedero de la Mancomunidad del Sur"). In this thesis, the landfill will be referred to as "Pinto landfill," as this is the term used in the scientific literature because most of the landfill is located in the municipality of Pinto, and it is more concise than the official name.

In the following, some previously assessed emission rates are presented[5]. The Spanish Register of Emissions and Pollutant Sources (PRTR-España) reports emission rates of $1.55\,\mathrm{t\,CH_4\,h^{-1}}$ in 2021, $0.037\,\mathrm{t\,CH_4\,h^{-1}}$ in 2022, and $0.66\,\mathrm{t\,CH_4\,h^{-1}}$ in 2023, positioning the Pinto landfill as the largest Spanish methane emitter in 2021 and the second largest in 2023. Prior to 2022, these emission rates were calculated using emission factors, whereas from 2022 onward, they are based on measurements (Ministry for the Ecological Transition and the Demographic Challenge (MITECO), 2025). The TNO GHGco v5 dataset lists the Pinto landfill with an emission rate of $1.28\,\mathrm{t\,CH_4\,h^{-1}}$ in 2018 (TNO preliminary data, Hugo Denier van der Gon, personal communication, 2025). Using satellite observations from TROPOMI and IASI acquired between 2018 and 2020, Tu et al. (2022) found that the three landfills Valdemingómez, Pinto, and Alcalá in the Community of Madrid, Spain, collectively emit $(7.1 \pm 0.6)\,\mathrm{t\,CH_4\,h^{-1}}$, while the PRTR-España lists a total emission rate of $2.4\,\mathrm{t\,CH_4\,h^{-1}}$ for these landfills in 2019. Additionally, Krautwurst et al. (2024) found an emission rate of $\sim 5\,\mathrm{t\,CH_4\,h^{-1}}$ for the Pinto landfill using aerial passive imaging (MAMAP2DL) and active lidar (CHARM-F) remote sensing measurements on August 4, 2022.

The discrepancy between emission inventory values and independent measurement studies may be attributed to several factors. First, the use of estimated, non-ideal parameters in the waste decay model for emission calculations (Wang et al., 2024). Second, the register may only account for emissions from the currently active, open parts of a landfill, neglecting emissions from covered and mostly, but not completely sealed areas (Tu et al., 2022). Additionally, a diurnal cycle in landfill emissions, where daytime emissions are significantly higher than nighttime emissions, could contribute to this discrepancy (Delkash et al., 2022). Remote sensing observations are conducted during the day, whereas inventory data represents an annual average, encompassing the entire day-night-cycle. Despite these considerations, the significant discrepancy suggests that further investigation into the landfill's methane emissions may be warranted, especially focusing on emission variability.

However, comparisons between the listed emission rates and our measurements should be interpreted cautiously, as the transition of the Pinto landfill from Phase III to Phase IV might have altered the emission rate since early 2024.

This thesis investigates the feasibility of ground-based stationary imaging for detecting and quantifying landfill methane emissions using a hyperspectral camera in the short wave infrared (SWIR) spectral range. In this sense, it complements the doctoral thesis by Knapp (2024), which pioneered the use of this ground-based camera for quantifying methane emissions from a coal mine ventilation shaft and carbon dioxide emissions from a coal-fired power plant. While the camera's specifications are comparable to that of

[5] For better comparability with our measurement data, these are all given in $\mathrm{t\,CH_4\,h^{-1}}$ here, even though this conversion assumes a constant emission rate throughout the day and year, which might not be given.

satellite and aerial imagers, the ground-based setup allows for prolonged observations of a single point source, with an imaging rate on the order of one minute.

Chapter 2 provides the physical background necessary for atmospheric remote sensing in the SWIR spectral range using a push-broom imager. Chapter 3 details the camera's properties and describes the wind lidar used for wind measurements. Chapter 4 explains the matched filter data analysis employed to retrieve methane slant column enhancements from the observed spectra. Chapter 5 briefly summarizes the measurement campaign at the Pinto and Valdemingómez landfills in June and July 2024. Chapter 6 presents the findings, including data analysis challenges, characterization of methane distribution, and concludes with time series of methane emission rates for two days in July 2024. Finally, Chapter 7 summarizes this work and offers ideas for future investigations.

2 Background

This thesis uses a hyperspectral camera to capture sky-scattered sunlight in the SWIR spectral range. The following chapter provides the theoretical foundation for this application. Section 2.1 offers a concise overview of the Earth's atmospheric composition. Section 2.2 delves into the physics of atmospheric radiative transfer, focusing on the emission, absorption, and scattering of light by molecules and aerosols. This culminates in the radiative transfer equation, with two solutions from simplified versions presented at the end. Section 2.3 explains the basics of grating spectrometry and the functionality of a push-broom imager, the type of spectral imager used in this study.

This chapter aims to provide essential background information for understanding the thesis and does not aim to cover every detail or phenomenon, focusing only on relevant aspects within the scope of this research.

2.1 Composition of the Earth's Atmosphere

Petty (2006) provides an overview of the Earth's atmosphere, which will be summarized here, focusing on key facts relevant to our application.

The Earth's atmosphere comprises different layers, of which only the troposphere as the lowest layer is truly relevant for our measurements. The troposphere starts at ground level and extends up to approximately 15 km in height, depending on latitude and season. It is well-mixed due to convection, as it is heated at the ground.

Dry air in the troposphere primarily consists of 78.1% molecular nitrogen (N_2), 20.9% molecular oxygen (O_2), and 0.93% argon (Ar). Amongst the remaining 0.07% trace gases are carbon dioxide (CO_2) and methane (CH_4), whose concentrations have been rising continuously due to human activities. They have reached levels of (419.32 ± 0.10) ppm CO_2 (Lan et al., 2024a) and (1921.76 ± 0.46) ppb CH_4 (Lan et al., 2024b) in 2023, respectively. These two gases are also the most important greenhouse gases, along with water vapor (H_2O), whose tropospheric concentration varies significantly by location and time, influenced mainly by temperature rather than direct human impact.

2.2 Radiative Transfer in the Earth's Atmosphere

Molecules and particles in the atmosphere interact with electromagnetic radiation at specific wavelengths through the processes of emission, absorption, and scattering. These

interactions are detailed further in the following. Focusing on the radiative processes relevant to this thesis, this section will omit negligible effects and irrelevant topics.

This section is based on Petty (2006), which provides an introduction to radiative transfer processes in the atmosphere, and Demtröder (2018), which delves into the fundamentals of interactions between electromagnetic radiation and molecules.

2.2.1 Radiance

Before diving into the radiative transfer processes in the atmosphere, the physical quantity *radiance* shall be introduced. Radiance describes electromagnetic radiation in terms of its magnitude, direction, and wavelength. When radiative power P in the wavelength interval $[\lambda, \lambda + \mathrm{d}\lambda]$ originates from a solid angle $\mathrm{d}\Omega$ and crosses an area $\mathrm{d}A$ at an angle θ, the corresponding radiance I is defined as

$$I(\lambda, \Omega) = \frac{\mathrm{d}^3 P}{\mathrm{d}A \cos\theta \, \mathrm{d}\Omega \, \mathrm{d}\lambda} \,. \tag{2.1}$$

Radiance is typically measured in units of $\mathrm{W\,m^{-2}\,sr^{-1}\,nm^{-1}}$. Note that in some literature, the quantity termed radiance here may also be referred to as spectral radiance, spectral intensity, radiant intensity, or simply intensity.

2.2.2 Emission

Thermal radiation is emitted by any object with a temperature T. In the ideal case of a black body, a perfect emitter, the emitted radiance $B_\lambda(\lambda, T)$ per wavelength λ is given by Planck's law

$$B_\lambda(\lambda, T) = \frac{2hc^2}{\lambda^5} \frac{1}{\exp\left(\frac{hc}{k_\mathrm{B}\lambda T}\right) - 1} \,, \tag{2.2}$$

where h is the Planck constant, c is the speed of light, and k_B is the Boltzmann constant. For other objects, this black body radiation sets the upper limit of possible emission and is often used as a reasonable approximation.

When comparing the Sun's radiance in the Earth's atmosphere to the thermal radiance of molecules in the atmosphere, it becomes clear that thermal emission is completely negligible in the SWIR range around a wavelength of 2000 nm.

2.2.3 Absorption

Electromagnetic radiation of wavelength λ or frequency ν is quantized into photons of energy $E = hc/\lambda = h\nu$. A molecule can absorb a photon if the photon's energy equals the energy difference between the molecule's current and an energetically higher quantum

state, and if this transition is allowed by the selection rules[1]. Molecular quantum states can be divided into electronic, vibrational, and rotational states. As transitions between electronic states usually require an energy corresponding to photons in the visible or ultraviolet spectral range, these are not treated here.

Vibrational states A molecule can vibrate, meaning its atomic nuclei exhibit a periodic movement relative to one another. For a diatomic molecule, the only possible vibrational mode is a movement of the two nuclei along their imaginary connection line, like they were mounted at the two ends of a spring. This vibration can occur in quantized strengths, corresponding to equidistant energy levels. For a non-linear molecule consisting of N atoms, $3N-6$ vibrational normal modes exist[2], which results in a much more complicated structure of the vibrational energy levels. The vibrational states have energy differences on the order of 10^{-1} eV, which corresponds to wavelengths on the order of 10 µm and smaller.

Rotational states A molecule can rotate, and these rotational energy levels are quantized as well. Diatomic and all other linear molecules can only rotate around the axis through their center of mass and perpendicular to the molecular axis, but for any other molecule, any rotational axis through the center of mass is possible, again resulting in a much more complicated structure of the rotational energy levels, compared to linear molecules. The rotational states have energy differences on the order of 10^{-4} eV, which corresponds to wavelengths on the order of 10 mm and smaller.

In addition to transitions between vibrational or rotational states, combined transitions are possible as well. In these, a molecule changes both its vibrational and rotational state. These transitions are frequently called ro-vibrational transitions.

As energy needs to be conserved, absorption is only possible if the molecule can transition into an energetically higher state such that the energy difference between the current and the higher molecular state equals the energy of the photon to be absorbed[3]. This absorption produces an absorption line in a transmission spectrum. Each molecular species exhibits characteristic absorption lines i, each of which is described by a line's absorption cross-section

$$\sigma_{\mathrm{a},i}(\nu) = S_i \cdot f(\nu - \nu_i)\,, \tag{2.3}$$

[1] Selection rules are a complex topic in itself and will not be covered here.

[2] Depending on molecular symmetries, some of these normal modes may have equal energies. For example, this is the case for methane, which has only four normal modes of distinct energies. Therefore, some sources state it has only four normal modes, some of which are then called degenerate (e.g., Kefala et al., 2024).

[3] To follow conservation of momentum, the molecule will also change its velocity when absorbing a photon. At atmospheric temperatures, molecules move at a few hundred meters per second, whereas the change in velocity for absorption of a photon in the SWIR spectral range is on the order of centimeters per second.

with the center frequency[4] ν_i, the strength S_i, and the shape function $f(\nu - \nu_i)$. The absorption line's center frequency ν_i is determined by the energy of the corresponding molecular transition[5]. The line shape $f(\nu - \nu_i)$ is the distribution of the absorption around the center frequency ν_i and is normalized to 1. The strength S_i is the integral over the line's absorption cross-section $\sigma_{\mathrm{a},i}$. Summing over the absorption cross-sections $\sigma_{\mathrm{a},i}$ of all lines i yields the total absorption cross-section

$$\sigma_{\mathrm{a}}(\nu) = \sum_i \sigma_{\mathrm{a},i}(\nu)\,. \tag{2.4}$$

This absorption cross-section $\sigma_{\mathrm{a}}(\nu)$ characterizes the number of photons $\mathrm{d}N_\nu$ of frequency ν absorbed along the path $\mathrm{d}s$ in a gas with molecular density n and N_ν the number of incident photons:

$$\frac{\mathrm{d}N_\nu}{\mathrm{d}s} = -N_\nu \cdot \sigma_{\mathrm{a}}(\nu) \cdot n\,. \tag{2.5}$$

The product of absorption cross-section $\sigma_{\mathrm{a}}(\nu)$ and molecular density n defines the absorption coefficient

$$\beta_{\mathrm{a}}(\nu) = \sigma_{\mathrm{a}}(\nu) \cdot n\,. \tag{2.6}$$

A line's strength S_i is determined by the fraction of molecules in the required initial state for the transition, and the intrinsic probability of a photon with the correct wavelength hitting a molecule actually producing this transition. In the atmosphere, thermal equilibrium prevails up to a height of about 120 km, meaning the population density of the molecular states is given by a Boltzmann distribution and defined by the local temperature. The intrinsic probability of a transition happening depends on the Einstein B coefficient of that transition, which can be derived in the framework of quantum electrodynamics, but this would exceed the scope of this thesis. Furthermore, an absorption line can be degenerate, meaning there are multiple transitions that have the exact same energy difference.

There are different effects that determine a line's shape and width, which are described in the following.

Natural broadening Natural broadening describes the natural width of an absorption line, which is due to Heisenberg's uncertainty principle and independent of external variables like gas temperature or pressure. In the atmosphere, this natural broadening is negligible in comparison to the two following broadening effects.

[4] In the following description, all expressions are in terms of frequency, as these can be derived from first principles. The conversion of, e.g, a line width from frequency to wavelength can be achieved through different ways, resulting in slightly different expressions, even though the numerical difference between these different wavelength expressions is tiny (Lovett & Parsons, 1977).

[5] Different effects, which will not be described here, can lead to a slight shift of the center frequency of an absorption line.

Doppler broadening A second broadening effect originates from the temperature T of the gas. This temperature is associated with a velocity distribution of the molecules, which is a Maxwell-Boltzmann distribution if thermal equilibrium prevails. If a molecule moves toward a photon it is about to absorb, the photon has a smaller wavelength and thus an increased energy due to the Doppler effect in the molecule's frame of reference. The opposite is true for a molecule moving in the same direction as the photon. Through this effect, photons with a higher or lower energy are absorbed, if their Doppler shift accounts for the energy difference to the molecular transition energy. This results in a Gaussian line shape

$$f_{\mathrm{D}}(\nu - \nu_0) = \frac{1}{\gamma_{\mathrm{D}}\sqrt{\pi}} \exp\left(-\frac{(\nu - \nu_0)^2}{\gamma_{\mathrm{D}}^2}\right) \tag{2.7}$$

with the full width at half maximum (FWHM) $\gamma_{\mathrm{D}}\sqrt{\ln 2} \propto T^{1/2}\, m^{-1/2}$ and the molecular mass m. The higher the temperature of the gas, the broader the velocity distribution of the molecules, and thus the stronger the line broadening. Doppler broadening is the dominant broadening effect in the upper atmosphere.

Pressure broadening A third broadening effect depends on the pressure p of the gas. Transitions between quantum states can be affected by simultaneous collisions with other molecules, which are more likely at higher pressure. The theory behind pressure broadening is quite complicated, so here we settle for the result that pressure broadening usually can be sufficiently well described by a Lorentzian line shape

$$f_p(\nu - \nu_0) = \frac{\gamma_p/\pi}{(\nu - \nu_0)^2 + \gamma_p^2} \tag{2.8}$$

with the FWHM $2\gamma_p$, which is roughly proportional to the molecular collision rate. To first order, this implies $\gamma_p \propto p\, T^{-1/2}$. Pressure broadening is the dominant broadening effect in the lower atmosphere.

Further effects like speed dependence of pressure broadening, line mixing, and Dicke narrowing affect the spectral line shape, but these corrections were neglected when generating the unit absorption spectrum (UAS) (see Section 4.1) used for data analysis. After all, the camera used for this thesis has a spectral resolution of a few nanometers, so these effects can be neglected at this spectral resolution.

Unless either Doppler broadening or pressure broadening clearly dominate, the Gaussian and the Lorentzian line shape have to be convoluted to the Voigt line shape

$$f_V(\nu - \nu_0) = (f_{\mathrm{D}} * f_p)(\nu - \nu_0) = \int_0^\infty f_{\mathrm{D}}(\nu' - \nu_0) \cdot f_p(\nu - \nu')\, \mathrm{d}\nu' \,. \tag{2.9}$$

Close to its center, the Voigt line shape is similar to the Gaussian line shape, whereas

the tails on either side resemble the Lorentzian line shape.

Taking all these effects together, one can derive the wavelength dependent atmospheric transmission for different molecular species. Figure 2.1 shows atmospheric transmission spectra for H_2O, CO_2, and CH_4 in the SWIR spectral range between 1000 nm and 2500 nm. The CH_4 absorption band at around 2300 nm is used for CH_4 retrievals in this thesis[6].

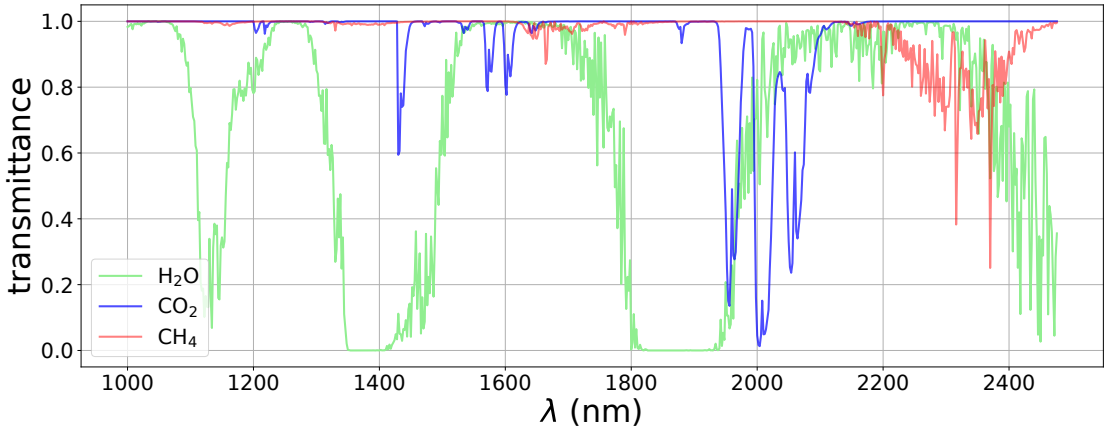

Fig. 2.1. Transmission spectrum of atmospheric H_2O in green, CO_2 in blue, and CH_4 in red, derived from MODTRAN (Berk et al., 2014) and resampled to 2 nm spectral resolution. Figure taken from Roger et al. (2024a).

2.2.4 Scattering

When a photon collides with a molecule or another small particle, it can be scattered, changing its direction. In our application, elastic scattering dominates over inelastic scattering, meaning the photon's wavelength remains unchanged. There are different theories to describe an elastic scattering event which are applicable for different size relations of photon wavelength λ and particle radius r. This is expressed by the size parameter

$$x = \frac{2\pi r}{\lambda} \,. \tag{2.10}$$

The radiative transfer effect of scattering is described by two quantities, depending on refractive index, size, and shape of the scattering particle. The scattering cross-section σ_s characterizes the total scattering probability, analogously to the absorption cross-section σ_a characterizing the probability of absorption. The scattering phase function $p(\theta)$

[6] Methane's shortwave (1000 nm to 5000 nm) bands contribute about 15% to methane's total radiative forcing. This is not obvious, as, e.g., the shortwave bands of CO_2 actually decrease the total radiative forcing of CO_2 through stratospheric absorption of solar radiation (Etminan et al., 2016).

describes the relative probability distribution of scattering angles θ, and is normalized to 4π.

The processes relevant to this thesis are scattering of photons in the SWIR range on molecules and on aerosols. For molecules, the size parameter x is on the order of some 10^{-4}, leading to very weak scattering that is likely negligible compared to aerosol scattering. Still, molecular scattering is included in the computation of the UAS. This scattering is described by Rayleigh theory, which characterizes the dipole interaction of spherical molecules with plane electromagnetic waves, where the wavelength λ is significantly larger than the molecule's radius r ($x < 0.2$). The scattering cross-section is characterized by

$$\sigma_{\mathrm{s,Rayl.}} \propto \frac{r^6}{\lambda^4} \,. \tag{2.11}$$

The scattering phase function is

$$p_{\mathrm{Rayl.}}(\theta) = \frac{3}{4}(1 + \cos^2\theta) \,, \tag{2.12}$$

meaning that forward and backward scattering (θ close to 0 or close to π) are more probable than scattering in a perpendicular angle (θ close to $\pi/2$).

Scattering on aerosols is described by Mie theory ($0.2 < x < 2000$). In most situations, it dominates over Rayleigh scattering in the SWIR range, and the dependence of the scattering cross-section $\sigma_{\mathrm{s,Mie}}$ on particle size and wavelength is much more complicated than Eq. (2.11). For spherical particles with uniform radius, it starts at 0 for $x = 0$, and oscillates around $2\pi r^2$ with an ever smaller amplitude for larger x. In reality, with differently sized particles, only a small wavelength dependence remains. The scattering phase function for aerosols can be approximated by the Henyey-Greenstein phase function

$$p_{\mathrm{HG}}(\theta) = \frac{1 - g^2}{(1 + g^2 - 2g\cos\theta)^{3/2}} \,. \tag{2.13}$$

g is called asymmetry parameter, and is a measure for the asymmetry of the phase function. For $g = 0$, scattering is isotropic, for $g \to \pm 1$, the preferred scattering direction is forward/backward.

Analogously to the absorption coefficient β_{a}, one can define a scattering coefficient β_{s} as the product of scattering cross-section σ_{s} and particle density n

$$\beta_{\mathrm{s}}(\lambda) = \sigma_{\mathrm{s}}(\lambda) \cdot n \,. \tag{2.14}$$

Integrating this scattering coefficient vertically over the whole atmosphere yields the aerosol optical depth

$$\tau(\lambda) = \int_0^\infty \beta_{\mathrm{s}}(\lambda, z') \, \mathrm{d}z' \,, \tag{2.15}$$

which is a measure for the strength of (out-of-beam) scattering happening in the atmosphere. The dependence of τ on the wavelength λ is roughly given by

$$\frac{\tau(\lambda)}{\tau(\lambda_0)} = \left(\frac{\lambda}{\lambda_0}\right)^{-\alpha}, \tag{2.16}$$

with the Ångström exponent α (Ångström, 1929). This allows the calculation of the aerosol optical depth $\tau(\lambda)$ from a given $\tau(\lambda_0)$ and α.

2.2.5 Radiative Transfer Equation

The radiative transfer processes described up to here can be summed up into the radiative transfer equation. It quantifies the change $\mathrm{d}I(\lambda, \boldsymbol{\Omega}, s)$ of radiance $I(\lambda, \boldsymbol{\Omega}, s)$ in the direction $\boldsymbol{\Omega}$ along the path $\mathrm{d}s$ as

$$\frac{\mathrm{d}I}{\mathrm{d}s} = -\beta_\mathrm{a} I - \beta_\mathrm{s} I + \beta_\mathrm{a} B_\lambda(T) + \frac{\beta_\mathrm{s}}{4\pi} \int_{4\pi} p(\boldsymbol{\Omega}', \boldsymbol{\Omega}) I(\boldsymbol{\Omega}') \, \mathrm{d}\boldsymbol{\Omega}' \,. \tag{2.17}$$

Here, $\beta_\mathrm{a}(\lambda, s)$ is the absorption coefficient as given in Eq. (2.6), $\beta_\mathrm{s}(\lambda, s)$ is the scattering coefficient as given in Eq. (2.14), $B_\lambda(\lambda, T(s))$ is the Planck function as given in Eq. (2.2), and $p(\boldsymbol{\Omega}', \boldsymbol{\Omega}, s)$ is the scattering phase function. All quantities in Eq. (2.17) are functions of s, and except for the path $\mathrm{d}s$ and the scattering phase function $p(\boldsymbol{\Omega}', \boldsymbol{\Omega}, s)$, all quantities are functions of the wavelength λ, which is omitted in this equation and also in the following for the sake of readability. The terms on the right-hand side of Eq. (2.17) are—in this order—(molecular) absorption, out-of-beam scattering (by molecules and aerosols), thermal radiation, and into-beam scattering (by molecules and aerosols).

In the form of Eq. (2.17), the radiative transfer equation has no analytical solution due to the into-beam scattering term. One can either choose to numerically solve this differential equation, or introduce simplifications which allow for an analytical solution. This thesis makes use of the second approach, and two such solutions of simplified versions of the radiative transfer equation are presented in the following.

2.2.6 Beer-Lambert Law

The analysis of the hyperspectral camera data with a matched filter (see Chapter 4) as done in this thesis relies on the identification of absorption due to methane in the light path. The change of a spectrum due to absorption and scattering with respect to the amount of a gas or aerosol in the light path is described by the Beer-Lambert law, which is derived in the following. For the detection of methane as just described, only molecular absorption is relevant; nevertheless, this derivation includes out-of-beam scattering as well as absorption, and a version only including absorption can easily be found as an even simpler special case.

Looking at absorption and out-of-beam scattering, and neglecting thermal emission and into-beam scattering, Eq. (2.17) simplifies to

$$\frac{\mathrm{d}I(s)}{\mathrm{d}s} = -\beta_\mathrm{a}(s)I(s) - \beta_\mathrm{s}(s)I(s) = -\beta_\mathrm{e}(s)I(s)\,, \tag{2.18}$$

with the extinction coefficient $\beta_\mathrm{e}(\lambda, s) = \beta_\mathrm{a} + \beta_\mathrm{s}$. This differential equation can easily be solved to

$$I(s) = I(0) \cdot \mathrm{e}^{-\hat{\tau}_\mathrm{e}(s)}\,, \tag{2.19}$$

with the extinction optical path $\hat{\tau}_\mathrm{e}(\lambda, s)$ defined as

$$\hat{\tau}_\mathrm{e}(\lambda, s) = \int_0^s \beta_\mathrm{e}(s')\,\mathrm{d}s'\,. \tag{2.20}$$

Equation (2.19) describes the extinction along the light path s, and is called Beer-Lambert law.

When absorption dominates over scattering, $\beta_\mathrm{e} \approx \beta_\mathrm{a}$. Then

$$\hat{\tau}_\mathrm{e}(s) \approx \hat{\tau}_\mathrm{a}(s) = \int_0^s \beta_\mathrm{a}(s')\,\mathrm{d}s' = \sigma_\mathrm{a} \cdot \int_0^s n(s')\,\mathrm{d}s'\,, \tag{2.21}$$

where σ_a is the absorption cross-section and $n(s')$ is the molecular density at position s'. Here, we used the definition of β_a in Eq. (2.6) and assumed a constant absorption cross-section σ_a along the light path s'.

Thus, absorption is dependent on the molecular density integrated along the light path. This integrated molecular density is called column density, and is the observable quantity in absorption spectroscopy. In this thesis, it is mainly expressed in ppm m, which can be converted into molec m^{-2} using the ideal gas law as

$$\alpha_{\mathrm{molec\,m^{-2}}} = \alpha_{\mathrm{ppm\,m}} \cdot \frac{p}{k_\mathrm{B}T} \cdot \frac{10^{-6}}{\mathrm{ppm}}\,, \tag{2.22}$$

where $\alpha_{\mathrm{molec\,m^{-2}}}$ is the enhancement in molec m^{-2}, $\alpha_{\mathrm{ppm\,m}}$ is the enhancement in ppm m, p is the pressure, T is the temperature, and k_B is the Boltzmann constant. A further conversion to kg m^{-2} can be achieved by multiplying with the molar mass M.

2.2.7 Single Scattering Approximation

In this thesis, the hyperspectral camera data is analyzed using a matched filter. The matched filter needs a UAS as external input, which is calculated from simulated camera observations. We use the single scattering solution of the radiative transfer equation (2.17) to simulate such observations. For a cloudless sky, this solution is a reasonably

good approximation.

As the name suggests, this approximation only considers photons that were scattered into the beam by exactly one scattering event, i.e., all observed photons originate at the Sun, are scattered once in the atmosphere, and then reach the observer. This simplifies the calculation a lot, as the intensity $I(\boldsymbol{\Omega}')$ in the integral in Eq. (2.17) then is a Dirac delta function of the Sun's direction $\boldsymbol{\Omega}_\mathrm{S}$:

$$I(\boldsymbol{\Omega}') = F_\mathrm{S}\,\delta(\boldsymbol{\Omega}' - \boldsymbol{\Omega}_\mathrm{S})\,\mathrm{e}^{-\frac{\tau}{\mu_\mathrm{S}}}\,. \tag{2.23}$$

Here, $F_\mathrm{S}(\lambda)$ is the spectral irradiance of the Sun, τ is the extinction optical depth (defined below in Eq. (2.24)), and $\mu_\mathrm{S} = \cos(\mathrm{SZA}) > 0$ is the cosine of the solar zenith angle (SZA), which is the angle between zenith and Sun.

In addition, the solution presented here also neglects thermal emission, which is reasonable for the SWIR spectral range.

To solve the radiative transfer equation (2.17), we parametrize the slant path s using the vertical coordinate $z = \mu s$. Here, $\mu = \cos(\mathrm{VZA})$ is the cosine of the viewing zenith angle (VZA), which is the angle between zenith and photon propagation direction after the scattering event. For our upward-viewing geometry $\mathrm{VZA} > 90°$ and thus $\mu < 0$ because photons are propagating downward. As the next step we reparametrize the equation, now using the extinction optical depth

$$\tau(\lambda, z) = \int_z^\infty \beta_\mathrm{e}(z')\,\mathrm{d}z' \tag{2.24}$$

as a vertical coordinate, with the extinction coefficient $\beta_\mathrm{e} = \beta_\mathrm{a} + \beta_\mathrm{s}$.

Simplifying Eq. (2.17) like this yields

$$\mu\frac{\mathrm{d}I}{\mathrm{d}\tau} = I - \frac{F_\mathrm{S}\omega(\tau)}{4\pi}\,p(\theta,\tau)\,\mathrm{e}^{-\frac{\tau}{\mu_\mathrm{S}}} \tag{2.25}$$

$$\frac{\mathrm{d}}{\mathrm{d}\tau}\left(I\mathrm{e}^{-\frac{\tau}{\mu}}\right) = -\frac{F_\mathrm{S}\omega(\tau)}{4\pi\mu}\,p(\theta,\tau)\,\mathrm{e}^{-\tau\left(\frac{1}{\mu_\mathrm{S}}+\frac{1}{\mu}\right)}\,. \tag{2.26}$$

The ratio of scattering to extinction efficiency is the single scattering albedo $\omega(\lambda,\tau) = \beta_\mathrm{s}/\beta_\mathrm{e}$. θ is the scattering angle given by the Sun's position and the observation direction.

In the solution presented here, the atmosphere is assumed to comprise N homogeneous, parallel layers (index n), neglecting the Earth's curvature for now. Each layer has a constant single scattering albedo ω_n and scattering phase function $p_n(\theta)$. Integrating Eq. (2.26) layer by layer yields the following solution for downwelling diffuse radiance at the Earth's surface:

$$I = \frac{F_\mathrm{S}\mu_\mathrm{S}}{4\pi(|\mu| - \mu_\mathrm{S})}\mathrm{e}^{-\frac{\tau_N}{|\mu|}}\sum_{n=1}^{N}\mathrm{e}^{-\tau_n\left(\frac{1}{\mu_\mathrm{S}}-\frac{1}{|\mu|}\right)}\omega_n p_n(\theta)\left(1-\mathrm{e}^{-\Delta\tau_n\left(\frac{1}{\mu_\mathrm{S}}-\frac{1}{|\mu|}\right)}\right) \tag{2.27}$$

(Haveresch, 2023). Here, $\tau_N = \tau(z = 0)$ is the total extinction optical depth, τ_n is the extinction optical depth from the top of the atmosphere down to atmospheric layer n, and $\Delta\tau_n = \tau_n - \tau_{n-1}$ is the extinction optical depth of layer n.

The plane-parallel approximation neglects Earth's curvature, which is a good approximation for many sky-scattered sunlight observations. The observations in this thesis have a VZA close to 90°, i.e., the camera points just above the horizon. In this case, the plane-parallel approximation is not valid anymore, but this deviation can be corrected empirically. The correction by Kasten and Young (1989), which was used in this thesis, reads

$$|\mu| = |\cos(\mathrm{VZA})| + 0.505\,72 \cdot (6.079\,95° + \mathrm{VZA} - 90°)^{-1.6364}\,. \tag{2.28}$$

2.3 Imaging Spectrometry

Imaging spectrometry is an umbrella term for all techniques that allow for a pixel-wise observation of spectra, resulting in an image with two spatial and one spectral dimension. While the measurement technique is different and more complex than that of an ordinary camera, the resulting structure of measurement data is comparable, except for the crucial difference that an ordinary color camera records intensities for red, green, and blue light in each spatial pixel, while an imaging spectrometer (also termed spectral or hyperspectral camera) records intensities for tens or hundreds of different wavelengths in each spatial pixel. Furthermore, these wavelengths may not lie in the visible spectral range and are therefore invisible to the human eye, as is the case for the camera employed in this thesis.

Section 2.3.1 treats the basics of grating spectrometry, and is based on Demtröder (2019). Section 2.3 then gets into the details of the imaging spectrometry technique of push-broom imaging, based on information from Shaw and Burke (2003) and Norsk Elektro Optikk AS (2014).

2.3.1 Grating Spectrometry

When light encounters an obstacle, it experiences diffraction. Diffraction cannot be explained by geometric optics alone; instead, the explanation is based on the Huygens principle. According to this principle, any point of a light ray acts as a source of spherical wave fronts. This explains light being diffracted around obstacles.

An optical grating consists of many parallel slits of distance d and width b, through which light can pass. As the light passes through these slits, it is diffracted, meaning all slits act as sources of spherical wave fronts. These wave fronts interfere with each other: At each point behind the grating, the light waves from all slits, carrying different phases due to differences in optical path length, combine to a single intensity value. This interference can result in a large intensity, but it can also happen that all the waves add

up to zero, and no intensity is left. Maximum intensity occurs when the path difference $\Delta s = d \cdot \sin\theta$ between light waves passing two neighboring slits satisfies

$$\Delta s = d \cdot \sin\theta = m \cdot \lambda\,, \tag{2.29}$$

where θ is the diffraction angle, λ is the wavelength, and m is an integer. Therefore, the angle θ of maximum intensity depends on the wavelength λ, effectively splitting the light into its spectral components.

A grating spectrometer is a spectrometer that makes use of a grating as its central optical component to split the incoming light into its different wavelengths. The diffraction pattern then falls onto a detector, where the signal is converted into digital units. A grating spectrometer furthermore consists of different optical components such as apertures, lenses, and/or mirrors.

2.3.2 Push-Broom Imaging

A push-broom imager (also push-broom scanner or along-track scanner) is an imaging spectrometer with a grating as its central optical component. Its working principle is depicted in Fig. 2.2.

Light entering the push-broom imager is focused onto a slit such that only light originating from a narrow strip of the scene passes. The light is then collimated onto a grating that diffracts the incoming light into its wavelength components. The light is then focused onto a two-dimensional array of detector pixels, where one dimension corresponds to the spatial coordinate called *line* here, and the other corresponds to the spectral coordinate called *channel* here. After one such strip, which is called *frame* here, is captured, the camera is either rotated by a certain angle (e.g., like in our case, when deployed on the ground), or is moved by a certain distance (e.g., when deployed on an aircraft), or a combination of both (e.g., on a satellite). This is what characterizes the push-broom imager in contrast to, e.g., a whisk-broom imager: The push-broom imager scans across the scene and captures the image frame by frame and the detector consists of a two-dimensional pixel array resolving spatial lines and spectral channels simultaneously.

Recording an image like this results in a three-dimensional data cube where two dimensions are the spatial x- and y-coordinates *frame* and *line*, and the third dimension is the spectral coordinate *channel*. One such data cube is called image or observation in this thesis. To avoid confusion about the term *pixel*, the term *spatial pixel* is used to refer to a certain frame and line, i.e., a spatial position in the field of view (FOV), while the term *detector pixel* is used to refer to a physical pixel on the detector, representing a certain line and channel.

A push-broom imager may be characterized by the following properties:

FOV The solid angle that an image covers.

FOV per pixel The solid angle that one spatial pixel covers.

Spectral range The detectable wavelength interval.

Instrument line shape (ILS) The response function to a single wavelength signal, usually assumed to be a Gaussian function and characterized by its FWHM.

Spectral sampling distance (SSD) The difference in wavelength between two adjacent spectral channels.

Point spread function The response function to a point source of light, usually assumed to be a Gaussian function and characterized by its FWHM.

In Tab. 3.1, the numerical values of these quantities are listed for the camera used for this thesis.

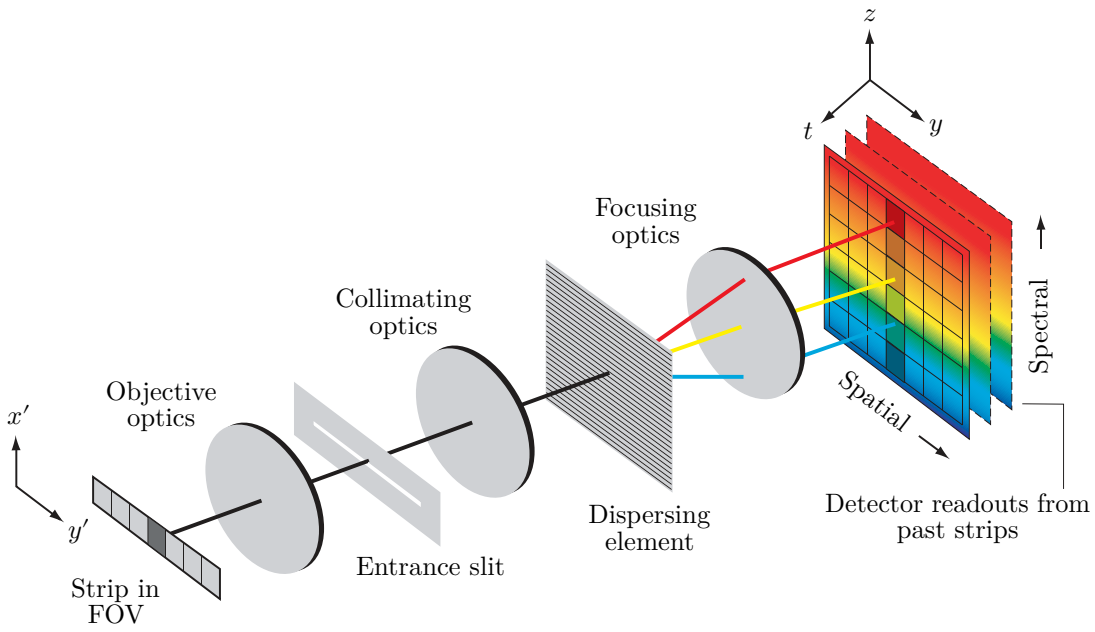

Fig. 2.2. The working principle of a push-broom imager. Light enters the camera from the left, is focused onto an entrance slit, collimated onto the dispersing element, and then focused onto the detector. Over time, different strips of the field of view (FOV) are observed, such that a two-dimensional image with an additional spectral dimension emerges. In our viewing geometry, the observed strips extend vertically. Figure adapted from Knapp (2024), Baumgartner (2022), and Shaw and Burke (2003).

3 Instrumentation

This section describes the instruments that were used during the summer 2024 field campaign near Madrid, Spain (see Chapter 5). Section 3.1 describes the setup of the hyperspectral cameras used for observations, lists the specifications of the camera whose data was used for this thesis, and also details how the camera raw data is converted into a quantity proportional to radiance for further evaluations. Section 3.2 describes the properties of the wind lidar that was co-deployed during the campaign and also outlines its operating principle.

3.1 Hyperspectral Cameras

3.1.1 Field Setup

A hyperspectral camera is a camera that—instead of capturing intensities for red, green, and blue like a conventional camera—captures a discrete spectrum with tens or hundreds of wavelengths for each spatial pixel (see Section 2.3). The hyperspectral camera used for this thesis is the model HySpex SWIR-384 by Norsk Elektro Optikk AS (NEO). Additionally, a HySpex Mjolnir S-620 camera was deployed during the summer 2024 field campaign near Madrid, Spain. Just like the HySpex SWIR-384, it measures in the SWIR spectral range, but its data was not used in this thesis. Furthermore, a HySpex VNIR-1800 camera was mounted beside the HySpex SWIR-384 due to operating software constraints. This camera captures light in the visible and near-infrared range and thus is not suited for detection of methane. All cameras are push-broom imagers, whose basic working principle is detailed in Section 2.3.2.

The cameras are mounted on two tripods and are rotated around the vertical axis during operations using two rotation stages. Two laptops are used to control the cameras. All devices are powered by two battery packs and a solar panel. To prevent overheating, all the equipment except for the solar panel is set up in the shade of a pavilion. This setup is illustrated in Fig. 3.1, which depicts the arrangement during measurements at the Pinto landfill.

3.1.2 Characteristics of the HySpex SWIR-384

The characteristics of the HySpex SWIR-384 camera are listed in Tab. 3.1.

Fig. 3.1. The measurement setup on July 4, 2024, at the Pinto landfill. The black camera on the left tripod is the HySpex Mjolnir S-620. The blue camera on the right tripod is the HySpex VNIR-1800 and the red camera on the right tripod is the HySpex SWIR-384. The cameras and rotation stages are controlled by two laptops, and all devices are powered by two battery packs and a solar panel.

3.1.3 Raw Data Preprocessing

An image captured by the HySpex SWIR-384 camera is output as a three-dimensional array of digital numbers DN_{flc}, which are 16-bit unsigned integers. The indices f, l, and c indicate the coordinates *frame* (horizontal spatial), *line* (vertical spatial) and *channel* (spectral) of the image, which consists of F frames, $L = 384$ lines, and $C = 288$ channels in total. The detector inside the camera is a two-dimensional pixel array resolving lines and channels. Such a physical pixel is referred to as *detector pixel* in the following. The frame coordinate arises from the camera rotating from left to right around its vertical axis and capturing one frame after another. A certain spatial position in the image, i.e., a certain frame and line, is referred to as *spatial pixel*.

Tab. 3.1. Characteristics of the HySpex SWIR-384 camera, which are explained in Section 2.3.2. Values taken from (A) Moritz Sindram (personal communication), (B) Norsk Elektro Optikk AS (n.d.), (C) data acquired with the camera, (D) Norsk Elektro Optikk AS (2021), and (E) the camera software.

Characteristic	Value	Source (see caption)
Vertical FOV	16.06°	A
Number of vertical lines L	384	B
Vertical angular resolution	0.66 mrad to 0.81 mrad	A
Horizontal angular resolution	0.73 mrad	B
Spectral range	953 nm to 2515 nm	C
Number of spectral channels C	288	B
ILS FWHM	7 nm	D
SSD	5.44 nm	C
Detector operating temperature	147 K	E

The digital numbers DN_{flc} can be converted into a photon count (per average detector line vertical opening angle) N_{flc} according to

$$N_{flc} = \frac{\mathrm{DN}_{flc} - \mathrm{BG}_{flc}}{\mathrm{QE}_c \cdot \mathrm{RE}_{lc} \cdot \mathrm{SF}} \,. \tag{3.1}$$

Here, the background BG_{flc} is the sum of an offset introduced by the analog-to-digital converter in the camera and the dark current, which comprises photoelectrons produced by thermal fluctuations. QE_c is the quantum efficiency, which is the wavelength-dependent ratio of photoelectrons to incident photons of the total system consisting of optics and detector. RE_{lc} is the relative responsivity matrix, which accounts for differences in sensitivity of detector pixels due to detector imperfections and properties of the optical components in the camera. It furthermore accounts for the relative differences in vertical angle that the detector lines cover. RE_{lc} is relative in the sense that the average over all lines is 1 for each channel. Lastly, SF is an artificial scaling factor between photoelectrons and digital numbers.

While QE_c, RE_{lc} and SF are known beforehand from calibration measurements, BG_{flc} is calculated for each image individually. For this, 200 readouts are performed with a closed shutter, using the same integration time as for the actual observation. These readouts are taken before capturing the first and after capturing the last frame of an image. The readouts are then averaged to BG_{0lc} and $\mathrm{BG}_{(F-1)lc}$ and interpolated linearly for all frames in between (Norsk Elektro Optikk AS, 2014).

For the data analysis, a conversion from the photon count in Eq. (3.1) to a quantity

proportional to radiance L_{flc} is necessary. The latter is given by

$$L_{flc} = \frac{N_{flc} \cdot h \cdot c}{t \cdot A \cdot \Omega \cdot \Delta\lambda \cdot \lambda_c} \,. \tag{3.2}$$

Here, h is the Planck constant, c is the speed of light, t is the integration time per frame, A is the area of the entrance aperture, Ω is the average solid angle covered by a spatial pixel (relative differences are already accounted for in the relative responsivity matrix RE_{lc}), $\Delta\lambda$ is the SSD (constant for our camera), and λ_c is the center wavelength of a channel.

As the matched filter analysis of an image only requires a quantity proportional to radiance, all quantities that are constant throughout the image can be ignored, resulting in the conversion

$$L_{flc} \propto \frac{\mathrm{DN}_{flc} - \mathrm{BG}_{flc}}{\mathrm{QE}_c \cdot \mathrm{RE}_{lc} \cdot \lambda_c} \,. \tag{3.3}$$

As a last step, defective detector pixels, which fail to sense incoming photons correctly, have to be eliminated from the image. This is achieved by linewise linear interpolation over all such pixels listed in the bad pixel map BP_{lc}, which excludes pixels with exceptionally high, low, or variable response to incoming radiation. Knapp (2024) describes the bad pixel map in detail.

3.2 Wind Lidar WindRanger 200

To measure wind conditions in the field, a WindRanger 200 wind lidar[1] (light detection and ranging) by METEK Meteorologische Messtechnik GmbH was used. It was configured to measure three-dimensional wind velocities at heights of 10 m, 20 m, 50 m, 100 m, 150 m, and 200 m approximately every 8 s. During the Madrid field campaign, the lidar was powered by a solar panel in conjunction with a battery pack. High towers and other characteristic landmarks served as reference points for azimuth directions to align the lidar. This alignment set 0° as the direction of the landmark. Afterward, the positions of these landmarks were used to calculate absolute wind directions, where 0° corresponds to north. For vertical alignment, a built-in spirit level was used.

The WindRanger 200 is a frequency-modulated continuous-wave (FMCW) lidar. This means it continuously emits a laser signal, which is modulated in frequency (as a triangular waveform). Furthermore, the laser is tilted at an angle of 10° relative to the vertical and rotates around the vertical axis once per second. The laser light sent out into the sky is backscattered by aerosols, and the lidar optics are focused at a specific height where wind velocity is to be measured, ensuring that the received signal is primarily composed

[1] The word lidar exists in many different casings (Lidar, LiDAR, LIDAR, LiDaR, ...), but lower case seems to have become the most prominent variant (Deering & Stoker, 2014).

of backscattered light from that focal height level. When the signal is backscattered by moving air/moving aerosols, its frequency undergoes a Doppler shift. Mixing the incoming, backscattered and the outgoing signal allows for measurement of the beat frequency. Assuming constant wind, this beat frequency oscillates at the rotation frequency of the laser, i.e., once per second. To retrieve data, two sine functions are fitted to the beat frequency of the increasing and decreasing branches of the frequency sweeps/triangular wave separately. From the fit parameters, the horizontal wind direction, horizontal wind speed, vertical wind velocity, and measurement height can be calculated. The latter serves as a quality indicator, as it should not deviate significantly from the desired measurement height (METEK Meteorologische Messtechnik GmbH, 2023).

4 Matched Filter

A matched filter is a statistical method to detect a signal in noisy data (Manolakis et al., 2014). In this thesis, spectra of skylight captured with a hyperspectral camera (see Section 2.3) are examined with a matched filter to detect a spectral absorption signal of a target gas like methane. This results in a two-dimensional image showing the signal strength, i.e., the amount of target gas in each pixel.

An alternative to such a matched filter would be a physical retrieval, where a physics-based inversion routine is applied to all pixels sequentially, and multiple species like different gases and aerosol content can be retrieved simultaneously (e.g., Butz et al., 2010, 2011). This is advantageous for heterogeneous scenes, but has much higher computational costs.

The matched filter only requires the observed spectra of all pixels in an image and a predefined unit absorption spectrum (UAS) as input. This UAS is the spectral absorption signal to be detected in the observed spectra. It specifies the relative change of an observed spectrum in dependence of the amount of target gas in the light path. The UAS is artificially generated from a modeled atmosphere and a simulated camera observation.

The matched filter correlates each of the observed spectra with the UAS (or rather, target signature), and outputs a single value per spectrum or pixel which quantifies this correlation. This value is the light path–integrated gas enhancement in the pixel, or simply enhancement for short. It is the amount of target gas that exceeds the atmospheric background concentration. The resulting image shows the spatial distribution of the target gas enhancement, and can be used, e.g., to locate the source of the gas, or to quantify emission rates using additional environmental information like wind velocity.

Section 4.1 explains the generation of the UAS in detail. In Section 4.2, the classic matched filter (CMF) as the simplest version of a suitable matched filter is derived from statistical considerations, followed by a possibly more illustrative and visual derivation of the CMF in Section 4.3. Section 4.4 then lists and describes different improvements to the CMF that enhance its signal detection and quantification capabilities. Section 4.5 derives the lognormal matched filter (LMF); a matched filter differing from the CMF in the underlying assumption of the statistical distribution of the observed spectra. This is followed by an iterative version of the LMF in Section 4.6. Lastly, Section 4.7 discusses performance differences between all these matched filter versions.

4.1 Unit Absorption Spectrum

The unit absorption spectrum (UAS) is the only external input the matched filter needs, apart from the observed spectra themselves. It is the signal that the matched filter tries to find in the observed spectra; it quantifies the relative change of an observed spectrum in dependence of the amount of target gas in the light path. Therefore, the strength of the detected signal in an observed spectrum corresponds to the light path–integrated target gas enhancement—the amount of target gas in the light path exceeding the background concentration.

The UAS needs to be simulated specifically for each instrument. Solving the radiative transfer equation for two atmospheric states—one with and one without a target gas enhancement in the light path—provides two observations of an ideal instrument. For any real instrument, they need to be converted using the ILS and the camera's spectral sampling. The UAS then follows from the ratio of these instrument-specific spectra.

Once generated, a UAS can be used for the analysis of all data that was captured under the same or similar environmental conditions of surface pressure and atmospheric aerosol content, and with the same instrument.

In theory, the UAS $\boldsymbol{s}$ is defined as the change of the logarithmized observed spectrum $\boldsymbol{L}(\alpha)$ per gas enhancement α[1]

$$\boldsymbol{s}(\alpha) = \frac{\partial}{\partial \alpha} \ln \boldsymbol{L}(\alpha)\,. \tag{4.1}$$

Here, the boldface font denotes a spectrum/spectral vector.

This definition of the UAS depends on the gas enhancement α, which is the intended result of the matched filter. While an iterative approach could account for this complexity, it is generally avoided by approximating Eq. (4.1) with the difference quotient

$$\boldsymbol{s} = \frac{\ln \boldsymbol{L}(\alpha) - \ln \boldsymbol{L}(0)}{\alpha}\,, \tag{4.2}$$

for a given enhancement α, which was chosen as 20 000 ppm m, a typical magnitude above a localized methane source like a landfill or a coal mine ventilation shaft. This approximation holds because the at-sensor radiance decreases exponentially with α according to the Beer-Lambert law (2.19) (and Eq. (4.3)). Consequently, $\boldsymbol{s}(\alpha)$ remains nearly constant. The slight variation in $\boldsymbol{s}(\alpha)$ arises from the fact that the UAS quantifies the relative change in *observed* radiance, which includes the instrument's spectral influence (i.e., convolution and binning, see further down). These instrument effects do not commute with atmospheric attenuation affecting the *at-sensor* radiance. This makes the UAS, in theory, dependent on both the atmospheric background concentration and the enhancement.

[1] In our case, this is per 1 ppm m, so the UAS has units of $(\mathrm{ppm\,m})^{-1}$. One could equivalently express the UAS in units of $\mathrm{m^2\,molec^{-1}} = (\mathrm{molec\,m^{-2}})^{-1}$ (see Eq. (2.22)).

However, it is reasonable to calculate a constant UAS from an enhancement over a realistic atmospheric background. The entries of the UAS $\boldsymbol{s}$ are all negative as all entries of the observation with target gas enhancement $\boldsymbol{L}(\alpha)$ are smaller than the corresponding entries of the observation without target gas enhancement $\boldsymbol{L}(0)$ (or equal in spectral regions without absorption).

The radiative transfer model used for the generation of the UAS is the same as in Knapp (2024). It is the single-scattering solution (see Section 2.2.7) of the radiative transfer equation (see Section 2.2.5), modeled for an atmosphere consisting of 100 layers of 400 m thickness each, and with a spectral resolution of 0.001 nm. Only the three most important atmospheric absorbers water, methane, and CO_2 are incorporated in the simulation, and their absorption cross-sections are taken from the HITRAN database (Gordon et al., 2022; Kochanov et al., 2016). Atmospheric standard profiles are taken from G. P. Anderson et al. (1986), with the background concentrations of methane and CO_2 scaled to 1850 ppb and 420 ppm, respectively. Furthermore, the scattering effect of aerosols is included via the aerosol optical depth τ and the asymmetry factor g of the Henyey-Greenstein phase function.

For the Madrid Methane Remote Sensing Campaign 2024, these two aerosol parameters were taken as the median of data collected by the AERONET station (Holben et al., 1998) of Madrid in the months of June and July 2024[2]. The asymmetry factor g is taken for 1020 nm, and the aerosol optical depth $\tau(\lambda)$ is scaled to the retrieval wavelength using Eq. (2.16) with $\tau(1020\,\text{nm})$ and the Ångström exponent α. This results in $g = 0.636$ and $\tau = 0.0160$ for the CH_4 retrievals and $\tau = 0.0156$ for the CO_2 retrievals presented in this thesis. The surface pressure was taken as 940 hPa, which is the average surface pressure measured during the Madrid measurement campaign. For observations of coal mine ventilation shafts in the Upper Silesian Coal Basin (USCB) (Fig. 4.5), the same UAS as used by Knapp (2024) was employed, which is based on data taken from the AERONET station at Racibórz[3].

The at-sensor radiance without target gas enhancement is directly obtained from the radiative transfer model, while the at-sensor radiance with target gas enhancement is calculated by subsequently applying the Beer-Lambert law (2.19). Since the absorption due to target gas enhancement occurs close to the camera and over a small fraction of the total light path, we can assume that this additional absorption happens after all other radiative transfer effects have taken place. These two at-sensor radiances are then converted into artificial observation spectra by convolving with the camera's ILS and binning onto the separate detector channels, yielding $\boldsymbol{L}(\alpha)$ and $\boldsymbol{L}(0)$, from which the UAS is then calculated using Eq. (4.2). The ILS is assumed to be a Gaussian function with a FWHM equal to that of the camera's ILS (see Tab. 3.1). The manufacturer's calibration provides the channel wavelengths up to an empirical wavelength shift of 0.75 nm for the

[2]Data of processing level 1.5 from the station located at 40.45190° N, 3.72395° W, 680 m.
[3]Station located at 50.08310° N, 18.19170° E, 230 m.

2300 nm methane absorption band and 2.25 nm for the 2050 nm CO_2 absorption band (Knapp, 2024; Siegel, 2023).

Unless otherwise noted, the CH_4 retrievals use a spectral window from 2190 nm to 2396 nm and the CO_2 retrievals use a spectral window from 1967 nm to 2260 nm, so the UAS is generated only in the respective spectral range.

As methane and CO_2 have significant atmospheric background concentrations, the length of the light path changes the observed slant column density of the gas significantly (see also Section 6.2), and thus also influences the UAS: the longer the light path, the smaller the influence of an additional gas enhancement, hence the smaller the modulus of the UAS (Foote et al., 2021). The light path depends on the viewing geometry, which is why this whole calculation of the UAS is done for viewing elevation angles (VEAs) of 1°, 4°, 7°, 10°, 13°, 16°, 19°, and 22°, for solar zenith angles (SZAs) of 10°, 30°, 50°, 70°, and 80°, and for relative azimuth angles (RAAs) between the observation direction and the Sun of 0°, 45°, 90°, 135°, and 180°. As can be seen in Fig. 4.1, the absolute UAS decreases with decreasing VEA and increasing SZA as the light path lengthens. The influence of the RAA on the UAS is only in the per mill range as it does not change the light path length, but only scattering efficiency.

This results in a look-up table, which is ready to be used for matched filter retrievals. It is specific to a measurement campaign due to the location-dependent surface pressure and aerosols parameters, and specific to a camera due to the ILS and the wavelength calibration. At the same time, this look-up table can be used for analysis of measurement data from different dates and day times.

Before applying the matched filter to an image, the UAS look-up table is interpolated onto the image pixels, such that each pixel has its own, geometry-dependent UAS. For this, the position of the Sun is calculated from the date, time, and location of the observation using pvlib python (K. S. Anderson et al., 2023). The viewing direction of each pixel is calculated from the geographic position of the camera, the geographic position of a landmark in the image, and the pixel position of this landmark in the image in terms of frame and line. This calculation incorporates the results of a geometric characterization of the camera provided by Moritz Sindram (personal communication). The process of this characterization is detailed in Sindram (2021) for a similar camera.

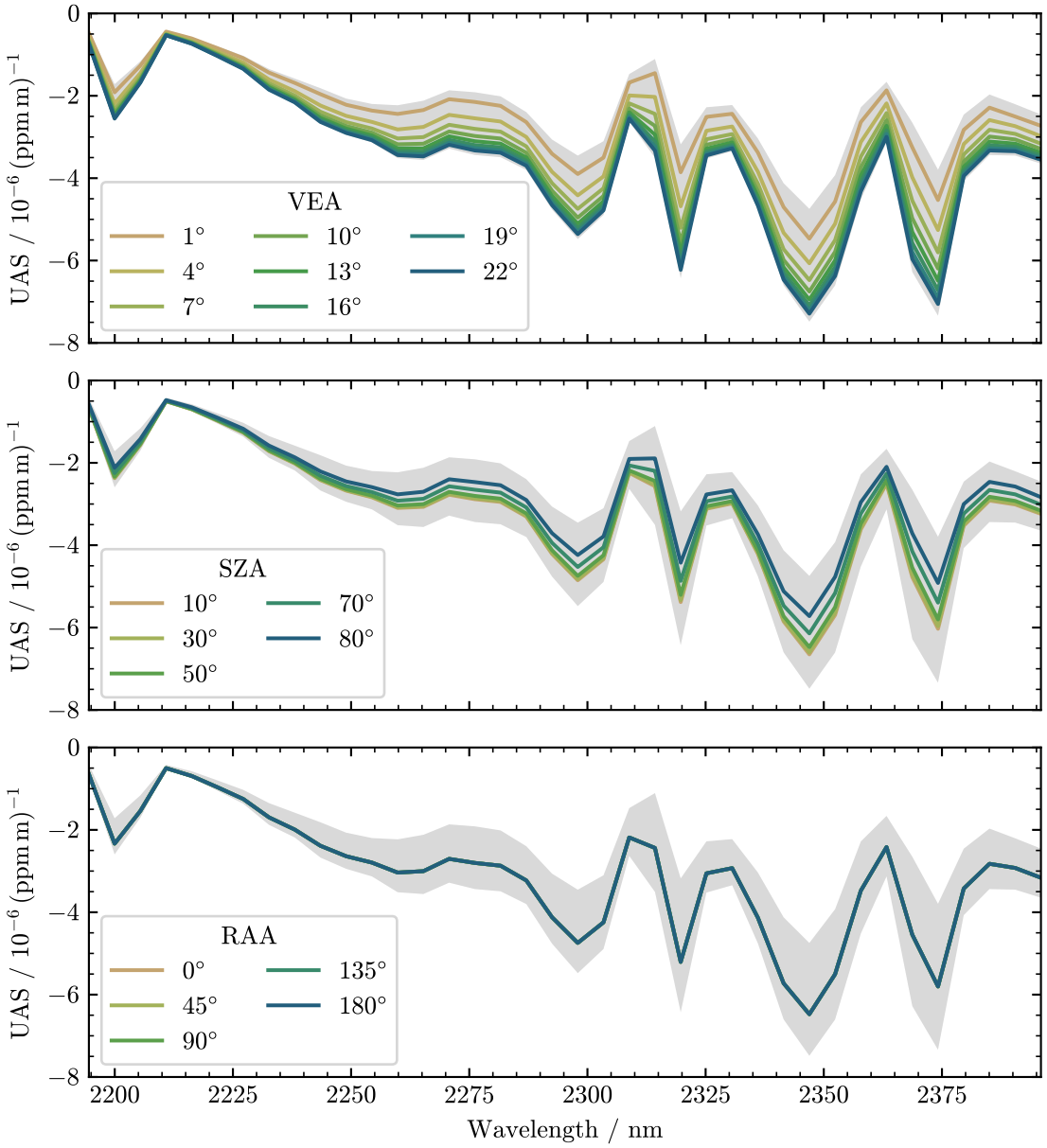

Fig. 4.1. The UAS that was used for retrieving methane enhancements from the Madrid campaign data. The gray envelope shows the variation of the UAS for SZAs between 10° and 80°, VEAs between 1° and 22°, and RAAs between 0° and 180°. Each panel shows the change of the UAS with one angle varied, while the other two angles are fixed to VEA = 6°, SZA = 50°, and RAA = 90°. The change of the UAS in dependence of the RAA is only in the per mill range and thus not visible here.

4.2 Classic Matched Filter

A hyperspectral image consists of P spatial pixels each containing a value in C different spectral channels. It can thus be represented by the vector $\vec{\boldsymbol{L}} = (\boldsymbol{L}_1, \boldsymbol{L}_2, \dots, \boldsymbol{L}_P)$, where $\boldsymbol{L}_p$ is the spectrum of the p^{th} pixel containing radiances in C different spectral channels.

In analogy to the Beer-Lambert law (2.19), a pixel's spectrum $\boldsymbol{L}_p$ can be modeled as

$$\boldsymbol{L}_p \approx \boldsymbol{L}_{p,0} \odot \exp(\alpha_p \cdot \boldsymbol{s}_p)\,, \tag{4.3}$$

where $\boldsymbol{L}_{p,0}$ would be the observed spectrum without any gas enhancement in the light path, α_p is the light path–integrated gas enhancement (e.g., in ppm m), $\boldsymbol{s}_p$ is the UAS for this pixel (which has only negative entries), $\odot$ denotes componentwise multiplication,

Tab. 4.1. Symbols used in the following derivations of the different versions of the matched filter. Boldface denotes a spectral vector (dimension C), a vector arrow denotes a spatial vector (dimension P), and a double-struck letter denotes a spectral matrix (dimension $C \times C$). A variable can also be a spectral and spatial vector at the same time (dimension $C \times P$). The entries in the table are sorted by their dimensions.

Symbol	Type/Dimension	Name/Meaning
P	Fixed scalar	Number of spatial pixels (number of lines times number of frames minus pixels that are masked out)
C	Fixed scalar	Number of spectral channels
p	Index	Index specifying the spatial pixel
c	Index	Index specifying the spectral channel
$\vec{\boldsymbol{L}}$	$C \times P$	Observed spectra in an image
$\vec{\boldsymbol{s}}$	$C \times P$	Unit absorption spectra
$\vec{\boldsymbol{t}}$	$C \times P$	$\boldsymbol{\mu} \odot \vec{\boldsymbol{s}}$; target signatures
$\boldsymbol{\mu}$	C	Mean spectrum
$\boldsymbol{\nu}$	C	Mean logarithmized spectrum
$\mathbf{1}$	C	Spectral vector of ones
$\mathbb{C}$	$C \times C$	Spectral covariance matrix
$\vec{\alpha}$	P	Gas enhancements
$\vec{r}$	P	Albedo factors
$\vec{\sigma}$	P	Noise-equivalent enhancements
$\odot$	Operator	componentwise multiplication of spectral vectors; conserves the vectors' dimensions

and $\exp(\square)$ is applied componentwise as well. This approximation ignores the noise in the measurement as well as the fact that, in reality, the absorption and scattering of photons due to the gas enhancement happen before the light passes the detector optics and these two processes are treated here as if they were commutable.

Assuming only a small portion of pixels exhibits a significant gas enhancement, $\boldsymbol{L}_0$ can be approximated by the mean spectrum over all pixels

$$\boldsymbol{\mu} = \frac{1}{P}\sum_{p=1}^{P} \boldsymbol{L}_p \,, \tag{4.4}$$

such that

$$\begin{aligned} \boldsymbol{L}_p &\approx \boldsymbol{\mu} \odot \exp(\alpha_p \cdot \boldsymbol{s}_p) && (4.5)\\ &\approx \boldsymbol{\mu} \odot (\mathbf{1} + \alpha_p \cdot \boldsymbol{s}_p) && (4.6)\\ &= \boldsymbol{\mu} + \alpha_p \cdot \boldsymbol{t}_p \,, && (4.7) \end{aligned}$$

defining the target signature

$$\boldsymbol{t}_p = \boldsymbol{\mu} \odot \boldsymbol{s}_p \tag{4.8}$$

as a shorthand for further calculations.

Assuming the observed spectra follow a multivariate normal distribution

$$\boldsymbol{L}_p \sim \mathcal{N}(\boldsymbol{\mu}, \mathbb{C}) \tag{4.9}$$

with the mean spectrum $\boldsymbol{\mu}$ and the covariance matrix[4]

$$\mathbb{C} = \frac{1}{P-1}\sum_{p=1}^{P} (\boldsymbol{L}_p - \boldsymbol{\mu})(\boldsymbol{L}_p - \boldsymbol{\mu})^\top \,, \tag{4.10}$$

where $\square^\top$ denotes the transposed of a vector, the likelihood $\mathcal{L}$ of an observation $\vec{\boldsymbol{L}}$ given the pixel's enhancements $\vec{\alpha}$ is

$$\mathcal{L}(\vec{\boldsymbol{L}}|\vec{\alpha}) = ((2\pi)^C \det \mathbb{C})^{-P/2} \exp\left(-\frac{1}{2}\sum_{p=1}^{P} (\boldsymbol{L}_p - (\boldsymbol{\mu} + \alpha_p \boldsymbol{t}_p))^\top \mathbb{C}^{-1} (\boldsymbol{L}_p - (\boldsymbol{\mu} + \alpha_p \boldsymbol{t}_p)) \right) . \tag{4.11}$$

This likelihood is maximized by the classic matched filter (CMF)

$$\alpha_p = \frac{(\boldsymbol{L}_p - \boldsymbol{\mu})^\top \mathbb{C}^{-1} \boldsymbol{t}_p}{\boldsymbol{t}_p^\top \mathbb{C}^{-1} \boldsymbol{t}_p} \,, \tag{4.12}$$

[4] In some papers $\mathbb{C}$ is normalized by P instead of $P-1$, but this distinction is negligible in our case, where P is on the order of 10^5.

giving the gas enhancement α_p of pixel p in ppm m. For a mathematical derivation of this maximum likelihood, see, e.g., the appendix of Knapp (2024).

4.3 Visual Derivation of the Classic Matched Filter

In the following, the CMF will be derived in a more visual way, analogously to the derivation of the normalized matched filter in Manolakis et al. (2014).

Figure 4.2 schematically shows the observed spectra of an image. For simplicity, only the values in two different spectral channels are shown in the plot, but the following derivation works for an arbitrary number of spectral channels C. The two axes represent the measured intensity in two channels, and each gray point represents one pixel. Each point's position is thus defined by the observed intensities in the two channels.

The blue point labeled $\boldsymbol{\mu}$ is the mean spectrum, placed at the mean position of all gray points. The green point labeled $\boldsymbol{L}_p$ is the spectrum of one exemplary pixel p. We can put the uncertainty of Eq. (4.7) into a new variable $\boldsymbol{\varepsilon}_p$, making it an exact equality

$$\boldsymbol{L}_p = \boldsymbol{\mu} + \alpha_p \cdot \boldsymbol{t}_p + \boldsymbol{\varepsilon}_p \,, \tag{4.13}$$

and subtract the mean spectrum $\boldsymbol{\mu}$

$$\boldsymbol{L}_p - \boldsymbol{\mu} = \alpha_p \cdot \boldsymbol{t}_p + \boldsymbol{\varepsilon}_p \,. \tag{4.14}$$

The left-hand side of the equation, $\boldsymbol{L}_p - \boldsymbol{\mu}$, is drawn into Fig. 4.2 as a green vector, pointing from $\boldsymbol{\mu}$ to $\boldsymbol{L}_p$. The right-hand side of Eq. (4.14) is drawn into the figure as well: $\alpha_p \cdot \boldsymbol{t}_p$ in purple and $\boldsymbol{\varepsilon}_p$ in brown. $\boldsymbol{t}_p = \boldsymbol{\mu} \odot \boldsymbol{s}_p$ is predefined as $\boldsymbol{\mu}$ is defined by the mean of all pixel's spectra and $\boldsymbol{s}_p$ is external input and does not depend on the measurement itself. According to Eq. (4.14), $\boldsymbol{t}_p$ has a scalar prefactor α_p, so the direction of the vector $\alpha_p \cdot \boldsymbol{t}_p$ is fixed, as shown by the dashed purple line in Fig. 4.2. α_p can scale the length of the purple vector, and the brown vector $\boldsymbol{\varepsilon}_p$ representing the error must then point from the tip of the purple vector to the point $\boldsymbol{L}_p$. The question is now, how α_p shall be chosen, and a logical choice is such that the norm of the error $\|\boldsymbol{\varepsilon}_p\|$ is minimized. This is exactly the case when $\boldsymbol{\varepsilon}_p$ is orthogonal to $\alpha_p \cdot \boldsymbol{t}_p$. An equivalent condition is that $\alpha_p \cdot \boldsymbol{t}_p$ is the projection of $\boldsymbol{L}_p - \boldsymbol{\mu}$ onto $\alpha_p \cdot \boldsymbol{t}_p$ or $\boldsymbol{t}_p$ or the normalized vector $\boldsymbol{e}_{\boldsymbol{t}_p} = \boldsymbol{t}_p / \|\boldsymbol{t}_p\|$. This can be used to calculate α_p and express it in terms of $\boldsymbol{L}_p$, $\boldsymbol{\mu}$ and $\boldsymbol{t}_p$:

$$\begin{aligned}
\alpha_p \boldsymbol{t}_p &= \operatorname{proj}_{\boldsymbol{t}_p}(\boldsymbol{L}_p - \boldsymbol{\mu}) && (4.15)\\
&= ((\boldsymbol{L}_p - \boldsymbol{\mu})^\top \boldsymbol{e}_{\boldsymbol{t}_p})\, \boldsymbol{e}_{\boldsymbol{t}_p} && (4.16)\\
&= \left((\boldsymbol{L}_p - \boldsymbol{\mu})^\top \frac{\boldsymbol{t}_p}{\|\boldsymbol{t}_p\|} \right) \frac{\boldsymbol{t}_p}{\|\boldsymbol{t}_p\|} && (4.17)
\end{aligned}$$

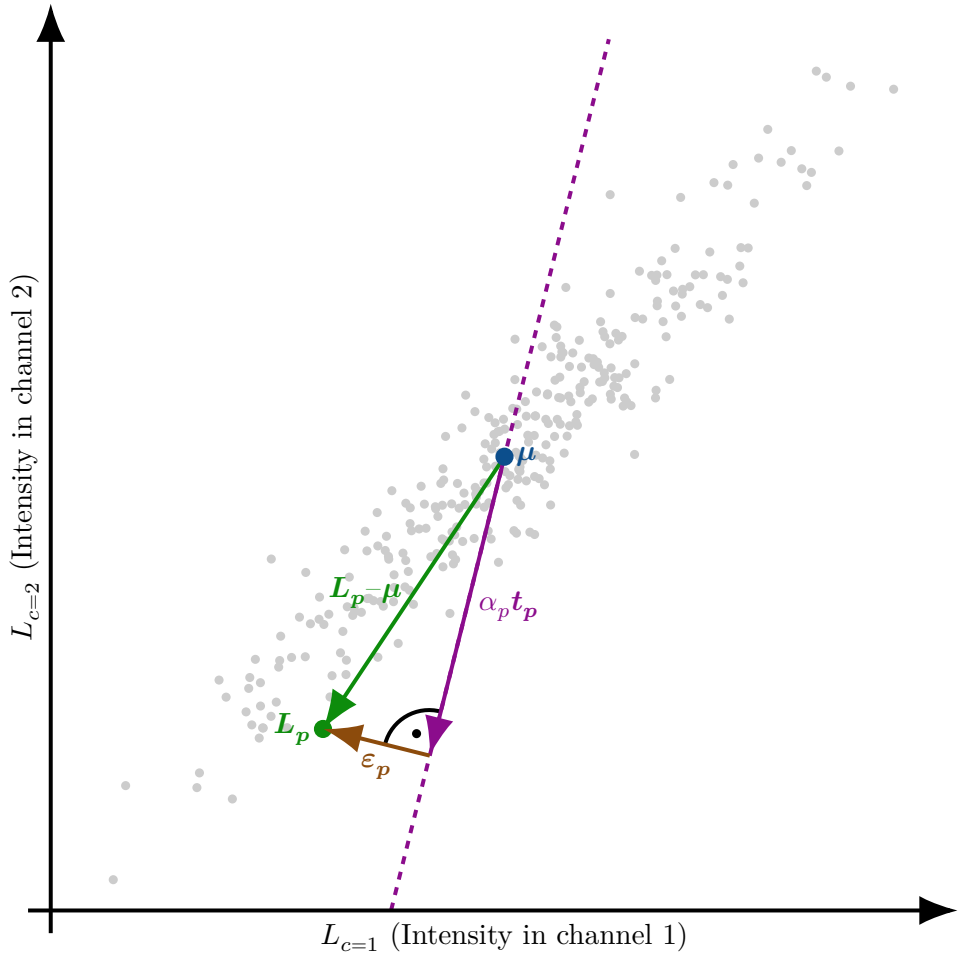

Fig. 4.2. Visual illustration of the working principle of the CMF, which models the difference between a pixel's spectrum $\boldsymbol{L}_p$ and the mean spectrum $\boldsymbol{\mu}$ as the sum of enhancement α_p times target signature $\boldsymbol{t}_p$ and the measurement error $\boldsymbol{\varepsilon}_p$, and chooses the enhancement α_p such that $\|\boldsymbol{\varepsilon}_p\|$ is minimized. Figure inspired by Manolakis et al. (2014).

$$= \frac{(\boldsymbol{L}_p - \boldsymbol{\mu})^\top \boldsymbol{t}_p}{\|\boldsymbol{t}_p\|^2} \, \boldsymbol{t}_p \,. \tag{4.18}$$

Thus follows

$$\alpha_p = \frac{(\boldsymbol{L}_p - \boldsymbol{\mu})^\top \boldsymbol{t}_p}{\|\boldsymbol{t}_p\|^2} \tag{4.19}$$

$$= \frac{(\boldsymbol{L}_p - \boldsymbol{\mu})^\top \boldsymbol{t}_p}{\boldsymbol{t}_p^\top \boldsymbol{t}_p} \,. \tag{4.20}$$

This expression is already very similar to the CMF in Eq. (4.12). What is missing is the covariance matrix $\mathbb{C}$, whose entry into the CMF is explained and derived in the following.

If a pixel p is brighter than average (e.g., $\|\boldsymbol{L}_p\| > \|\boldsymbol{\mu}\|$), probably most its channels will be brighter than average, and the equivalent is true for a pixel being darker, meaning there will be a strong correlation between all the channels' intensities over the whole image. This correlation needs to be removed in order to assure the matched filter only detects an enhancement when there is actually an enhanced target gas concentration in the light path, and not when a pixel is just unusually dark. To remove this correlation, we perform the whitening transformation

$$\tilde{\boldsymbol{L}}_p = \mathbb{C}^{-1/2}\boldsymbol{L}_p \,, \qquad \tilde{\boldsymbol{\mu}} = \mathbb{C}^{-1/2}\boldsymbol{\mu} \,, \qquad \tilde{\boldsymbol{t}}_p = \mathbb{C}^{-1/2}\boldsymbol{t}_p \,, \qquad \tilde{\boldsymbol{\varepsilon}}_p = \mathbb{C}^{-1/2}\boldsymbol{\varepsilon}_p \,, \tag{4.21}$$

transforming into a vector space where the covariance between any two distinct channels is zero, i.e., channels are not correlated anymore. The square-root decomposition $\mathbb{C} = \mathbb{C}^{1/2} \cdot \mathbb{C}^{1/2}$ is possible as any covariance matrix $\mathbb{C}$ is positive semi-definite and the decomposition is invertible if $\mathbb{C}$ and thus $\mathbb{C}^{1/2}$ is positive definite.

For these transformed variables, the same derivation as in Eqs. (4.15) to (4.18), minimizing $\|\tilde{\boldsymbol{\varepsilon}}_p\|$ instead of $\|\boldsymbol{\varepsilon}_p\|$, yields

$$\alpha_p \tilde{\boldsymbol{t}}_p = \mathrm{proj}_{\tilde{\boldsymbol{t}}_p}(\tilde{\boldsymbol{L}}_p - \tilde{\boldsymbol{\mu}}) \tag{4.22}$$

$$= ((\tilde{\boldsymbol{L}}_p - \tilde{\boldsymbol{\mu}})^\top \boldsymbol{e}_{\tilde{\boldsymbol{t}}_p})\ \boldsymbol{e}_{\tilde{\boldsymbol{t}}_p} \tag{4.23}$$

$$= \left((\tilde{\boldsymbol{L}}_p - \tilde{\boldsymbol{\mu}})^\top \frac{\tilde{\boldsymbol{t}}_p}{\|\tilde{\boldsymbol{t}}_p\|} \right) \frac{\tilde{\boldsymbol{t}}_p}{\|\tilde{\boldsymbol{t}}_p\|} \tag{4.24}$$

$$= \frac{(\tilde{\boldsymbol{L}}_p - \tilde{\boldsymbol{\mu}})^\top \tilde{\boldsymbol{t}}_p}{\|\tilde{\boldsymbol{t}}_p\|^2}\ \tilde{\boldsymbol{t}}_p \,, \tag{4.25}$$

and for α_p follows the CMF

$$\alpha_p = \frac{(\tilde{\boldsymbol{L}}_p - \tilde{\boldsymbol{\mu}})^\top \tilde{\boldsymbol{t}}_p}{\|\tilde{\boldsymbol{t}}_p\|^2} \tag{4.26}$$

$$= \frac{(\boldsymbol{L}_p - \boldsymbol{\mu})^\top \mathbb{C}^{-1} \boldsymbol{t}_p}{\boldsymbol{t}_p^\top \mathbb{C}^{-1} \boldsymbol{t}_p} \,. \tag{4.27}$$

4.4 Improvements to the Classic Matched Filter

Foote et al. (2020) propose different improvements to this CMF that target different shortcomings of the original algorithm. These are an albedo correction, a sparsity prior, a positivity constraint, and a background correction.

Apart from these, another way to drastically improve the retrieval, especially reducing line artifacts, is a line-wise differential matched filter, where the mean spectrum $\boldsymbol{\mu}$ and covariance matrix $\mathbb{C}$ are calculated for each line individually. If a target gas enhancement might spread over a large portion of a line, such a matched filter needs a clearly defined "background region" where no methane is present, so that $\boldsymbol{\mu}$ and $\mathbb{C}$ can be calculated from the spectra in this region. Usually, this would be a region upwind of the target gas source, and to compensate for the impaired statistics of only having very few pixels to calculate $\boldsymbol{\mu}$ and $\mathbb{C}$, in the case of our ground-based camera, the calculation can be performed for multiple images captured shortly after another at once. As the methane in the images from the Pinto landfill is usually spread horizontally over the whole image, there is no background region, and such a line-wise differential matched filter cannot be applied. For more details on this matched filter, see Knapp (2024).

In the following, the refinements by Foote et al. (2020) are presented.

4.4.1 Albedo Correction

In Eq. (4.5) the absorption due to a gas enhancement is modeled as a *relative* change of a pixel's spectrum, which is independent of the observed total radiance in that pixel. But the Taylor expansion in Eq. (4.7) alters this to the absorption being an *absolute* change of the pixel's spectrum, which is directly proportional to the pixel's total radiance. To compensate for this shift, the target spectrum needs to be scaled by the pixel's albedo factor

$$r_p = \frac{\boldsymbol{L}_p^\top \boldsymbol{\mu}}{\boldsymbol{\mu}^\top \boldsymbol{\mu}}\,, \tag{4.28}$$

which relates a pixel's total radiance to the mean radiance. By this definition, the average albedo factor over the whole image is one.

The albedo-corrected CMF then reads

$$\alpha_p = \frac{(\boldsymbol{L}_p - \boldsymbol{\mu})^\top \mathbb{C}^{-1} \boldsymbol{t}_p}{r_p \boldsymbol{t}_p^\top \mathbb{C}^{-1} \boldsymbol{t}_p}\,. \tag{4.29}$$

The spectral range that is used to calculate this albedo factor should contain more than just the wavelengths of methane absorption to ensure the albedo factor actually represents a true change in pixel brightness instead of strong methane absorption. This avoids that a small albedo factor is assigned to a pixel which only features strong methane absorption, but is not truly darker than average.

4.4.2 Sparsity Prior and Positivity Constraint

Assuming only a small fraction of the pixels in an image are truly enhanced, a reweighted ℓ_1 minimization scheme can be used to artificially force pixels which exhibit a small or negative enhancement to an enhancement of zero. This is done by iteratively calculating the enhancement

$$\alpha_p^k = \max\left(\frac{(\boldsymbol{L}_p - \boldsymbol{\mu})^\top (\mathbb{C})^{-1} \boldsymbol{t}_p - w_p^k}{r_p \boldsymbol{t}_p^\top (\mathbb{C})^{-1} \boldsymbol{t}_p}, 0\right) \tag{4.30}$$

with

$$w_p^k = \frac{1}{\alpha_p^{k-1} + \varepsilon}\,, \tag{4.31}$$

where $\varepsilon > 0$ is a small scalar for numerical stability. Foote et al. (2020) propose 30 such iterations.

4.4.3 Background Correction

Calculating the mean spectrum $\boldsymbol{\mu}$ and the covariance matrix $\mathbb{C}$ from the whole image is reasonable if only few pixels show a significant enhancement; still, correcting for these enhancements improves the matched filter. This is highly beneficial since including enhanced pixels lowers the mean spectrum intensities and increases the spectral variability specifically in the channels associated with strong target gas absorption. Foote et al. (2020) propose to run the matched filter iteratively and subtract the enhancement α_p^{k-1} calculated in the previous iteration from each pixel's spectrum before recalculating $\boldsymbol{\mu}^k$ and $\mathbb{C}^k$:

$$\boldsymbol{\mu}^k = \frac{1}{P}\sum_{p=1}^{P}(\boldsymbol{L}_p - r_p \alpha_p^{k-1} \boldsymbol{t}_p^{k-1}) \tag{4.32}$$

$$\boldsymbol{t}_p^k = \boldsymbol{\mu}^k \odot \boldsymbol{s}_p \tag{4.33}$$

$$\mathbb{C}^k = \frac{1}{P-1}\sum_{p=1}^{P}(\boldsymbol{L}_p - r_p \alpha_p^{k-1} \boldsymbol{t}_p^k - \boldsymbol{\mu}^k)(\boldsymbol{L}_p - r_p \alpha_p^{k-1} \boldsymbol{t}_p^k - \boldsymbol{\mu}^k)^\top\,. \tag{4.34}$$

Alternatively, one could also just remove the pixels that show a significant enhancement above a certain threshold or exhibit a signal-to-noise ratio (SNR) above a certain threshold from the calculation of $\boldsymbol{\mu}$ and $\mathbb{C}$ altogether. This is the approach that Pei et al. (2023) chose for their iterative lognormal matched filter (ILMF) (see Section 4.6).

Together with the sparsity prior, positivity constraint, and albedo correction, this results in the iterative matched filter

$$\alpha_p^k = \max\left(\frac{(\boldsymbol{L}_p - \boldsymbol{\mu}^k)^\top (\mathbb{C}^k)^{-1} \boldsymbol{t}_p^k - w_p^k}{r_p \boldsymbol{t}_p^{k\top} (\mathbb{C}^k)^{-1} \boldsymbol{t}_p^k}, 0\right) \tag{4.35}$$

$$w_p^k = \frac{1}{\alpha_p^{k-1} + \varepsilon} \,. \tag{4.36}$$

4.5 Lognormal Matched Filter

The lognormal matched filter (LMF)—proposed by Schaum (2021) and first implemented by Pei et al. (2023)—differs from the CMF in that the exponential function in Eq. (4.5) is not linearized in first order, but the componentwise natural logarithm is taken. This results in

$$\ln \boldsymbol{L}_p \approx \boldsymbol{\nu} + \alpha_p \cdot \boldsymbol{s}_p \,, \tag{4.37}$$

where $\boldsymbol{\nu}$ is the mean of the logarithmized spectra $\ln \boldsymbol{L}_p$

$$\boldsymbol{\nu} = \frac{1}{P} \sum_{p=1}^{P} \ln \boldsymbol{L}_p \,. \tag{4.38}$$

Schaum (2021) argues that assuming a lognormal distribution of $\boldsymbol{L}_p$ or a normal distribution of $\ln \boldsymbol{L}_p$ is more reasonable than the previous assumption of a normal distribution of $\boldsymbol{L}_p$ since the two distributions only differ significantly in regimes where the normal distribution allows unphysical negative radiance values. Deriving the likelihood function analogously to the CMF results in

$$\begin{aligned} \mathcal{L}(\vec{\boldsymbol{L}}|\vec{\alpha}) = {} & ((2\pi)^C \det \mathbb{C})^{-P/2} \\ & \cdot \exp\left(-\frac{1}{2} \sum_{p=1}^{P} (\ln \boldsymbol{L}_p - (\boldsymbol{\nu} + \alpha_p \boldsymbol{s}_p))^\top \mathbb{C}^{-1} (\ln \boldsymbol{L}_p - (\boldsymbol{\nu} + \alpha_p \boldsymbol{s}_p)) \right) \end{aligned} \tag{4.39}$$

where

$$\mathbb{C} = \frac{1}{P-1} \sum_{p=1}^{P} (\ln \boldsymbol{L}_p - \boldsymbol{\nu})(\ln \boldsymbol{L}_p - \boldsymbol{\nu})^\top \,. \tag{4.40}$$

This likelihood is maximized by the LMF

$$\alpha_p = \frac{(\ln \boldsymbol{L}_p - \boldsymbol{\nu})^\top \mathbb{C}^{-1} \boldsymbol{s}_p}{\boldsymbol{s}_p^\top \mathbb{C}^{-1} \boldsymbol{s}_p} \,. \tag{4.41}$$

This LMF was used for the analysis of the data presented in this thesis. The reason for this can be found in Section 4.7, where the different matched filters are compared.

4.6 Iterative Lognormal Matched Filter

Pei et al. (2023) furthermore use an iterative version of the LMF, where the enhancements are calculated five times, and each time pixels of the previous iteration that exhibit an

SNR greater than 2 are excluded from the new calculation of the mean logarithmized spectrum $\boldsymbol{\nu}$ and the covariance matrix $\mathbb{C}$.

With a pixel's noise-equivalent enhancement of the LMF defined as

$$\sigma_p = \frac{1}{\sqrt{\boldsymbol{s}_p^\top \mathbb{C}^{-1} \boldsymbol{s}_p}}\,, \tag{4.42}$$

the SNR is

$$\mathrm{SNR}_p = \frac{\alpha_p}{\sigma_p} = \frac{(\ln \boldsymbol{L}_p - \boldsymbol{\nu})^\top \mathbb{C}^{-1} \boldsymbol{s}_p}{\sqrt{\boldsymbol{s}_p^\top \mathbb{C}^{-1} \boldsymbol{s}_p}}\,. \tag{4.43}$$

4.7 Differences in Performance Between the Matched Filter Versions

This section compares retrievals using the CMF, CMF with sparsity prior, positivity constraint and background correction (henceforth called reweighted $\ell 1$ matched filter (RWL1MF) just like in Foote et al., 2020)[5], LMF, and ILMF.

In a first step, we investigate which of these matched filters have an albedo bias and therefore require an albedo correction. For this, an image of blue sky $\vec{\boldsymbol{L}}_0$ was artificially imprinted with an absorption signature of a random methane enhancement α_p between 0 ppm m and 20 000 ppm m in randomly selected 2% of its pixels as

$$\boldsymbol{L}_{p,\alpha} = \boldsymbol{L}_{p,0} \odot \exp(\alpha_p \cdot \boldsymbol{s}_p)\,. \tag{4.44}$$

This image was then retrieved using the four previously listed matched filters, each once with and once without an albedo correction, which was calculated according to Eq. (4.28) and Eq. (4.29) (or the equivalent albedo corrected version of other matched filters, where the albedo is a factor in the denominator). This, of course, is a very simplified method of assessing a matched filter's performance, but it is sufficient to test for an albedo bias as we see in the following.

Figures 4.3 and 4.4 show scatter plots with the imprinted enhancements on the x-axis and the retrieved enhancements on the y-axis where each pixel's albedo is represented by color. Figure 4.3 depicts the retrievals without albedo correction, and Fig. 4.4 with albedo correction.

It is clearly visible in Fig. 4.3 that the CMF and RWL1MF exhibit an albedo bias, which is eliminated by the albedo correction in Fig. 4.4. The LMF and ILMF do not show an albedo bias in Fig. 4.3, so an albedo correction actually introduces an albedo bias, as can be seen in Fig. 4.4.

[5]This matched filter is called Matched filter with Albedo correction and reweiGhted L1 sparsity Code (MAG1C) in Knapp (2024).

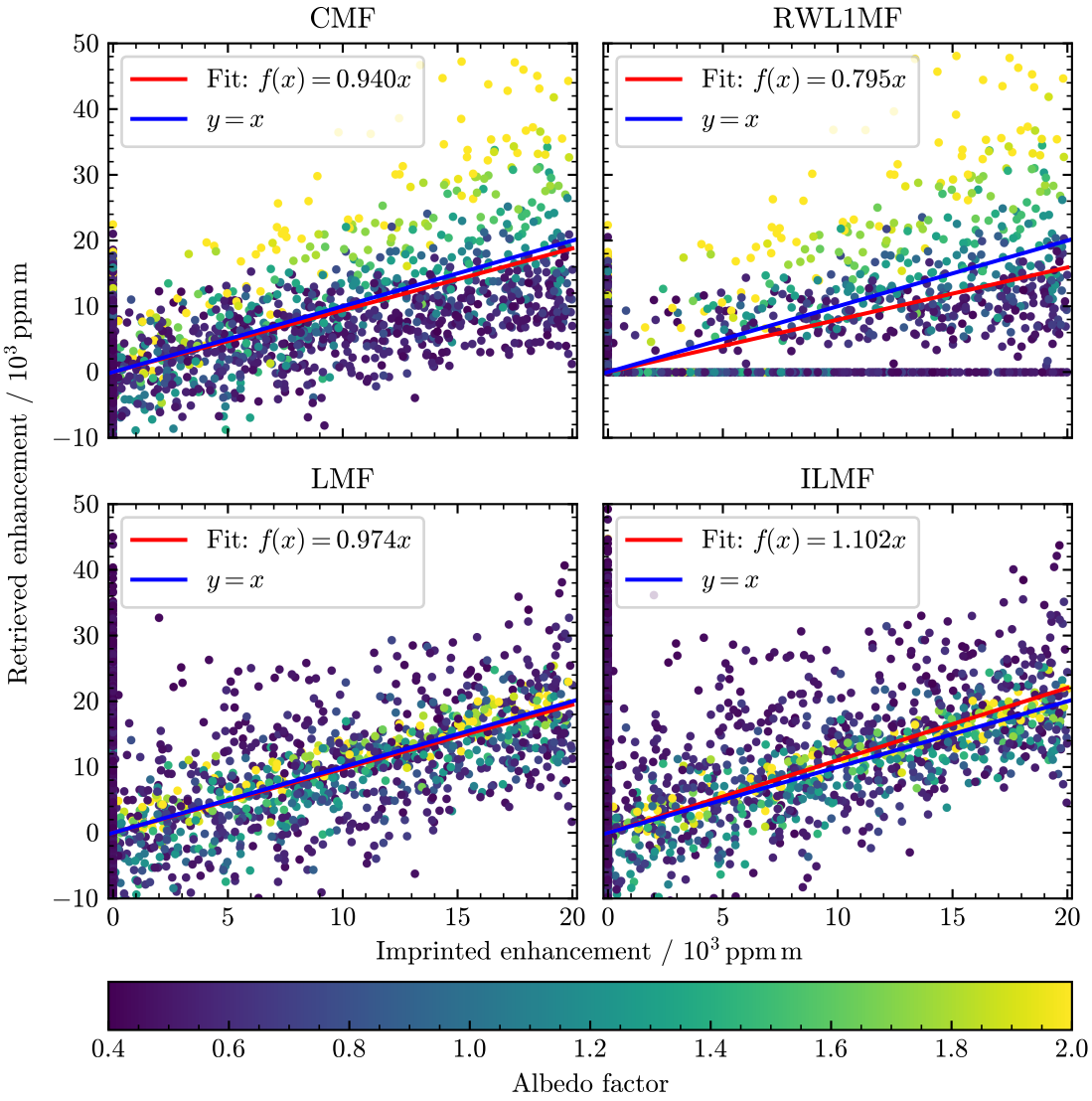

Fig. 4.3. Scatter plots of data with artificially imprinted enhancements retrieved using four different matched filters, all without albedo correction. The color bar encodes each pixel's albedo. A no-intercept linear regression was performed to indicate the general matched filter performance, even though this has to be interpreted with caution.

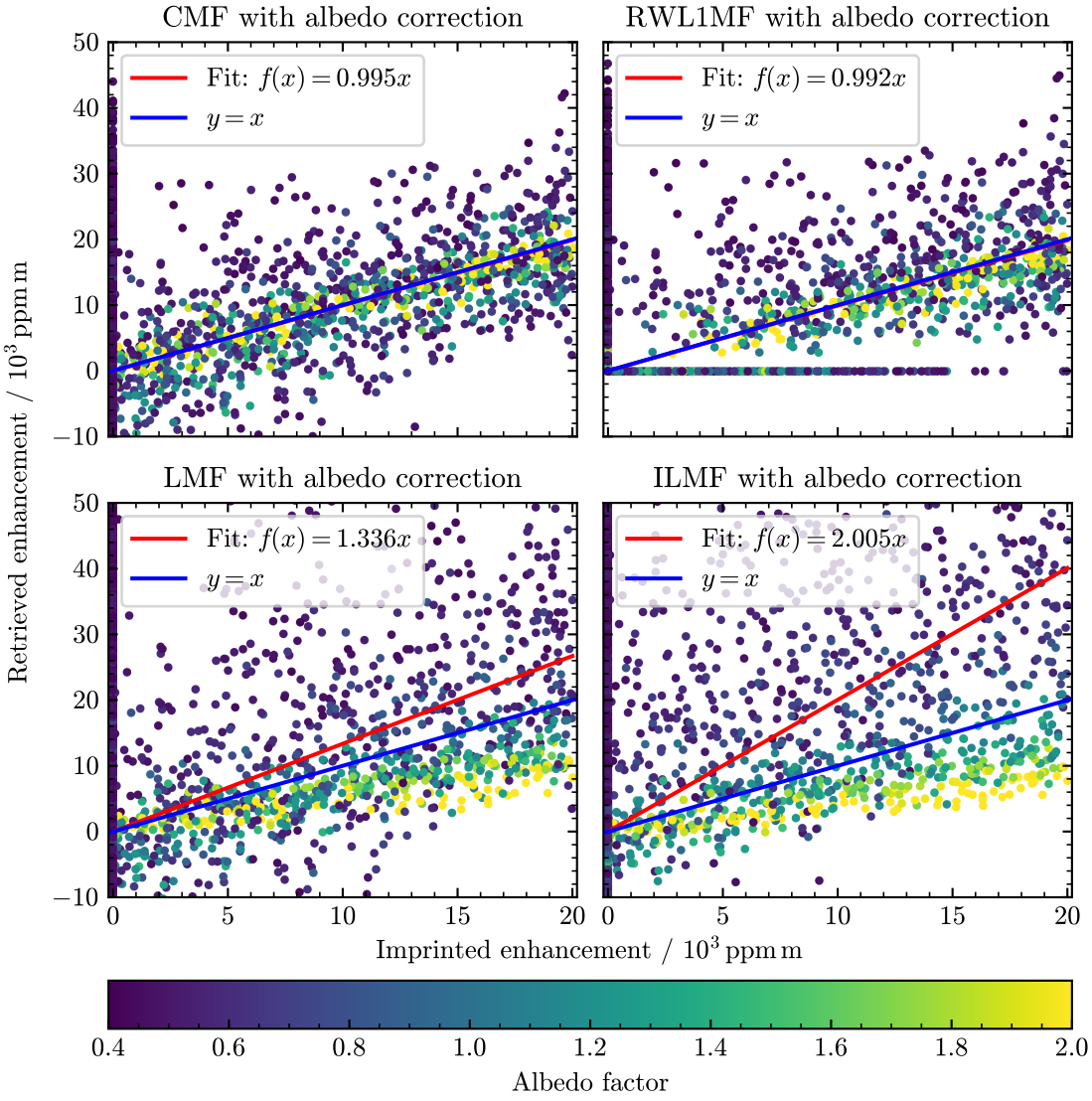

Fig. 4.4. The same as Fig. 4.3, but this time with albedo correction.

The reason for this outcome shall be illustrated in the following. In general, an unusually bright observed spectrum can be modeled as

$$\boldsymbol{L}_p \approx A_p \cdot \boldsymbol{\mu} \odot \exp(\alpha_p \cdot \boldsymbol{s}_p)\,, \tag{4.45}$$

where $A_p > 1$ is a factor scaling the whole spectrum to account for its brightness, comparable to the albedo factor r_p in Section 4.4.1. This means that seen in *absolute* terms, the absorption signature is stronger, because according to the Beer-Lambert law (2.19), the absorption strength is relative to the initial radiance, which is larger here. In the case of CMF and RWL1MF, this stronger absorption signal stays as is, and has to be corrected for using the albedo factor. On the other hand, in the case of LMF and ILMF, the logarithm of the spectrum is taken, which converts the albedo *factor* into an albedo *addend*:

$$\ln \boldsymbol{L}_p \approx \mathbf{1} \ln A_p + \boldsymbol{\nu} + \alpha_p \cdot \boldsymbol{s}_p\,. \tag{4.46}$$

The pixel's albedo A_p then barely plays a role in the LMF and ILMF. Oddly, Pei et al. (2023) claim to have found that an albedo correction is also needed for the LMF and ILMF, but they do not describe how they perform this albedo correction.

Based on these retrievals of simulated data, one might anticipate that the albedo-corrected CMF and RWL1MF would also perform equally well with real data, slightly outperforming the LMF. The ILMF, furthermore, tends to overestimate enhancements by approximately 10% on average. This is likely due to the exclusion of strongly enhanced pixels in the calculation of the background statistics. Occasionally, pixels with a high SNR might be excluded, even if the high SNR is merely a random fluctuation rather than a true enhancement. This skews the background statistics, leading to overestimated enhancements.

When examining real data, it becomes evident that the albedo-corrected CMF and RWL1MF do not perform equally well as suggested by the artificial data retrievals. Figure 4.5 presents a zoomed-in image of a methane plume from a coal mine ventilation shaft in the USCB. These data were collected during a measurement campaign in the USCB in 2022 (Knapp et al., 2023), and the matched filter retrieval used a UAS ranging from 2053 nm to 2396 nm (as in Knapp et al., 2023; Knapp, 2024).

Figure 4.5 shows an example of how the CMF consistently retrieves the smallest enhancements, while the enhancements in the plume for both RWL1MF and LMF are quite similar. Moreover, the ILMF exhibits much stronger enhancements, likely due to skewed background statistics, as previously discussed. Therefore, the LMF was chosen for all subsequent data retrievals. It was favored over the RWL1MF, despite their similar performance, because of its more reasonable physical background assumptions (i.e., the lognormal distribution of observed spectra), its lower computational demands, and its inherent simplicity.

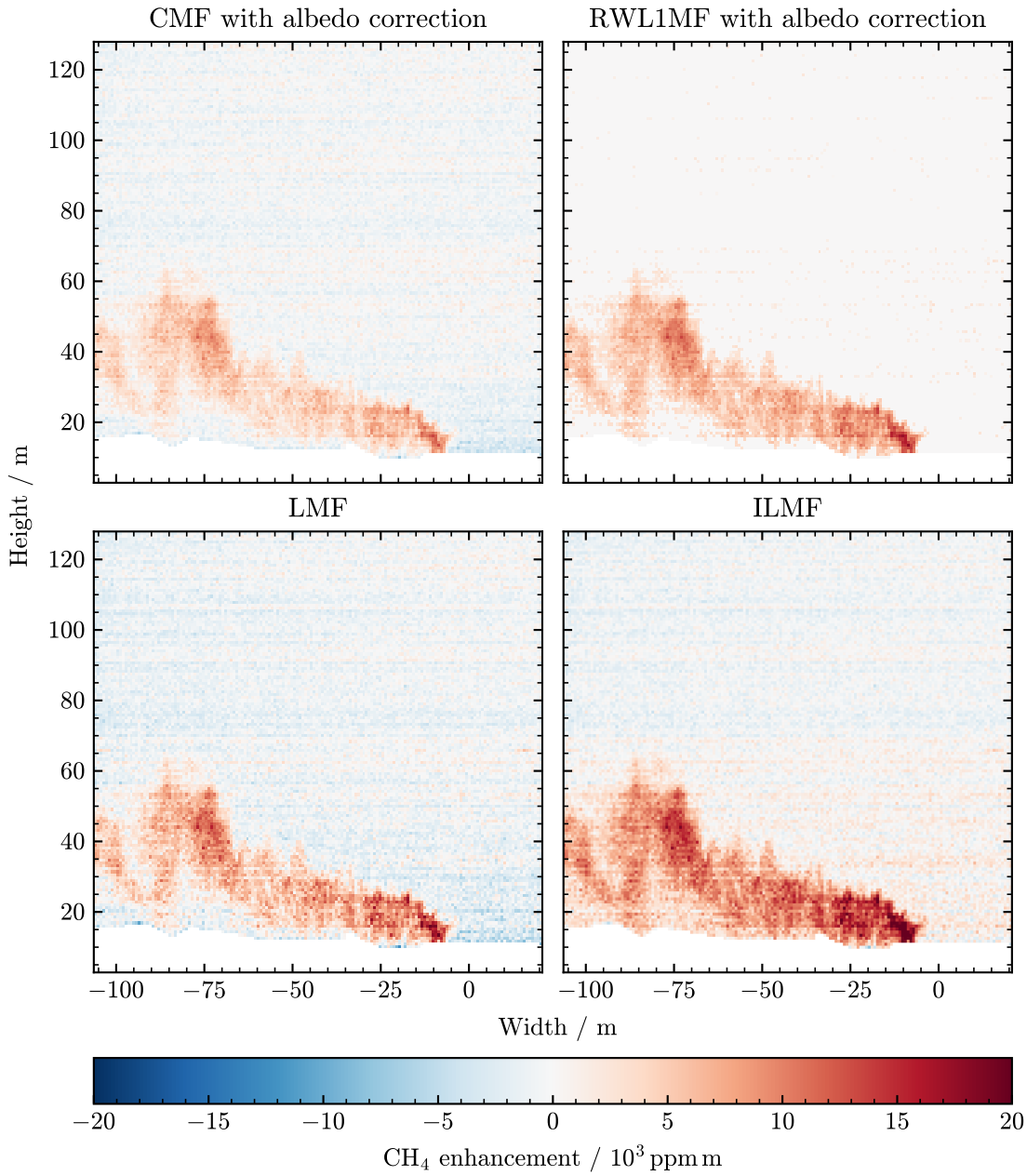

Fig. 4.5. Zoom on an image captured during the USCB measurement campaign in 2022 retrieved with the CMF with albedo correction, RWL1MF with albedo correction, LMF without albedo correction, and ILMF without albedo correction.

5 Overview of the 2024 Methane Remote Sensing Campaign at Madrid Landfills

Most of the data presented in this thesis was collected during a measurement campaign conducted near Madrid, Spain, from June 27 to July 9, 2024. Each day, hyperspectral images in the SWIR range were captured using one or both of the SWIR-observing HySpex cameras (see Section 3.1). The campaign primarily focused on the Pinto landfill[1], with the last two days dedicated to observing the Valdemingómez landfill[2]. The cameras were positioned at five different locations around the Pinto landfill (H1[3], J1, K1, Monastery, and Mirador) and two locations around the Valdemingómez landfill (L1 and L2), all marked in Figs. 5.1 and 5.2.

The HySpex SWIR-384 typically had a scanning rate on the order of 75 s. The HySpex Mjolnir typically had a scanning rate of 3 min to 5 min. Until June 30, tests with different gain and frame averaging modes were performed with the Mjolnir. Therefore, July 1 is the first day on which a long, consistent time series of Mjolnir observations exists. On July 5, the SWIR-384 camera stopped functioning, so all subsequent measurements were conducted using only the Mjolnir camera.

During all the measurements, wind data was recorded using a wind lidar (see Section 3.2). From July 3 to July 7, the lidar was permanently positioned at the administrative facilities of the Pinto landfill (indicated by the green marker in Fig. 5.1). On the other days, the lidar was positioned at a maximum distance of 150 m from the camera(s).

Below are remarks on the different measurement positions:

H1 On our first day scouting the fields around the Pinto landfill, we found this hill, which is relatively close to the landfill, requiring a large horizontal scanning angle. Due to difficult car access, we did not return to this spot after the first day. On this first day of measurement, a significant amount of Saharan dust in the atmosphere made the sky very hazy and consequently very bright in the SWIR range.

J1 This was the preferred spot for days when the wind was directed north, northwest, south, or southeast.

[1] PRTR-España coordinates: 40.257118° N, 3.637550° W

[2] PRTR-España coordinates: 40.336427° N, 3.590375° W. Technically, there are several landfills with different names located inside "Valdemingómez Technology Park" ("Parque tecnológico de Valdemingómez"), which also includes a wastewater treatment plant, biomethanation plant, and waste incineration plant. For simplicity, the term "Valdemingómez landfill" is used in the following.

[3] There is no deeper meaning behind these labels, which came about for historical reasons.

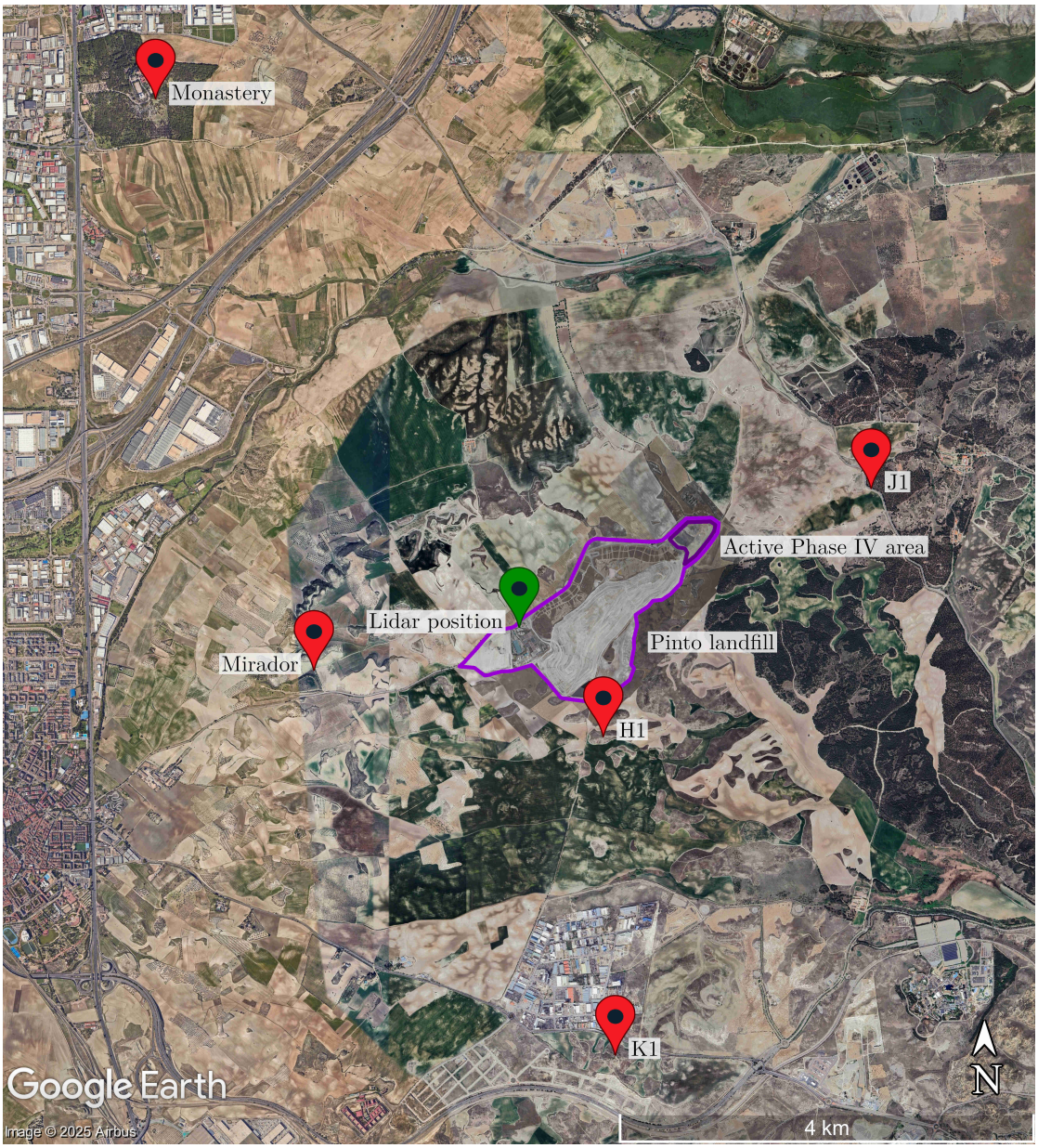

Fig. 5.1. The Pinto landfill outlined in pink, with the active Phase IV area at the northeast end outlined in purple. The five observation positions are shown with red markers, and the position of the lidar between July 3 and July 7, 2024, with a green marker. Base image by Airbus/Google Earth, with an inset photograph of the Pinto landfill captured at the time of the campaign by the German Aerospace Center (DLR). Additional annotations added by the author.

Fig. 5.2. The approximate outlines of the whole Valdemingómez Technology Park complex (pink) and the probably active landfill area (purple) are taken from Krautwurst et al. (2024). The two observation positions are shown with red markers. Base image by Airbus/Google Earth and additional annotations added by the author.

K1 This hill's elevation provides a downward view onto the Pinto landfill. In the background, the city of Madrid is visible, requiring a few pixels above the landfill to be masked out. A more problematic issue is the distant Sierra de Guadarrama mountain range, which is faintly visible to the naked eye but much clearer in the SWIR range. This affects the retrieval algorithm as the light path deviates significantly from the single scattering approximation. Additionally, an overhead electricity wire near the camera setup restricted the viewing angle or interfered with the FOV on one side of the image. This spot is ideal when the wind is blowing from the west or east.

Monastery Located over 6 km from the landfill, this spot is relatively distant. This was the preferred position for days with northeast or southwest wind.

Mirador Similar to K1, this elevated spot offers a downward view onto the landfill. A forest in the background of the images influences the light path significantly, similarly to the Sierra de Guadarrama.

L1 This was the first suitable position found when approaching the Valdemingómez landfill. The active part of the landfill is not directly visible, hidden behind a hill.

L2 After thoroughly scouting the area around the Valdemingómez landfill, this spot appeared to be the best for observation, because the active part of the landfill is directly visible.

Figure 5.3 depicts a timeline of all measurements, including satellite observations by EnMAP and GHGSat. Viewing azimuth directions are indicated by blue arrows, and pictograms depict the "average" weather condition for each day.

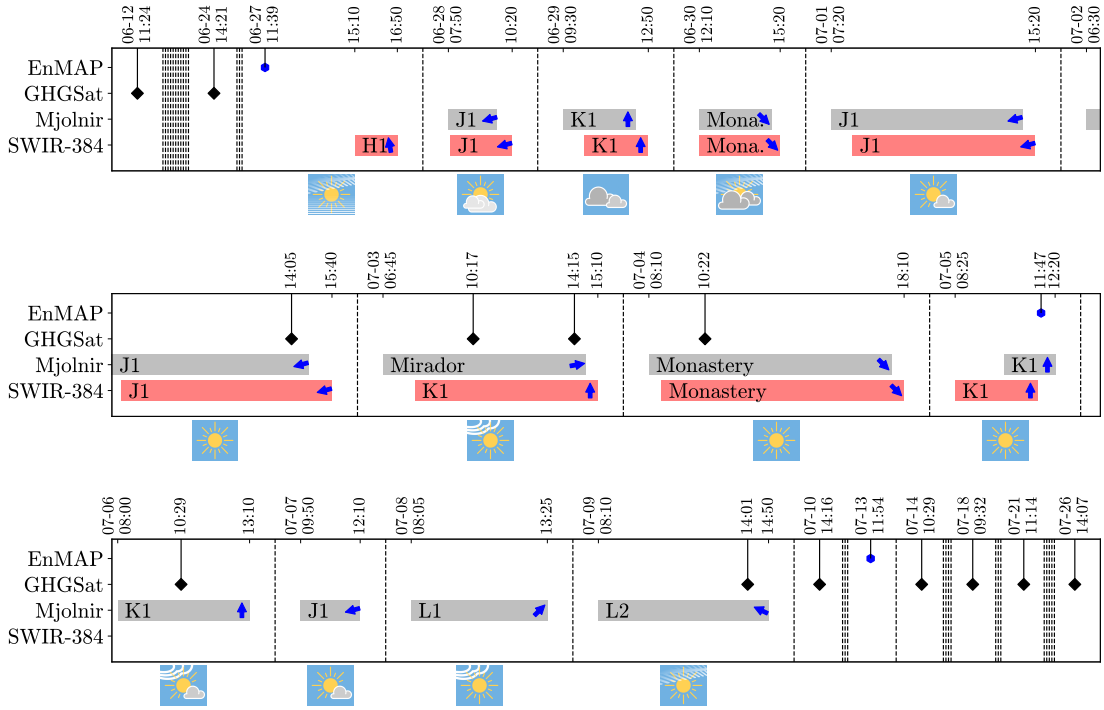

Fig. 5.3. Timeline of all data collected with the HySpex SWIR-384 and HySpex Mjolnir during the campaign, as well as satellite observations by EnMAP (blue hexagon) and GHGSat (black diamond) in the months of June and July. Blue arrows indicate the viewing azimuth direction. Pictograms show the "average" weather condition for each day. Figure adapted from Lukas Häffner (personal communication). Pictograms by meteoblue (https://content.meteoblue.com/en/research-education/specifications/standards/symbols-and-pictograms).

6 Methane Emissions at the Pinto Landfill

This chapter presents the key findings from the data collected at the Pinto landfill. Section 6.1 introduces the typical appearance of a retrieved image showing methane enhancement and explains what can be observed in these images. Section 6.2 discusses the dust clouds visible in many images, their origins, and how they affect the matched filter retrieval. Section 6.3 examines the observed methane over the landfill, aiming to characterize its spatial and temporal distribution. Section 6.4 is a small excursion that presents a method to extract the wind velocity perpendicular to the camera's line of sight from movement of dust clouds in the images. Finally, Section 6.5 estimates methane emission rates using a simple one-box model.

This chapter focuses on data interpretation and obstacles that had to be overcome during data analysis. Given these difficulties, the goal is to demonstrate what information can and cannot be extracted from the data. For this purpose, only data collected by the HySpex SWIR-384 camera on July 2 and July 4, 2024, is presented, as these were the days with the best measurement conditions (see Fig. 5.3). All data showcased here was retrieved using the LMF.

6.1 Exemplary Plots of Methane Enhancement

Figure 6.1 shows an exemplary methane image from the Pinto landfill retrieved using the LMF. Non-sky areas (i.e., ground and vegetation) are plotted as the observed intensity in the first channel of the retrieval window on a color scale ranging from blue to yellow to provide a sense of the scenery. For all sky pixels, the plot shows the retrieved methane enhancement in ppm m using the color scale on the right side of the plot. The width and height given on the x- and y-axis correspond to the plane of expected emissions, i.e., the landfill. These coordinates are derived from the viewing geometry but are subject to uncertainty, as the distance between camera and the observed methane enhancement can only be estimated (see Section 6.5.2 for an approximate uncertainty estimate). The origin $(0, 0)$ is the position that was used as a reference point to calculate the VEA and viewing azimuth angle (VAA), but has no further significance.

In the foreground of the image agricultural fields are visible. A forest is observable on the left in dark blue, and individual trees and bushes are scattered across the fields as dark blue spots. The bright yellow area in the center is the closed area of the landfill, which is covered with gravel. Figure 6.2 depicts the same scene as a normal RGB image captured at a different time.

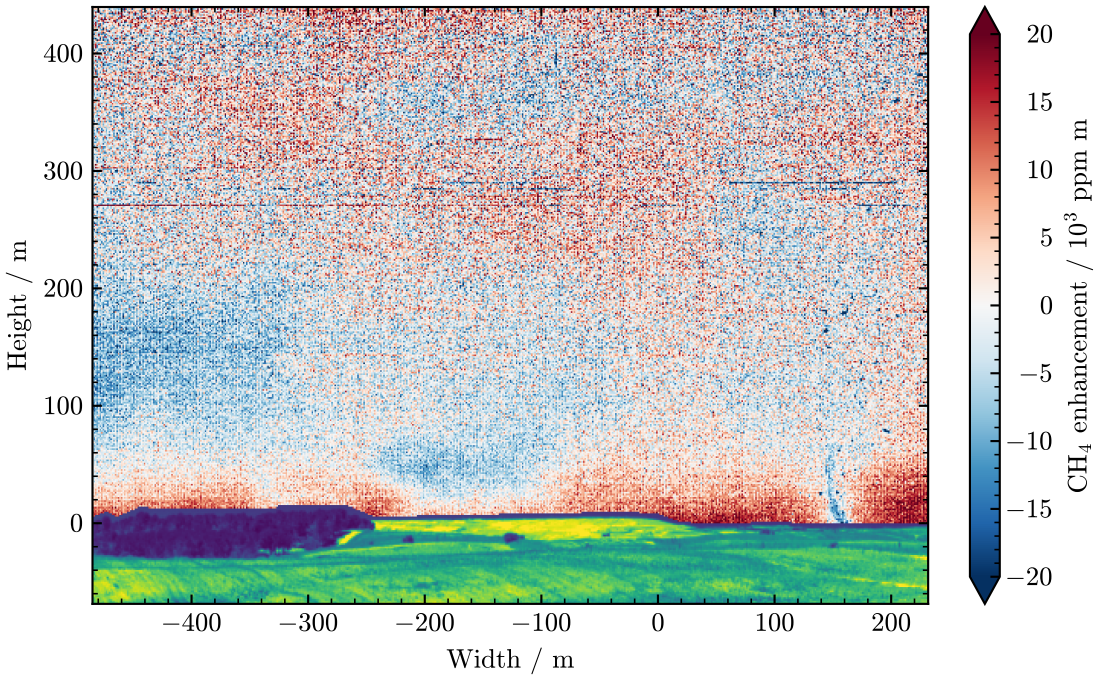

Fig. 6.1. Methane enhancement above the Pinto landfill on July 2, 2024, at 12:23 UTC, retrieved using the LMF in the wavelength range from 2190 nm to 2396 nm

Fig. 6.2. RGB image of the view from position J1, which was used for observations on July 2, 2024, with the approximate FOV of the measurement shown in Fig. 6.1 framed red

The dark blue thin line at the horizon in Fig. 6.1 consists of sky pixels but was masked out from the retrieval data. This precaution ensures that no ground pixels are included in the retrieval, as this would result in inaccurate enhancements for these pixels since the light path for ground pixels differs significantly from that of sky pixels, requiring a very different UAS. It would also influence the average spectrum ($\boldsymbol{\mu}$ or $\boldsymbol{\nu}$) and the covariance matrix ($\mathbb{C}$) used in the matched filter. However, this effect would be minimal, as sky pixels would vastly outnumber any mistakenly included ground pixels.

In Fig. 6.1, methane enhancement is visible close to the ground, horizontally separated by two areas of negative enhancement (shown in blue) in the middle and at the far right, which are dust clouds. By shortening the light path they reduce the total observed methane column and thus appear as negative enhancements. Additionally, dark spots are visible in and above the right dust cloud, which are likely storks flying over the landfill (Vicente-Hernández et al., 2023), also shortening the light path. Higher up in the sky, there are areas of both predominantly positive and negative methane enhancements, but these are not as pronounced as the enhancements close to the ground. These areas are characterized by higher noise, meaning even in areas of predominantly positive enhancement, there are pixels with negative enhancement and vice versa. This higher noise is due to the sky darkening with increasing VEA, and the structure is likely caused by heterogeneous aerosol concentrations in the sky, a result of the hot and dry summer climate.

The image also exhibits a few one pixel thin horizontal stripes, mostly at heights between 270 m and 300 m. These stripes are caused by bad detector pixels which sometimes function properly and sometimes do not and which were not masked out by the bad pixel map, appearing as stripes due to the camera's scanning operation. The incorrect radiance values reported by these defective pixels affect the matched filter, resulting in improper enhancements. However, these stripes do not significantly impact the overall results in the retrieved image for two reasons. First, they only occur high up in the image and do not affect areas of enhanced methane concentration close to the ground. Second, only very few pixels are affected in total, so they do not significantly influence the mean spectrum ($\boldsymbol{\mu}$ or $\boldsymbol{\nu}$) and covariance matrix ($\mathbb{C}$).

Figure 6.3 shows another image from the same day, also retrieved using the LMF. At a height of ∼100 m, clouds are visible on the right. These clouds are captured as very negative enhancement by the matched filter because they significantly shorten the light path, much like dust clouds, but in this case to a more drastic extent. This reduces the observed total methane column substantially. The retrieval of methane enhancement in front of clouds could be improved by using a version of the differential matched filter with clustering (Knapp, 2024). A dust cloud is visible in the center of the image. The presence of this dust cloud is confirmed by the unusually high radiance in the respective pixels, which can be seen in the ground pixels at a height of ∼0 m and below, just beneath the dust cloud shown in blue in the sky. The artifact in the bottom right corner of the image is a tractor that was driving through the FOV right in front of the camera.

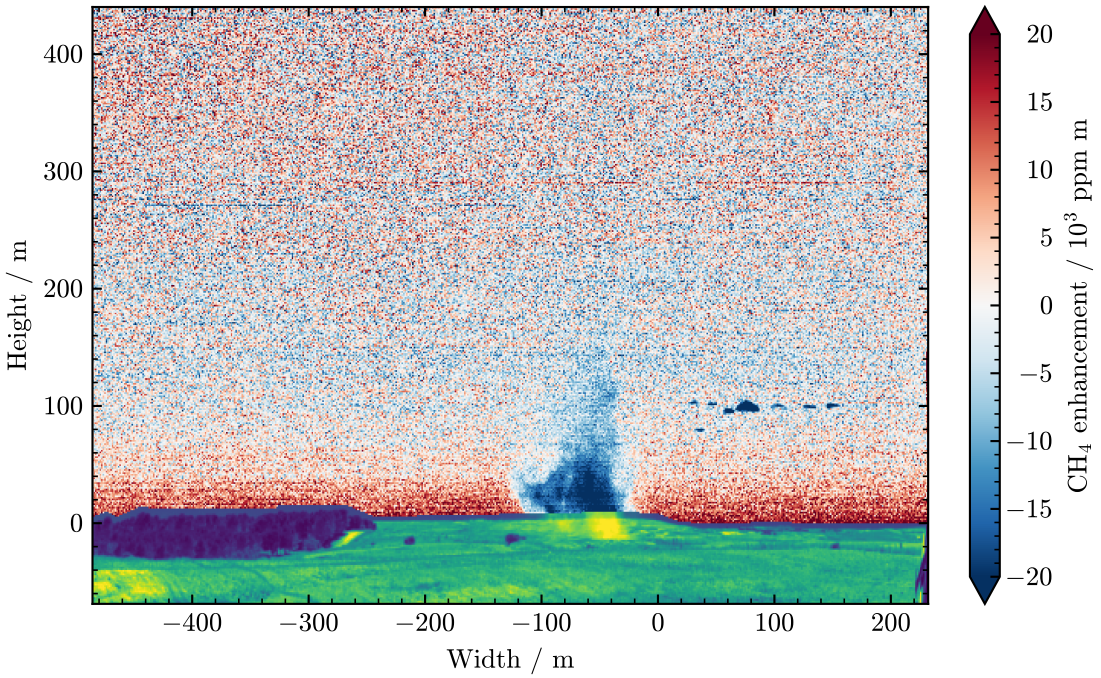

Fig. 6.3. Methane enhancement above the Pinto landfill on July 2, 2024, at 14:54 UTC, retrieved using the LMF in the wavelength range from 2190 nm to 2396 nm

Figure 6.4 shows another interesting phenomenon. It was captured in the morning of July 2, 2024, at 8:31 UTC. It uses the same color scale as the previous figures, but the noise high up in the sky is much stronger. This increased noise can be explained by the lower radiance from the sky at this time of day, resulting in less bright observed spectra and a smaller signal-to-noise ratio. Interestingly, on July 4, 2024, the sky became darker over time, which could be due to a reduction in atmospheric aerosols. Consequently, the noise in the images increases slightly over time. The same behavior is visible in retrievals of CO_2 in the same observations, supporting the idea that these variations are due to changes in sky brightness or light path effects, rather than changes in methane concentration.

Of all the effects influencing a retrieved image, dust clouds are most important in our case. As the majority of our images contain at least one dust clouds, this topic is treated in more detail in the following.

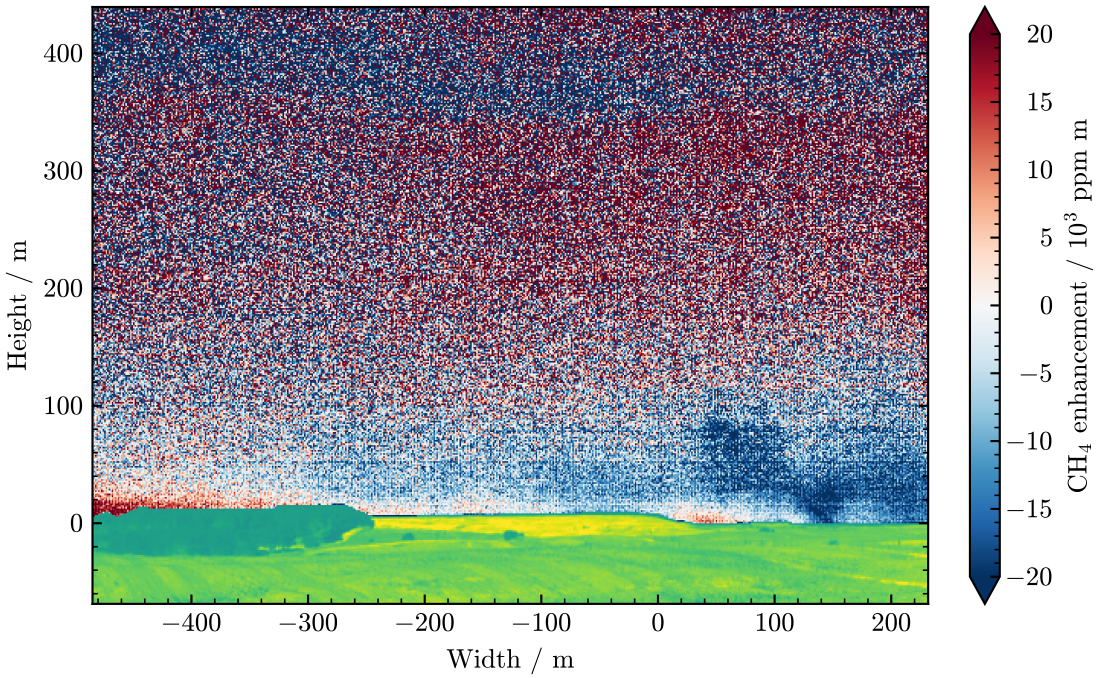

Fig. 6.4. Methane enhancement above the Pinto landfill on July 2, 2024, at 8:31 UTC, retrieved using the LMF in the wavelength range from 2190 nm to 2396 nm

6.2 Dust Clouds in the Images

The summer climate in and around Madrid is very hot and dry, causing a lot of dust in the air, which is captured in our images. These dust clouds were also recorded by the GoPro camera that was set up to document the weather conditions during measurements. In the data presented so far, most images contain at least one area which is clearly affected by dust. This section explains how different dust clouds appear in a retrieved image of methane enhancement, and how they can influence the retrieval of methane enhancements in general.

The dust clouds captured in our imagery have different causes. Sometimes, a dust cloud is formed by a wind gust dragging up particles from the ground. These dust clouds can have various shapes and sizes, ranging from a few to a few hundred meters. We see that they often start small just above the ground and over time increase in size as they move further up into the air and get diluted by turbulence. Similarly, dust clouds can form through human activity, which is mostly vehicles that drive on dusty ground and drag up particles behind them. In our case, these are cars that drive on the covered part of the landfill, which has gravel roads on top, or tractors or harvesters that drive on the agricultural fields in front of the landfill. A harvester also creates a lot of dust

by throwing the separated and chopped straw back onto the field. A further source of dust clouds are dust devils—small, short-lived whirlwinds that form from pockets of hot air spontaneously rising from the ground and starting to circulate, thereby creating an updraft sucking in new hot air at the ground. A retrieved image of a dust devil is depicted in Fig. 6.5. The different dust clouds also differ in their composition: dust from gravel on the covered part of the landfill, dust from soil on the agricultural fields, and dust from straw produced by a harvester.

In Figs. 6.1, 6.3 and 6.5, that were presented so far, dust is always present as negative enhancement as it shortens the light path. In theory, this is not necessarily always the case. On the one hand, it is thinkable that a dust cloud lengthens the light path, e.g., if the dust cloud is farther away than the average viewing distance (even though this is not the case for all the causes of dust clouds listed above), or if the light path within the dust cloud is very long. On the other hand, the spectrum of the dust cloud can mess with the matched filter retrieval itself. Not only do dust clouds exhibit high radiances and change the effective light path, they can also exhibit a spectral structure. Even when this is not a narrow absorption structure as, e.g., the absorption of methane, a broad band structure can also affect the matched filter result. This is especially the

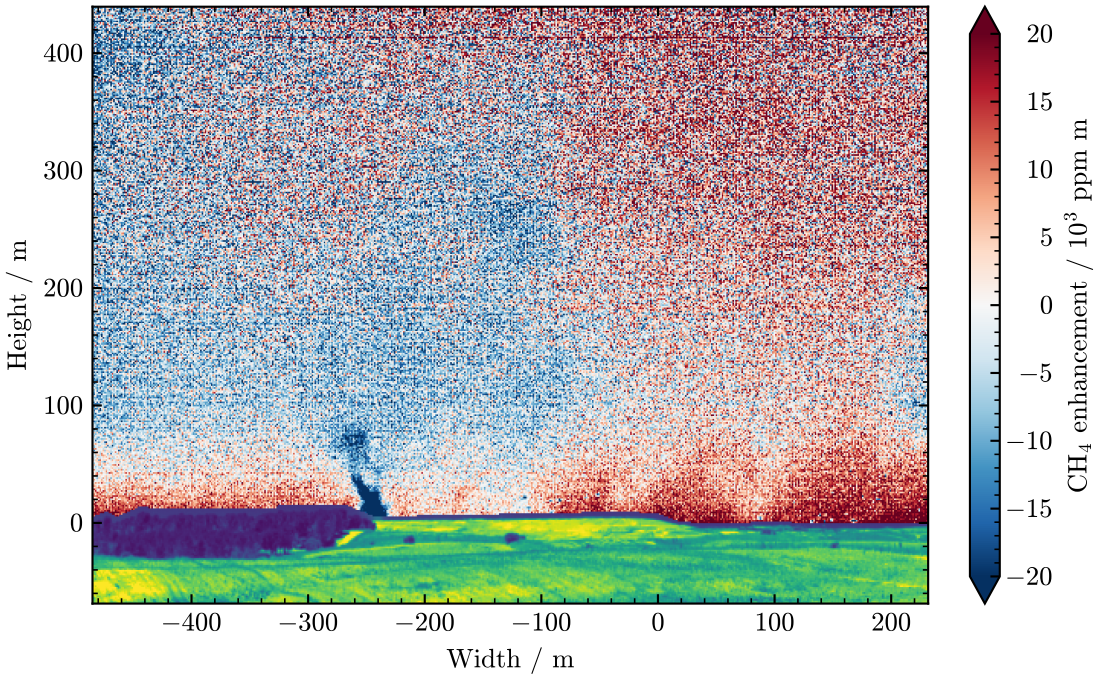

Fig. 6.5. A dust devil clearly visible as negative methane enhancement, captured on July 2, 2024, at 13:29 UTC

case when using a wider retrieval window in the matched filter. Knapp et al. (2023) and Knapp (2024) used a methane retrieval window from 2053 nm to 2396 nm. While from 2053 nm to 2190 nm there is nearly no methane absorption (see Fig. 2.1), this wavelength range was still included in the retrieval window to get a more informed estimate of each pixel's albedo factor (see Section 4.4.1), which was used to correct for an albedo bias in the enhancements[1] (Foote et al., 2020). Using this same retrieval window for the retrieval of observations from the Pinto landfill results in mineral dust clouds over the landfill hill itself (e.g., the dust devil in Fig. 6.5) to show as very high methane enhancements. Dust clouds from dirt or straw, produced by harvesters or other machines on the agricultural fields, remain very negative enhancements, as should be the case due to light path shortening. This difference can be explained by the different composition of the dust clouds, and their different broad band spectral features. Because of this, in this thesis methane was retrieved in the spectral window ranging from 2190 nm to 2396 nm. This range encompasses all significant methane absorption structures, but is less susceptible to broadband aerosol effects due to its narrower scope. Using this spectral window for retrieval consistently results in dust clouds appearing as very negative enhancements, which is expected due to the shortening of the light path. However, the influence of aerosol spectral structures in this retrieval window cannot be entirely dismissed. Since the LMF was used, no albedo correction is necessary (see Section 4.7).

Apart from spectral features of dust clouds possibly affecting the matched filter retrieval, in our case, a dust cloud in an image generally has two effects. Pixels with dust have a shortened light path compared to the average pixel light path, and thus the enhancement in that pixel comes out very negative, even though there might actually be a significant amount of methane in that pixel, behind or in front of the dust cloud. But also, all pixels' spectra go into the mean spectrum $\boldsymbol{\mu}$ or $\boldsymbol{\nu}$ and the covariance matrix $\mathbb{C}$, which in turn are used to calculate the enhancements in all pixels. Thus, a dust cloud, which exhibits a spectrum systematically different from non-obstructed pixels, influences these variables. Still, this influence is only minor as the number of pixels with dust in them is only a small fraction of the total number of pixels in an image.

This effect of a dust cloud on the enhancements of the pixels not containing any dust can be seen in Fig. 6.6. For an exemplary image with an especially strong dust cloud, the LMF retrieval was once run normally (visible in Fig. 6.5), and once after masking out the area compromised by dust. The quotient of the two images shown in Fig. 6.6 scatters around 1, and there are certain areas where it is predominantly greater than 1

[1] One might also use two different spectral windows for the matched filter retrieval and for the albedo factor calculation, but the author is not aware of any publication that uses such an approach. This would have two effects. On the one hand, it would eliminate the need for a relatively broad retrieval window, which is otherwise used so that the albedo factor is not too strongly influenced by methane absorption. On the other hand, the selection of the albedo factor spectral window needs to be done cautiously as a pixel's albedo factor might then not be representative for the retrieval window spectrum if it is spectrally too far away.

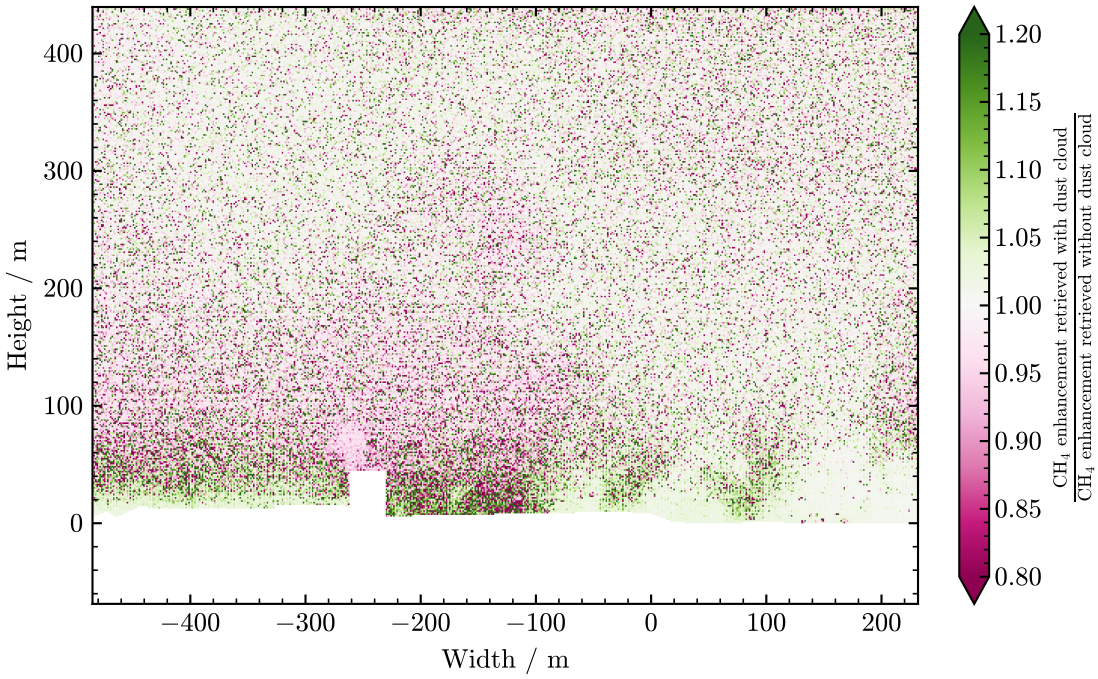

Fig. 6.6. The quotient of the methane enhancement retrieved with an especially strong dust cloud in the image (Fig. 6.5) and retrieved with the dust cloud masked out beforehand

or predominantly smaller than 1. Most importantly, in the area just above the horizon, where true methane enhancements are detected (see Fig. 6.5), the enhancement retrieved with the dust cloud in the image is larger than without the dust cloud. This is expected, because with the dust cloud in the image, the mean spectrum exhibits slightly weaker methane absorption features, making methane absorption in pixels with true enhancement stronger in relation. Yet the difference in this area of high methane enhancements rarely exceeds 5%, and lies mostly around 2% or 3%. This disparity is negligible in comparison to the effect that, e.g., the choice of matched filter has on the enhancement (see Section 4.7). Furthermore, it is also negligible in comparison to the uncertainties introduced by converting the slant column enhancement into absolute amounts of methane or by deducing an emission rate (see Section 6.5.2). Because of this, the effect dust clouds have onto the enhancement in the rest of the image can be accepted like this.

6.3 Enhanced Methane Concentrations in the Images

All the retrieved images show some methane enhancement close to the ground. Except for some images from the morning of July 2, 2024 (e.g., Fig. 6.4), the enhanced area extends horizontally across the entire image, interrupted only by dust clouds that inhibit the detection of methane. The vertical extent of the detected methane accumulation is initially small in the morning but increases over time, reaching approximately 50 m to 70 m on July 2, 2024, and approximately 200 m to 250 m on July 4, 2024. The detected methane concentration exhibits a vertical gradient, with the strongest enhancements occurring near the ground, just above the landfill, and decreasing with height.

Given that this gradient extends to the horizon and typically lacks distinct structures unless dust clouds are present, it seems plausible that the observed phenomenon is attributable to a light path effect rather than elevated methane concentrations above the landfill. This light path effect could stem from an incorrect geometric calibration of the camera and its FOV, meaning the presumed viewing geometry (i.e., VEA and VAA) might be inaccurate. As a result, the light path just above the horizon might be longer than anticipated, leading to an apparent methane enhancement due to the extended light path, rather than an increase in methane concentrations above the landfill.

To test this hypothesis, CO_2 was retrieved from the same observation within the spectral range of 1967 nm to 2260 nm. The result of the same observation as shown in Fig. 6.5 is depicted in Fig. 6.7. The dust devil in the image also appears as a strongly negative enhancement due to a shortened light path, and the right side of the image generally shows stronger enhancements than the left, similar to the methane image, suggesting aerosol effects. However, the CO_2 image does not show enhancements just above the horizon. This indicates that the enhancements above the horizon in the methane image are due to increased methane concentrations above the landfill and not caused by any light path effects, which would also appear in the CO_2 image.

The increase of methane concentrations over the course of the day might be a diurnal flux pattern. Delkash et al. (2022) find a positive correlation of methane flux with ambient temperature that is strongest under unstable atmospheric conditions. This would fit the observations presented here, as clear, sunny days make an especially unstable atmosphere, and temperature was continuously rising from morning to afternoon. Still, this interpretation is to be taken with caution, as we have no further evidence supporting this theory.

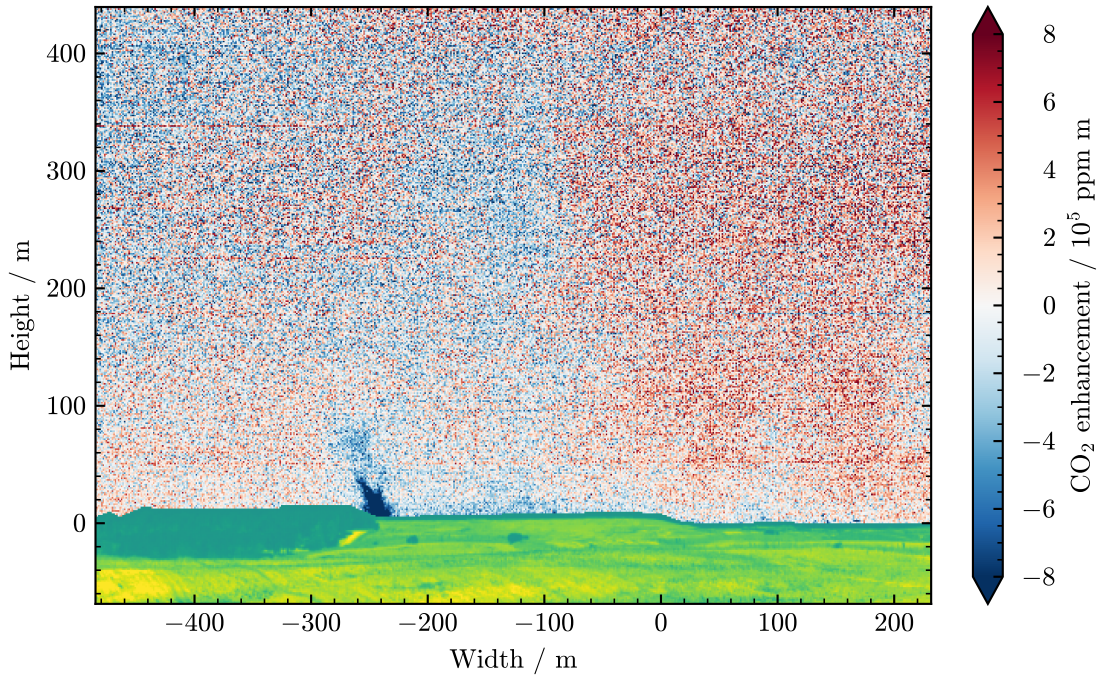

Fig. 6.7. CO_2 enhancement retrieved using the LMF in the wavelength range of 1967 nm to 2260 nm for the same scene as depicted in Fig. 6.5

6.4 Extraction of Wind Velocity From Retrieved Images

Due to the high temporal resolution of our images on the order of one minute, it is possible to see dust clouds moving, i.e., one and the same dust cloud shows at different positions in two or three consecutive images. An example for this is shown in Fig. 6.8. Using the horizontal positions of the dust cloud and the corresponding times of observation a calculation of the wind velocity perpendicular to the camera's line of sight is possible. A demonstration of this is presented in the following.

The extraction of the wind velocity perpendicular to the line of sight consists of five steps:

1. Determine the horizontal center positions of a dust cloud in two consecutive images in terms of frame numbers f_0, f_1.

2. Calculate the azimuth angle between them as $\theta = (f_1 - f_0) \cdot \theta_f$, where $\theta_f = 0.73\,\text{mrad}$ is the opening angle of one frame.

3. Calculate the distance between the positions as $w = d \cdot \tan\theta$, where d is the estimated distance between camera and dust cloud.

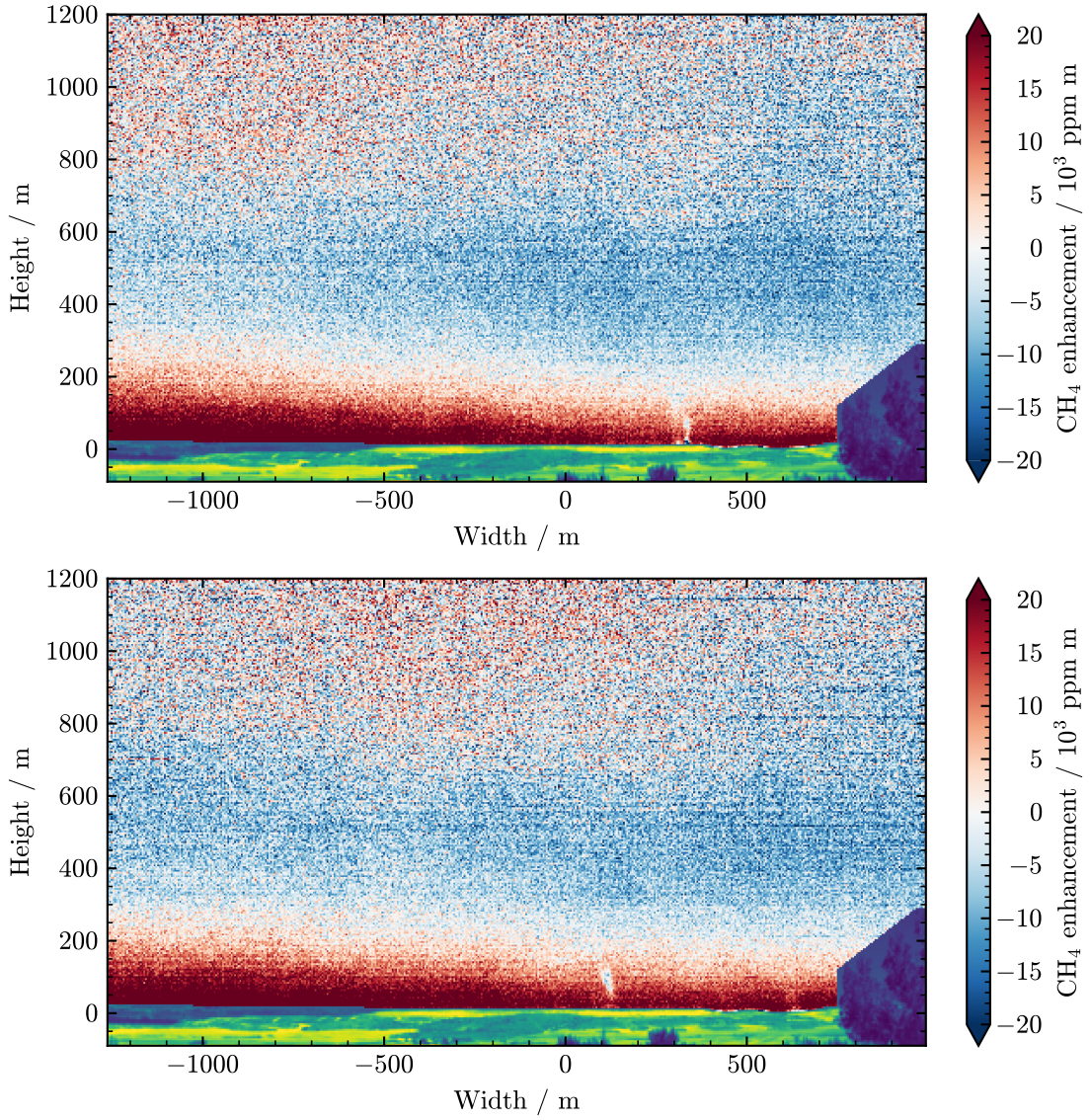

Fig. 6.8. Top: Image from July 4, 2024, at 12:54:22 UTC. Bottom: The subsequent image from 12:55:33 UTC. During ∼1 min the dust cloud moves ∼200 m to the left.

4. Calculate the time stamp T_i for each dust cloud i as $T_i = t_{i0} + (t_{i(F-1)} - t_{i0}) \cdot f_i/F$, where t_{i0} is the time stamp of the first frame of the image, $t_{i(F-1)}$ is the time stamp of the last frame of the image, and F is the total number of frames per image.

5. Calculate the wind velocity perpendicular to the line of sight as $v_\perp = w/(T_1 - T_0)$.

While, of course, all input variables are associated with an uncertainty, the uncertainties of f_0 and f_1 as well as d dominate. The uncertainties of f_0 and f_1 are estimated manually depending on the shape of the dust cloud, and the uncertainty of d is estimated to be $\Delta d = 0.1 \cdot d$ for July 4, 2024. Using Gaussian error propagation, the squared uncertainty of w then is

$$(\Delta w)^2 = (\Delta d \cdot \tan\theta)^2 + \left(\frac{d}{\cos^2\theta} \cdot \theta_f\right)^2 \cdot ((\Delta f_0)^2 + (\Delta f_1)^2)\,, \tag{6.1}$$

where Δd, Δf_0, and Δf_1 are the uncertainties of d, f_0, and f_1. The uncertainty of T_i is

$$\Delta T_i = \frac{t_{i(F-1)} - t_{i0}}{F} \Delta f_i\,. \tag{6.2}$$

The squared uncertainty of $v_\perp$ then is

$$(\Delta v_\perp)^2 = \frac{(\Delta w)^2}{(T_1 - T_0)^2} + \frac{w^2}{(T_1 - T_0)^4}((\Delta T_0)^2 + (\Delta T_1)^2)\,. \tag{6.3}$$

Figure 6.9 shows the wind velocity perpendicular to the line of sight that was extracted from the dust cloud shown in Fig. 6.8. For comparison, it furthermore shows the wind velocity perpendicular to the line of sight measured by the wind lidar, which on that day was positioned at the Pinto landfill facilities, meaning it was probably only a few hundred meters away from the estimated positions of the dust cloud. The dots in Fig. 6.9 are single data points, and the lines are rolling averages over $\sim$1.18 min, which is the time difference between two consecutive observations. The horizontal error bar extents from the time of the first to the second observation of the dust cloud, and the vertical error bar is calculated from Eq. (6.3).

The wind velocities measured with the wind lidar compare well to the wind velocity extracted from the images. Of course, this is not least due to the wind velocity fluctuating significantly from one lidar measurement point to the next, resulting in a big spread.

This demonstrates that in theory, it might be possible to extract a methane emission rate solely from two hyperspectral images if they exhibit a dust cloud or similar that allows for a wind velocity estimate. Certainly, if auxiliary wind information is available, this will be the better choice. In the next section, such emission rates are estimated using the lidar wind data as transport velocity.

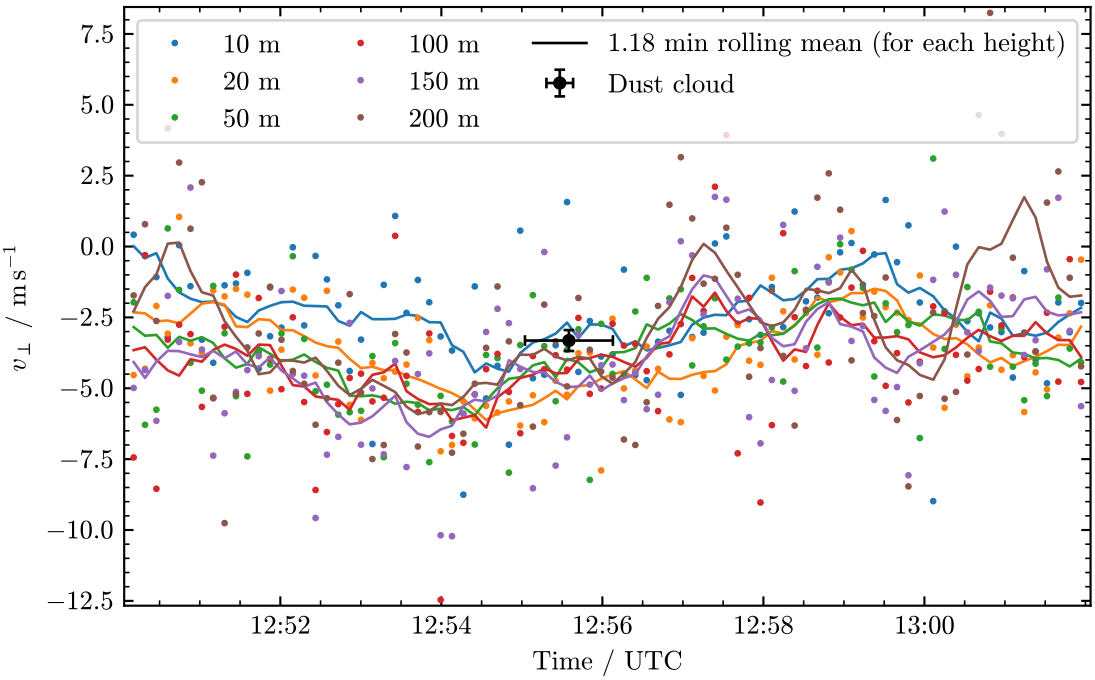

Fig. 6.9. The wind velocity perpendicular to the line of sight of the camera at different height levels on July 4, 2024. Dots are single measurement points by the lidar, which was stationed at the Pinto landfill facilities, and lines are rolling means over the time difference between two subsequent camera observations. The black point is the wind velocity extracted from the dust cloud moving in the two images in Fig. 6.8. The horizontal error bar extends from the time of the first observation of the dust cloud to the second. The vertical error bar was calculated using Eq. (6.3).

6.5 Quantification of Methane Emission Rates

Since in our viewing geometry, we do not see a well-defined methane plume above the landfill similar to the observations of, e.g., methane emissions from a coal mine ventilation shaft (cf. Knapp et al., 2023), an alternative approach for quantification is required. The method proposed here is a one-box model, which equates the landfill methane emission rate to the advective transport of the methane enhancement detected in the images.

6.5.1 Identification of Accumulated Methane

To apply such a one-box model, an automatic identification of enhanced methane concentrations in the images is useful. This process separates the high-enhancement pixels of methane at the ground from the noise elsewhere in the image. Additionally, it ensures that dust cloud areas are not included in the emission calculation, as their negative

enhancement would significantly lower the estimated emission rate. The identification algorithm leverages the fact that methane enhancement near the ground covers many contiguous pixels, while pixels randomly enhanced due to noise are surrounded by many pixels without such enhancement. The algorithm is detailed below:

1. Select all pixels which exhibit an enhancement greater than a threshold of $\alpha_\mathrm{t} = 1000\,\mathrm{ppm\,m}$.
2. From this selection, remove all pixels which have $N_\mathrm{neighbor} \geq 1$ neighboring pixels (straight or diagonal, 8 neighbors per pixel in total) which are not included in the selection.
3. Sort the contiguous patches of selected pixels by size, i.e., number of pixels in it.
4. From the selection, eliminate all patches that do not have an overlap in height with the largest patch, and all patches that contain less than $p_\mathrm{min} = 11$ pixels.
5. Dilate the selection with a circular mask of radius r, but do not include any ground pixels.

Except for single images captured during the morning of July 2, 2024, which show very little methane enhancement directly above the ground, this algorithm reliably selects all areas with a significant amount of methane close to the ground. The values of the variables α_t, N_neighbor, p_min, and r used in this algorithm are based on empirical testing, such that the algorithm's identification of pixels resembles an intuitive manual identification as closely as possible. The optimal values may also depend on the observed methane enhancement distribution. Like this, for July 2, 2024, a dilation radius of $r = 10$ pixels was used, and for July 4, 2024, $r = 5$ pixels, because on that day the camera was farther away from the landfill. In reality, the choice of the radius r is always a tradeoff between including areas which are still systematically enhanced even though quite some pixels fall below the threshold of α_t, and including pixels that belong to a dust cloud and exhibit strongly negative enhancements.

Figures 6.10 and 6.11 show examples of images where this identification algorithm was applied. In both, some dust cloud pixels are included, while some areas above the selection still look like they show a systematic enhancement, but overall, the prominent enhancement areas are well identified.

6.5.2 One-Box Model

Basically, the one-box model equates the landfill methane emission rate with the advective transport of methane in the image to the left or right. This approach assumes a steady state of methane emissions from the landfill. The methane slant column enhancements, identified by the algorithm outlined in the previous section, are integrated

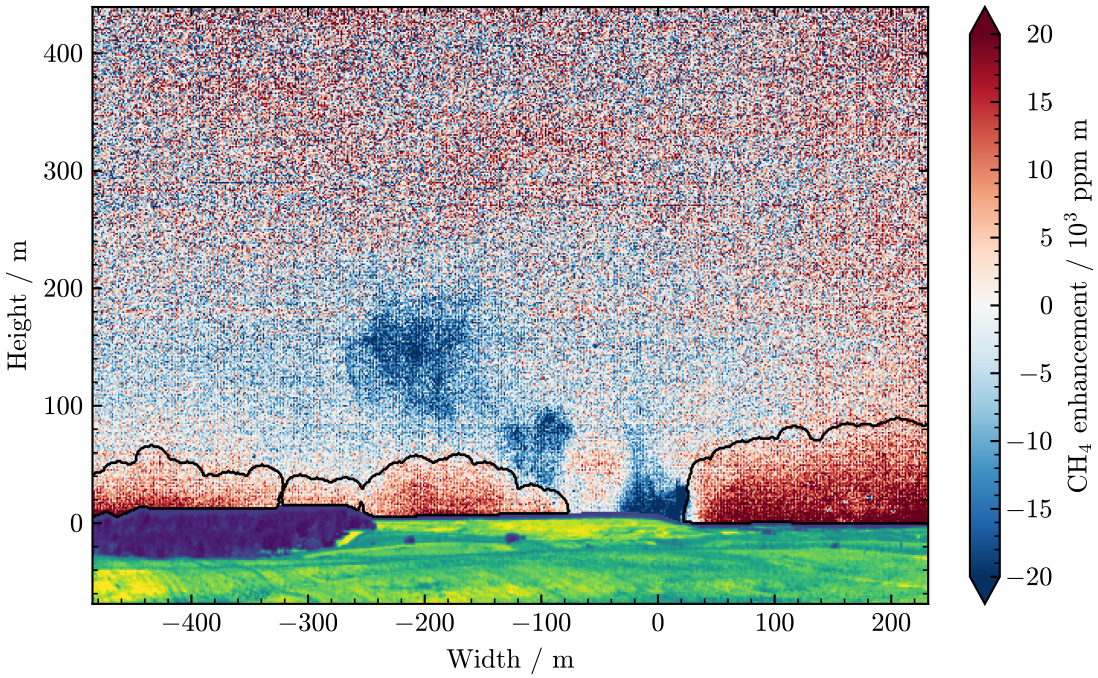

Fig. 6.10. Image from July 2, 2024, at 13:35 UTC. The methane enhancement identified algorithmically is enclosed in black.

vertically and averaged over all frames in an image. These values are then multiplied by a 10-min averaged wind velocity perpendicular to the camera's line of sight. This calculation yields an emission rate in dimensions of molecules per time or mass per time. Below are the details of the one-box model, followed by a discussion of its uncertainties and shortcomings.

Once the pixels of true methane enhancement are identified, the following procedure is applied to derive an emission rate:

1. Convert the slant column enhancements from ppm m to $\mathrm{kg\,m^{-2}}$ using Eq. (2.22). Here, the same pressure as for the generation of the UAS was used, and the temperature was estimated as the average of the time series from the temperature logger, excluding periods when the logger was exposed to direct sunlight.

2. Integrate the enhancements vertically: $\alpha_{f,\mathrm{int}} = \sum_{l=0}^{L-1} s_{lf} \cdot \alpha_{lf} \cdot h_l$, where L is the number of lines in the image, s_{lf} is 1 if the pixel at line l and frame f is among the selected pixels and 0 otherwise, and h_l is the height of line l in m. $\alpha_{f,\mathrm{int}}$ has units of $\mathrm{kg\,m^{-1}}$.

3. Average over all frames $f \in G$ where $G = \{f \,|\, \alpha_{f,\mathrm{int}} > 0\}$ is the set of all frames

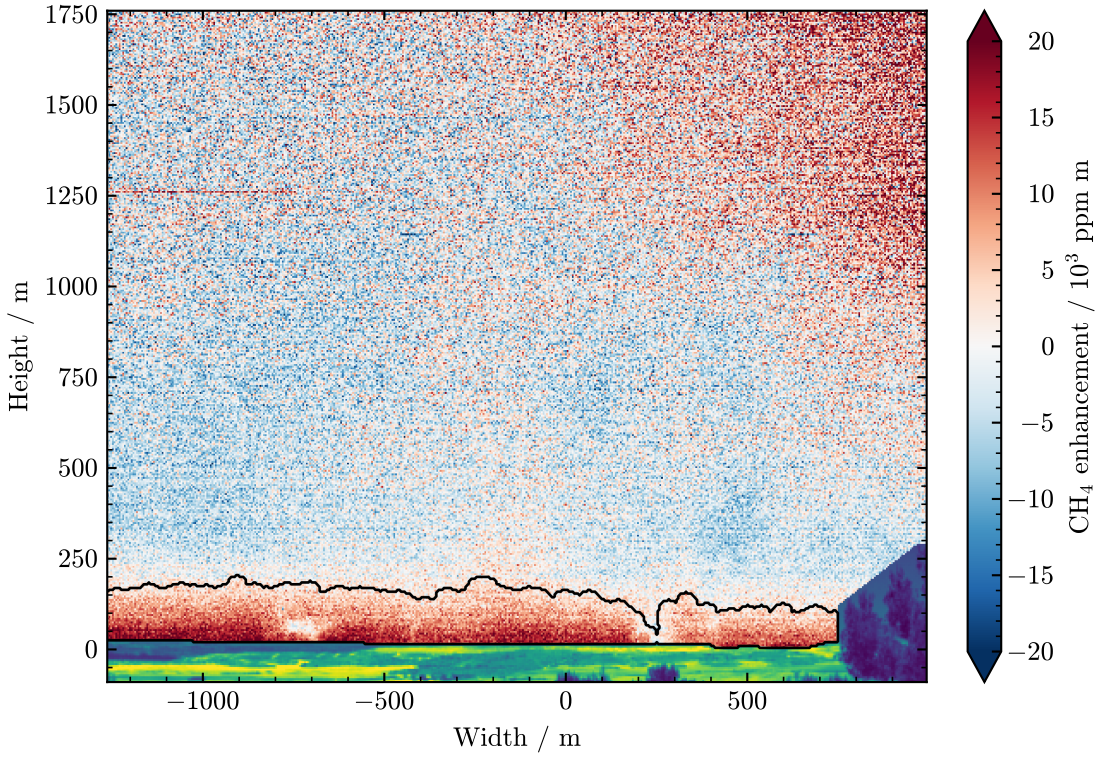

Fig. 6.11. Image from July 4, 2024, at 11:31 UTC. The methane enhancement identified algorithmically is enclosed in black.

with $\alpha_{f,\mathrm{int}} > 0$. This yields $\alpha_{\mathrm{int,avg}}$, which is still in units of $\mathrm{kg\,m^{-1}}$. Averaging in this manner assumes that all frames where $\alpha_{f,\mathrm{int}} \leq 0$ do not show enhanced methane concentrations either because they are obscured by dust clouds or because they are located upwind of the methane source. The latter is only the case on July 2, 2024, before 9:00 UTC for the data presented in this thesis (e.g., Fig. 6.4). In both cases, averaging like this ensures frames with $\alpha_{f,\mathrm{int}} \leq 0$ are excluded from the emission rate calculation.

4. Multiply with the wind velocity perpendicular to the line of sight $v_\perp$ averaged over $\pm 5\,\mathrm{min}$ around the time stamp of the image. Do this for all different height levels of the wind lidar data. This results in six time series of methane emission rates in units of $\mathrm{t\,h^{-1}}$.

5. For each emission rate and corresponding perpendicular wind velocity, calculate the Pearson correlation coefficient r.

6. Choose the wind height level that yields the smallest such correlation. A high

correlation means the variability in the emission rate time series stems from the variability in wind velocity, whereas a small correlation means the variability is true variability in emission. Therefore, the wind velocity from the wind height level with the smallest correlation is most representative of the real transport velocity of methane.

7. Take the absolute value of the emission rate to prevent unphysical negative emission rates, which can emerge if the wind changes direction. It is important to only take the absolute value after the correlation calculations are made, or the correlation is meaningless, as, e.g., a correlation coefficient of 0 may result if the correlation between emission rate and wind velocity is perfect, but the wind changes direction halfway through the time series.

Steps 2, 3, 4, and 7 can be summed up as

$$\alpha_{f,\mathrm{int}} = \sum_{l=0}^{L-1} s_{lf} \cdot \alpha_{lf} \cdot h_l \tag{6.4}$$

$$E = \frac{|v_\perp|}{|G|} \sum_{f \in G} \alpha_{f,\mathrm{int}}\,, \tag{6.5}$$

where $|G|$ is the cardinality of G, i.e., the number of frames in G, and E is the resulting emission rate.

The uncertainties of the different variables and data processing steps are discussed following the same numbering scheme as previously:

0. The methane enhancements that the matched filter returns are afflicted with uncertainty, and the methane identification algorithm also introduces uncertainty. The sum of these two is assumed to be 20% of the enhancement, which represents the current best estimate of this error. A future laboratory study, e.g., retrieving a know methane column in a cell, could be conducted to consolidate this uncertainty estimate.

1. The uncertainty of temperature and pressure needed for the conversion of enhancements from ppm m to $\mathrm{kg\,m^{-2}}$ are on the order of a few percent, and thus neglected.

2. The uncertainty Δh_l of the line heights h_l, which are needed for the vertical integration of enhancements, is directly proportional to the uncertainty of the distance from camera to enhanced methane concentrations. For July 2, 2024, this is estimated to be $\Delta h_l / h_l = 50\%$, and for July 4, 2024, $\Delta h_l / h_l = 30\%$. This uncertainty depends on the viewing geometry; the larger the distance between camera and landfill (where the enhanced methane concentrations are assumed to be), the lower the

relative uncertainty. Additionally, it depends on the viewing direction, as the Pinto landfill has an oblong shape extending from northeast to southwest. Since the uncertainty of the distance results in equal relative uncertainties for h_l across all lines l, we assume that all Δh_l are perfectly correlated (even though the distance and its uncertainty might slightly vary for different lines l).

3. The uncertainty of enhancements introduced by dust clouds is estimated to be 10%. With the initial enhancement uncertainty of 20%, this is roughly combined to a relative uncertainty of $\Delta\alpha_{lf}/\alpha_{lf} = 30\%$. For these uncertainties $\Delta\alpha_{lf}$, we also assume perfect correlation across all lines l and all frames f. This assumption is based on the premise that any over- or underestimation of enhancements by the matched filter is likely systematic.

4. The uncertainty of the wind velocity perpendicular to the line of sight is determined by calculating the standard deviation $\Delta v_\perp$ over the same 10-minute period used for averaging. This uncertainty of the wind velocity is the primary contributor to the overall uncertainty in the emission rate.

The resulting uncertainty of the emission rate E is estimated using Gaussian propagation of uncertainty. Due to the correlation between all $\Delta\alpha_{lf}$ and all Δh_l, these uncertainties are summed linearly. These sums are then squared before adding the squared wind uncertainty $\Delta v_\perp^2$. The resulting squared uncertainty of the emission rate E is then

$$(\Delta E)^2 = \left(\frac{\partial E}{\partial v_\perp}\right)^2 (\Delta v_\perp)^2 + \left(\sum_{l=0}^{L-1} \frac{\partial E}{\partial h_l}\Delta h_l\right)^2 + \left(\sum_{f\in G}\sum_{l=0}^{L-1} \frac{\partial E}{\partial \alpha_{lf}}\Delta\alpha_{lf}\right)^2 \tag{6.6}$$

$$= \frac{E^2}{v_\perp^2}(\Delta v_\perp)^2 + \frac{v_\perp^2}{|G|^2}\left(\left(\sum_{f\in G}\sum_{l=0}^{L-1} s_{lf}\alpha_{lf}\Delta h_l\right)^2 + \left(\sum_{f\in G}\sum_{l=0}^{L-1} s_{lf}h_l\Delta\alpha_{lf}\right)^2\right). \tag{6.7}$$

This simplistic one-box model has additional shortcomings which cannot be directly quantified, and which are discussed in the following.

The model's most significant issue is likely the unstable wind conditions. Since methane accumulates just above the ground, the wind that transports it is slow and frequently changes direction. When the wind direction shifts, e.g., from blowing right to blowing left, the same methane molecules contribute to the emission rate twice: once when moving to the right and again when transported back to the left. The only alternative to this would be not to take the absolute value of the emission rate. However, this would allow for unphysical negative emission rates, which could and would occur over extended periods.

Furthermore, the model only considers methane transport to the left or right, neglecting movement toward or away from the observer, as well as upward motion. When

methane is transported along the observer's line of sight, it remains within the FOV, but turbulent diffusion reduces its concentration, possibly making detection by the matched filter more difficult, and also changing its distance to the observer, which is needed for the emission rate estimate. Similarly, while upward methane movement is still captured in the image, the dilution caused by turbulence appears as a vertical gradient in the images, and upward motion of methane is not captured in the model.

Instead of using wind data from a single height level, another approach would be to interpolate all wind height levels to create a vertical wind profile, which could then be used as height-dependent methane transport velocity in the one-box model. However, this approach was not implemented for several reasons. First, the emission rates inherently come with significant uncertainty. Using all wind heights separately for different emission rate estimates provides a clearer understanding of the spread, uncertainty, and wind velocity dependence of the emission rates. Second, the exact position of an enhanced methane concentration along the line of sight is unknown, making it difficult to determine its precise height above ground and thus unclear which wind height level is most appropriate. Topographical features also greatly affect wind patterns, further complicating the determination of an accurate wind height. Lastly, creating a wind profile by interpolating all wind height levels significantly increases the model's complexity without reducing the uncertainty in emission rate estimates. Therefore, focusing on a single wind height level that minimizes the correlation between wind velocity perpendicular to the line of sight and emission rate is a more practical and reliable approach for estimating methane emissions from the landfill.

6.5.3 Emission Rate Time Series

Figure 6.12 shows an emission rate time series from July 2, 2024, which was obtained by the algorithm lined out above. It furthermore shows the wind velocity perpendicular to the line of sight at a height of 50 m, which was averaged over 10 min. This wind height level yielded the smallest Pearson correlation coefficient between wind velocity and emission rate, which was $r_{50\,\mathrm{m}} = 0.90$. The figure also shows the methane mass in the image, which was obtained by integrating the enhancements of all selected pixels vertically and horizontally.

Figure 6.13 shows the same for July 4, 2024, with a wind height of 10 m, which yielded the lowest correlation of $r_{10\,\mathrm{m}} = 0.90$ for that time series. For comparison, Fig. 6.14 shows an emission rate time series for a wind height of 150 m, which has a correlation of $r_{150\,\mathrm{m}} = 0.93$. Tab. 6.1 shows the average emission rates and Pearson correlation coefficients for all wind height levels on both July 2 and July 4, 2024.

While the uncertainty of the emission rates is very big, and the temporal fluctuations are very strong, the emission rates are of the same order of magnitude as listed in the PRTR-España ($0.66\,\mathrm{t\,h^{-1}}$ in 2023, Ministry for the Ecological Transition and the Demographic Challenge (MITECO), 2025), in the TNO GHGco v5 dataset ($1.28\,\mathrm{t\,h^{-1}}$ in 2018,

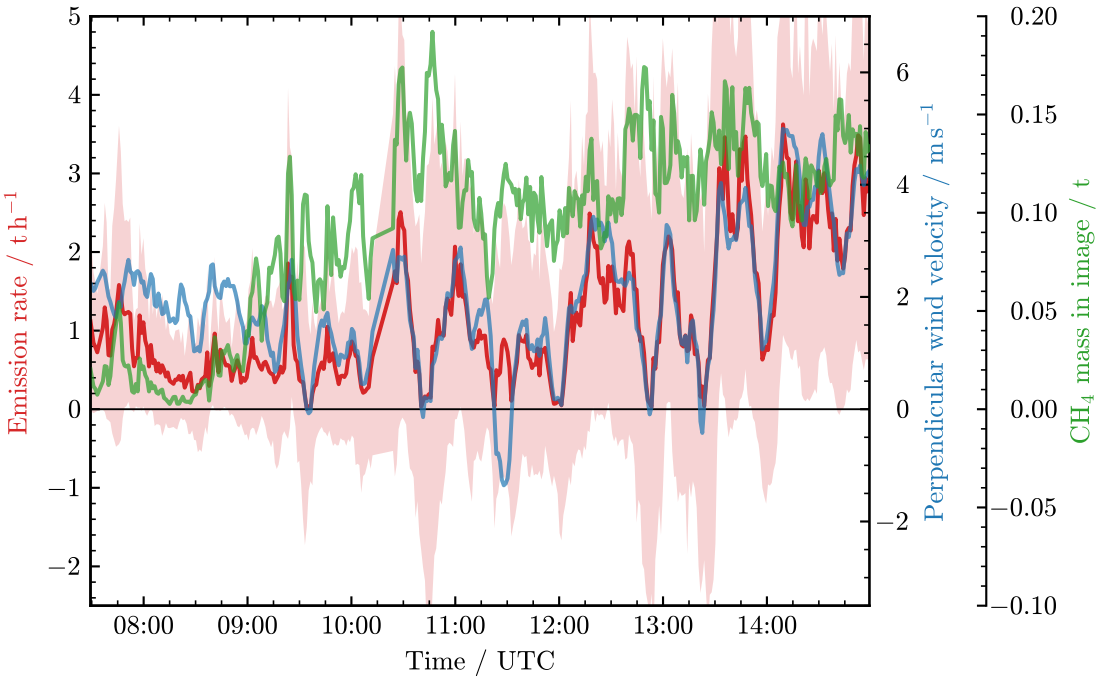

Fig. 6.12. Emission rate on July 2, 2024, in red, and uncertainty as light red shaded area. 10 min-averaged wind velocity perpendicular to the line of sight from the wind lidar at a height of 50 m in blue. Total methane mass in each image in green. The data gap at around 10:15 UTC is due to technical problems with the camera.

TNO preliminary data, Hugo Denier van der Gon, personal communication, 2025), and as found by Tu et al. (2022) ($(7.1 \pm 0.6)\,\mathrm{t\,h^{-1}}$ for the landfills Pinto, Valdemingómez, and Alcalá together between 2018 and 2020) and Krautwurst et al. (2024) ($\sim 5\,\mathrm{t\,h^{-1}}$ in 2022). As already mentioned in Chapter 1, a comparison between our measurements and these numbers from other sources is difficult as the active part of the landfill changed in February 2024 (Personnel of the Pinto landfill, personal communication, June 27, 2024). Furthermore, the difference between the emission rates on July 2 and July 4, 2024, also indicates a large uncertainty.

The high correlation of emission rate and perpendicular wind velocity is clearly visible in all three figures. The correlation of emission rate and methane mass in the images is only weak, but can be seen at certain points in time, e.g., at ∼7:45 UTC on July 2, 2024, in Fig. 6.12.

Ideally, we would expect the total methane mass per image to increase whenever the perpendicular wind speed decreases and vice versa, because decreasing wind speed means less advective transport of methane, which should result in a methane accumulation. This behavior would suppress the short-term variations that we see in all emission time series,

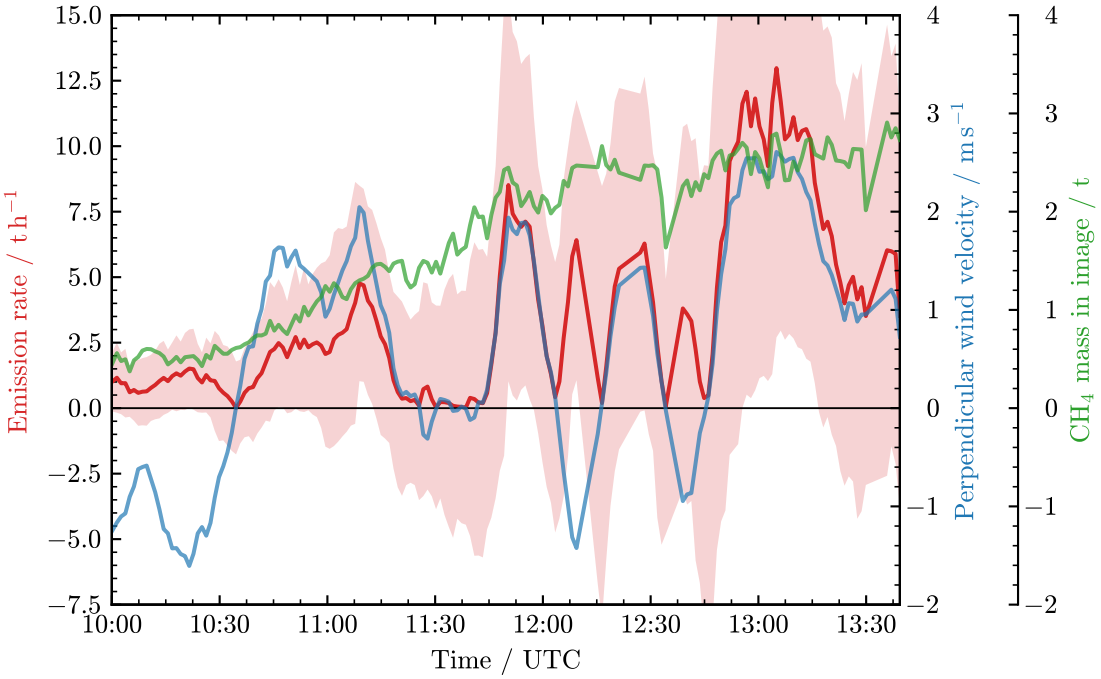

Fig. 6.13. Emission rate on July 4, 2024, in red, and uncertainty as light red shaded area. 10 min-averaged wind velocity perpendicular to the line of sight from the wind lidar at a height of 10 m in blue. Total methane mass in each image in green.

Tab. 6.1. Average emission rate and Pearson correlation coefficient between emission rate and wind velocity perpendicular to the line of sight for the different wind heights on both July 2 and July 4, 2024

Date	Wind height / m	Pearson correlation	Average emission rate / t h^{-1}
July 2, 2024	10	0.95	0.49
	20	0.92	0.85
	50	0.90	1.16
	100	0.91	1.21
	150	0.94	1.35
	200	0.94	1.46
July 4, 2024	10	0.90	3.55
	20	0.92	4.70
	50	0.93	5.22
	100	0.94	5.62
	150	0.93	5.78
	200	0.93	5.95

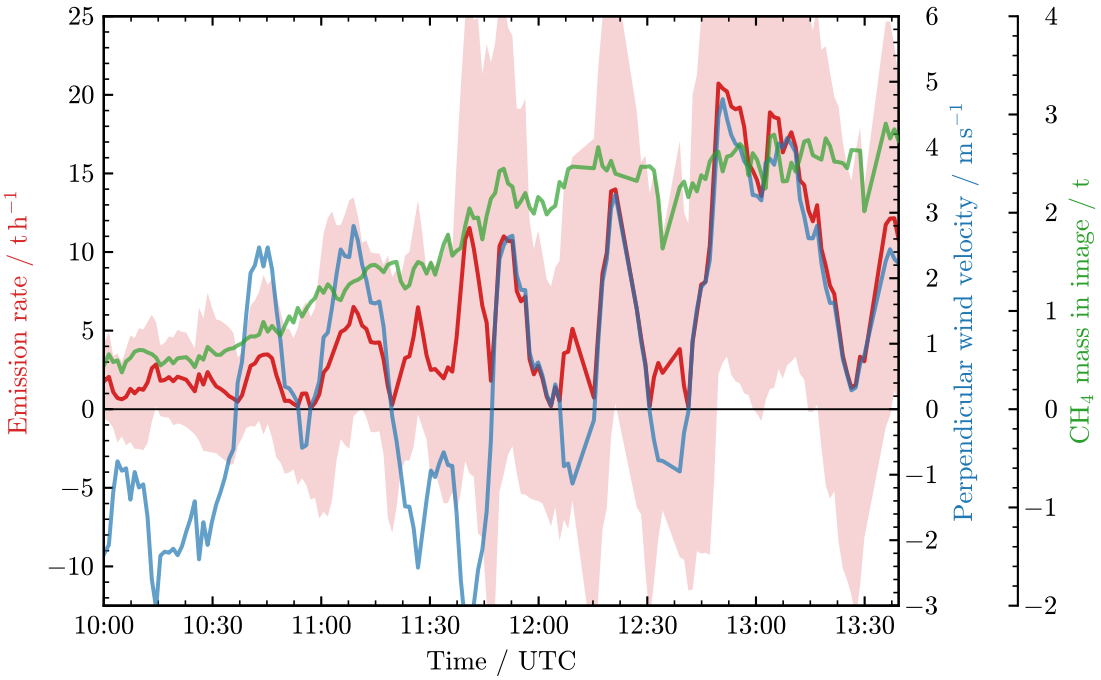

Fig. 6.14. Emission rate on July 4, 2024, in red, and uncertainty as light red shaded area. 10 min-averaged wind velocity perpendicular to the line of sight from the wind lidar at a height of 150 m in blue. Total methane mass in each image in green.

and it would reduce or remove the correlation between emission rate and wind velocity. The fact that we do not observe this behavior indicates inaccurate model assumptions, e.g., significant vertical transport and turbulent dilution of methane.

The strong correlation between emission rate and perpendicular wind velocity furthermore indicates that the short-term emission rate variability is not a real variability of landfill methane emissions. The emission rate slowly increasing over time, though, could be a real signal, not least because this increase is present on both days analyzed, independent of the observation position. Both times, this emission rate increase is due to the increasing amount of methane in the image, which was already discussed in Section 6.3.

7 Conclusion and Outlook

7.1 Conclusion

This thesis evaluates the capabilities of ground-based spectral imaging for detecting and quantifying methane emissions from a landfill. Data was collected at the Pinto landfill near Madrid, Spain, over two weeks in the summer of 2024 (Chapter 5). The hyperspectral camera HySpex SWIR-384 allows for a scanning rate on the order of a minute, and a wind lidar was co-deployed to record wind velocities at various altitudes. On July 2 and July 4, 2024, weather conditions were best, which is why those two days were selected to be evaluated for this thesis. The hyperspectral images were analyzed using the lognormal matched filter (LMF), which was found to outperform the classic matched filter (CMF) and its variants. As the retrieved images show a diffuse distribution of enhanced methane concentrations above the landfill, a one-box model was employed to estimate emission rates using the wind data from the lidar.

To compare different matched filters, enhancements were retrieved from an image of sky-scattered sunlight with artificially imprinted methane absorption signatures in 2% of its pixels. The results reveal that the CMF and its variant, the reweighted $\ell 1$ matched filter (RWL1MF), exhibit an albedo bias, necessitating an albedo correction. In contrast, the LMF and its iterative version were found not to require such a correction. Furthermore, real data from a coal mine ventilation shaft in the Upper Silesian Coal Basin (USCB), Poland, showed that, while all matched filters retrieve similar enhancements, there are systematic differences. The CMF retrieves the smallest enhancements, while the iterative lognormal matched filter (ILMF) retrieves the largest enhancements. The RWL1MF and LMF yield similar enhancements that fall between these extremes (Section 4.7). Given that the exceptionally high enhancements from the ILMF are likely due to skewed background statistics, the LMF was selected for retrieving all enhancement data presented in this thesis. It was preferred over the RWL1MF due to its more reasonable physical background assumptions, its lower computational demands, and its inherent simplicity.

Retrieved images of the Pinto landfill show that enhanced methane concentrations are spread across a broad area above the landfill. These enhanced concentrations are mainly observed near the ground, with a vertical gradient of decreasing concentrations with increasing altitude. During the course of a day, the observed concentrations of methane increase (Section 6.3). Dust clouds obstruct enhanced methane concentrations and appear as very negative enhancement due to a shortened light path, but they do not significantly

impact the retrieval of methane columns in other parts of an image (Section 6.2). By analyzing images of moving dust clouds present in two or more consecutive images, it was demonstrated that one can infer the wind velocity perpendicular to the line of sight. An example calculation of this yielded a wind velocity consistent with measurements taken with the wind lidar (Section 6.4).

Using the wind lidar data as a proxy for methane transport velocity, emission rates can be inferred from the images of methane enhancements. For this, an automated selection of areas of enhanced methane concentrations was implemented, ensuring that regions affected by dust clouds are excluded (Section 6.5.1). The emission rates derived through this one-box model (Section 6.5.2) show a high correlation with wind velocity, indicating weaknesses of the model. This correlation suggests that short-term variability in emission rates is due to wind variability rather than changes in source emissions. Furthermore, the emission rates exhibit considerable uncertainty. Still, the temporally averaged emission rates on the order of $1\,\mathrm{t\,h^{-1}}$ to $5\,\mathrm{t\,h^{-1}}$ are of the same order of magnitude as the emission rates listed in emission registers such as the Spanish Register of Emissions and Pollutant Sources (PRTR-España) and the TNO GHGco v5 dataset, and as recently found in other studies (Krautwurst et al., 2024; Tu et al., 2022). Additionally, the observed increase in emission rates from morning to afternoon might be true landfill emission rate changes linked to a diurnal cycle, as suggested by Delkash et al. (2022) (Section 6.5.3).

Overall, the findings demonstrate the potential of ground-based spectral imaging for monitoring and quantifying methane emissions of the Pinto landfill, which was specifically chosen for this proof of concept due to its very high methane emission rate. Methane enhancements are clearly visible in the resulting images, and emission rates can be inferred from the collected data. However, these emission rates come with a high degree of uncertainty. Our measurement technique is well-suited to resolve temporal variations of methane concentrations, and remote sensing allows measurements without needing physical access to the landfill premises. Other techniques, such as in-situ measurements, however, are not restricted to daytime and good weather conditions and are not affected by aerosols. Given the diffuse shape of enhanced methane concentrations, alternative remote sensing viewing geometries, such as airborne or satellite measurements, can potentially observe the full plume, where the ground-based geometry has its limits. Complementary measurements using other instruments and techniques, such as in-situ measurements, also have the potential to quantify landfill methane emission rates accurately.

7.2 Outlook

A lot of data from the measurement campaign has not been analyzed yet. Although the data presented in this thesis was collected on days with optimal weather conditions, data from other days may still reveal interesting features or support the trends observed so

far, such as the increasing emission rates over the course of a day.

Furthermore, data from the HySpex Mjolnir S-620 camera, which was also deployed during the campaign, remains unanalyzed. Given that this camera has different optical properties compared to the HySpex SWIR-384, it could be insightful to compare the methane enhancements retrieved from both cameras' spectra. Such a comparison could provide valuable insights into the effects of varying camera characteristics on the retrieved enhancements.

Data collected at the Valdemingómez landfill in Madrid, Spain, also has not yet been analyzed. Likewise, it would be interesting to see if these observations show the same trends as found at the Pinto landfill and whether they yield emission rates similar to those found in previous studies.

Additionally, conducting camera observations of a controlled release experiment would be valuable for validating the methane column enhancements retrieved by a matched filter[1]. This could also be used to compare the different matched filters and help implement improvements. For the ILMF, this could be a more sophisticated selection of enhanced pixels or areas to be excluded from the calculation of mean spectrum and covariance.

During and around the time of the campaign, observations of the Pinto and Valdemingómez landfills were also conducted by GHGSat satellites, by the EnMAP satellite, and by TROPOMI onboard the Sentinel-5 Precursor satellite, as well as from an aircraft. Comparing these data with the HySpex measurements might provide valuable insights into the accuracy of methane column enhancements and emission rates inferred from the HySpex data. This comparison could be particularly interesting because previous measurements at the Pinto landfill were conducted while Phase III was still operational. The Phase III area was sealed and equipped with a degassing system in February 2024 (Personnel of the Pinto landfill, personal communication, June 27, 2024), which means that our measurements and previous studies need to be compared with caution. Ideally, measurements with the same instrument are performed before and after such emission reduction measures are taken so their effectiveness can be assessed using the collected data.

[1]This was initially planned for 2024 but was not carried out due to practical constraints.

Bibliography

Anderson, G. P., Clough, S. A., Kneizys, F. X., Chetwynd, J. H., & Shettle, E. P. (1986). *AFGL atmospheric constituent profiles (0–120 km)* (tech. rep. No. AFGL-TR-86-0110). Air Force Geophysics Lab., Hanscom AFB, MA. https://apps.dtic.mil/sti/pdfs/ADA175173.pdf

Anderson, K. S., Hansen, C. W., Holmgren, W. F., Jensen, A. R., Mikofski, M. A., & Driesse, A. (2023). pvlib python: 2023 project update. *Journal of Open Source Software*, *8*(92), 5994. https://doi.org/10.21105/joss.05994

Ångström, A. (1929). On the atmospheric transmission of sun radiation and on dust in the air. *Geografiska Annaler*, *11*, 156–166. https://doi.org/10.2307/519399

Baumgartner, A. (2022). *Traceable imaging spectrometer calibration and transformation of geometric and spectral pixel properties* [Doctoral dissertation]. Universität Osnabrück. https://doi.org/10.48693/38

Berk, A., Conforti, P., Kennett, R., Perkins, T., Hawes, F., & Bosch, J. v. d. (2014). MODTRAN6: A major upgrade of the MODTRAN radiative transfer code. *Algorithms and Technologies for Multispectral, Hyperspectral, and Ultraspectral Imagery XX*, *9088*, 113–119. https://doi.org/10.1117/12.2050433

Butz, A., Guerlet, S., Hasekamp, O., Schepers, D., Galli, A., Aben, I., Frankenberg, C., Hartmann, J.-M., Tran, H., Kuze, A., Keppel-Aleks, G., Toon, G., Wunch, D., Wennberg, P., Deutscher, N., Griffith, D., Macatangay, R., Messerschmidt, J., Notholt, J., & Warneke, T. (2011). Toward accurate CO2 and CH4 observations from GOSAT. *Geophysical Research Letters*, *38*(14). https://doi.org/10.1029/2011GL047888

Butz, A., Hasekamp, O. P., Frankenberg, C., Vidot, J., & Aben, I. (2010). CH4 retrievals from space-based solar backscatter measurements: Performance evaluation against simulated aerosol and cirrus loaded scenes. *Journal of Geophysical Research: Atmospheres*, *115*. https://doi.org/10.1029/2010JD014514

Copernicus Climate Change Service. (2025, January 10). *Copernicus: 2024 is the first year to exceed 1.5°C above pre-industrial level*. Retrieved April 7, 2025, from https://climate.copernicus.eu/copernicus-2024-first-year-exceed-15degc-above-pre-industrial-level

Deering, C. A., & Stoker, J. M. (2014). Let's agree on the casing of lidar. *LiDAR News Magazine*, *4*(6). Retrieved February 28, 2025, from https://lidarmag.com/2014/09/05/lets-agree-on-the-casing-of-lidar/

Delkash, M., Chow, F. K., & Imhoff, P. T. (2022). Diurnal landfill methane flux patterns across different seasons at a landfill in southeastern US. *Waste Management*, *144*, 76–86. https://doi.org/10.1016/j.wasman.2022.03.004

Demtröder, W. (2018). *Atoms, molecules and photons: An introduction to atomic-, molecular- and quantum physics*. Springer. https://doi.org/10.1007/978-3-662-55523-1

Demtröder, W. (2019). *Electrodynamics and optics*. Springer International Publishing. https://doi.org/10.1007/978-3-030-02291-4

Denman, K. L., Brasseur, G., Chidthaisong, A., Ciais, P., Cox, P. M., Dickinson, R. E., Hauglustaine, D., Heinze, C., Holland, E., Jacob, D., Lohmann, U., Ramachandran, S., da Silva Dias, P. L., Wofsy, S. C., & Zhang, X. (2007). Couplings between changes in the climate system and biogeochemistry. In S. Solomon, D. Qin, M. Manning, Z. Chen, M. Marquis, K. B. Averyt, M. Tignor, & H. L. Miller (Eds.), *Climate change 2007: The physical science basis. Contribution of working group I to the Fourth Assessment Report of the Intergovernmental Panel on Climate Change* (pp. 499–587). Cambridge University Press. https://www.ipcc.ch/site/assets/uploads/2018/02/ar4-wg1-chapter7-1.pdf

Etminan, M., Myhre, G., Highwood, E. J., & Shine, K. P. (2016). Radiative forcing of carbon dioxide, methane, and nitrous oxide: A significant revision of the methane radiative forcing. *Geophysical Research Letters*, *43*(24), 12, 614–12, 623. https://doi.org/10.1002/2016GL071930

Foote, M. D., Dennison, P. E., Sullivan, P. R., O'Neill, K. B., Thorpe, A. K., Thompson, D. R., Cusworth, D. H., Duren, R., & Joshi, S. C. (2021). Impact of scene-specific enhancement spectra on matched filter greenhouse gas retrievals from imaging spectroscopy. *Remote Sensing of Environment*, *264*, 112574. https://doi.org/10.1016/j.rse.2021.112574

Foote, M. D., Dennison, P. E., Thorpe, A. K., Thompson, D. R., Jongaramrungruang, S., Frankenberg, C., & Joshi, S. C. (2020). Fast and accurate retrieval of methane concentration from imaging spectrometer data using sparsity prior. *IEEE Transactions on Geoscience and Remote Sensing*, *58*(9), 6480–6492. https://doi.org/10.1109/TGRS.2020.2976888

Gordon, I. E., Rothman, L. S., Hargreaves, R. J., Hashemi, R., Karlovets, E. V., Skinner, F. M., Conway, E. K., Hill, C., Kochanov, R. V., Tan, Y., Wcisło, P., Finenko, A. A., Nelson, K., Bernath, P. F., Birk, M., Boudon, V., Campargue, A., Chance, K. V., Coustenis, A., … Yurchenko, S. N. (2022). The HITRAN2020 molecular spectroscopic database. *Journal of Quantitative Spectroscopy and Radiative Transfer*, *277*, 107949. https://doi.org/10.1016/j.jqsrt.2021.107949

Gulev, S. K., Thorne, P. W., Ahn, J., Dentener, F. J., Domingues, C. M., Gerland, S., Gong, D., Kaufman, D. S., Nnamchi, H. C., Quaas, J., Rivera, J. A., Sathyendranath, S., Smith, S. L., Trewin, B., von Schuckmann, K., & Vose, R. S. (2021). Changing state of the climate system. In V. Masson-Delmotte, P. Zhai, A. Pirani,

S. L. Connors, C. Péan, S. Berger, N. Caud, Y. Chen, L. Goldfarb, M. I. Gomis, M. Huang, K. Leitzell, E. Lonnoy, J. B. R. Matthews, T. K. Maycock, T. Waterfield, O. Yelekçi, R. Yu, & B. Zhou (Eds.), *Climate change 2021: The physical science basis. Contribution of working group I to the Sixth Assessment Report of the Intergovernmental Panel on Climate Change* (pp. 287–422). Cambridge University Press. https://doi.org/10.1017/9781009157896.004

Haveresch, H. (2023). *Ground-based hyperspectral imaging of greenhouse gases using a physics inversion algorithm* [Unpublished master's thesis]. Heidelberg University.

Holben, B. N., Eck, T. F., Slutsker, I., Tanré, D., Buis, J. P., Setzer, A., Vermote, E., Reagan, J. A., Kaufman, Y. J., Nakajima, T., Lavenu, F., Jankowiak, I., & Smirnov, A. (1998). AERONET—a federated instrument network and data archive for aerosol characterization. *Remote Sensing of Environment*, *66*(1), 1–16. https://doi.org/10.1016/S0034-4257(98)00031-5

Huang, D., Du, Y., Xu, Q., & Ko, J. H. (2022). Quantification and control of gaseous emissions from solid waste landfill surfaces. *Journal of Environmental Management*, *302*, 114001. https://doi.org/10.1016/j.jenvman.2021.114001

IPCC. (2021). Summary for policymakers. In V. Masson-Delmotte, P. Zhai, A. Pirani, S. Connors, C. Péan, S. Berger, N. Caud, Y. Chen, L. Goldfarb, M. Gomis, M. Huang, K. Leitzell, E. Lonnoy, J. Matthews, T. Maycock, T. Waterfield, O. Yelekçi, R. Yu, & B. Zhou (Eds.), *Climate change 2021: The physical science basis. Contribution of working group I to the Sixth Assessment Report of the Intergovernmental Panel on Climate Change* (pp. 3–32). Cambridge University Press. https://doi.org/10.1017/9781009157896.001

Kasten, F., & Young, A. T. (1989). Revised optical air mass tables and approximation formula. *Applied Optics*, *28*(22), 4735–4738. https://doi.org/10.1364/AO.28.004735

Kefala, K., Boudon, V., Yurchenko, S. N., & Tennyson, J. (2024). Empirical rovibrational energy levels for methane. *Journal of Quantitative Spectroscopy and Radiative Transfer*, *316*, 108897. https://doi.org/10.1016/j.jqsrt.2024.108897

Knapp, M., Scheidweiler, L., Külheim, F., Kleinschek, R., Necki, J., Jagoda, P., & Butz, A. (2023). Spectrometric imaging of sub-hourly methane emission dynamics from coal mine ventilation. *Environmental Research Letters*, *18*(4), 044030. https://doi.org/10.1088/1748-9326/acc346

Knapp, M. (2024). *Ground-based imaging of carbon dioxide and methane emission plumes* [Doctoral dissertation]. Heidelberg University. https://doi.org/10.11588/heidok.00034911

Kochanov, R. V., Gordon, I. E., Rothman, L. S., Wcisło, P., Hill, C., & Wilzewski, J. S. (2016). HITRAN application programming interface (HAPI): A comprehensive approach to working with spectroscopic data. *Journal of Quantitative Spectroscopy and Radiative Transfer*, *177*, 15–30. https://doi.org/10.1016/j.jqsrt.2016.03.005

Krautwurst, S., Fruck, C., Wolff, S., Borchardt, J., Huhs, O., Gerilowski, K., Gałkowski, M., Kiemle, C., Quatrevalet, M., Wirth, M., Mallaun, C., Burrows, J. P., Gerbig, C., Fix, A., Bösch, H., & Bovensmann, H. (2024). Identification and quantification of CH_4 emissions from madrid landfills using airborne imaging spectrometry and greenhouse gas lidar. *EGUsphere*, 1–52. https://doi.org/10.5194/egusphere-2024-3182

Lan, X., Tans, P., & Thoning, K. W. (2024a). *Trends in globally-averaged CO2 determined from NOAA Global Monitoring Laboratory measurements* (2024-12). https://doi.org/10.15138/9N0H-ZH07

Lan, X., Thoning, K. W., & Dlugokencky, E. J. (2024b). *Trends in globally-averaged CH4, N2O, and SF6 determined from NOAA Global Monitoring Laboratory measurements* (2024-12). https://doi.org/10.15138/P8XG-AA10

Lovett, R. J., & Parsons, M. L. (1977). Converting atomic spectral line widths from frequency to wavelength. *Journal of Chemical Education*, *54*(10), 615. https://doi.org/10.1021/ed054p615

Maasakkers, J. D., Varon, D. J., Elfarsdóttir, A., McKeever, J., Jervis, D., Mahapatra, G., Pandey, S., Lorente, A., Borsdorff, T., Foorthuis, L. R., Schuit, B. J., Tol, P., van Kempen, T. A., van Hees, R., & Aben, I. (2022). Using satellites to uncover large methane emissions from landfills. *Science Advances*, *8*(32), eabn9683. https://doi.org/10.1126/sciadv.abn9683

Manolakis, D., Truslow, E., Pieper, M., Cooley, T., & Brueggeman, M. (2014). Detection algorithms in hyperspectral imaging systems: An overview of practical algorithms. *IEEE Signal Processing Magazine*, *31*(1), 24–33. https://doi.org/10.1109/MSP.2013.2278915

METEK Meteorologische Messtechnik GmbH. (2023). *WindRanger 100/200 operation manual VS. 05 20230309*.

Ministry for the Ecological Transition and the Demographic Challenge (MITECO). (2025). *Spanish register of emissions and pollutant sources (PRTR-España)*. Retrieved April 4, 2025, from https://en.prtr-es.es

Mønster, J., Kjeldsen, P., & Scheutz, C. (2019). Methodologies for measuring fugitive methane emissions from landfills – a review. *Waste Management*, *87*, 835–859. https://doi.org/10.1016/j.wasman.2018.12.047

Norsk Elektro Optikk AS. (n.d.). *HySpex SWIR-384*. Retrieved February 27, 2025, from https://www.hyspex.com/media/z4jdbwah/hyspex_swir-384.pdf

Norsk Elektro Optikk AS. (2014). *HySpex imaging spectrometer user manual v4.1*.

Norsk Elektro Optikk AS. (2021). *HySpex SWIR-384 SN-3160 hyperspectral camera test report*.

Paris agreement [Treaty No. XXVII-7-d]. (2015, December 12). *United Nations*. Retrieved April 7, 2025, from https://treaties.un.org/pages/ViewDetails.aspx?src=TREATY&mtdsg_no=XXVII-7-d&chapter=27&clang=_en

Pei, Z., Han, G., Mao, H., Chen, C., Shi, T., Yang, K., Ma, X., & Gong, W. (2023). Improving quantification of methane point source emissions from imaging spectroscopy. *Remote Sensing of Environment*, *295*, 113652. https://doi.org/10.1016/j.rse.2023.113652

Petty, G. (2006). *A first course in atmospheric radiation*. Sundog Pub.

Prather, M. J., Holmes, C. D., & Hsu, J. (2012). Reactive greenhouse gas scenarios: Systematic exploration of uncertainties and the role of atmospheric chemistry. *Geophysical Research Letters*, *39*(9). https://doi.org/10.1029/2012GL051440

Roger, J., Guanter, L., Gorroño, J., & Irakulis-Loitxate, I. (2024a). Exploiting the entire near-infrared spectral range to improve the detection of methane plumes with high-resolution imaging spectrometers. *Atmospheric Measurement Techniques*, *17*(4), 1333–1346. https://doi.org/10.5194/amt-17-1333-2024

Roger, J., Irakulis-Loitxate, I., Valverde, A., Gorroño, J., Chabrillat, S., Brell, M., & Guanter, L. (2024b). High-resolution methane mapping with the EnMAP satellite imaging spectroscopy mission. *IEEE Transactions on Geoscience and Remote Sensing*, *62*, 1–12. https://doi.org/10.1109/TGRS.2024.3352403

Saunois, M., Martinez, A., Poulter, B., Zhang, Z., Raymond, P., Regnier, P., Canadell, J. G., Jackson, R. B., Patra, P. K., Bousquet, P., Ciais, P., Dlugokencky, E. J., Lan, X., Allen, G. H., Bastviken, D., Beerling, D. J., Belikov, D. A., Blake, D. R., Castaldi, S., … Zhuang, Q. (2024). Global methane budget 2000–2020. *Earth System Science Data Discussions*, 1–147. https://doi.org/10.5194/essd-2024-115

Schaum, A. (2021). A uniformly most powerful detector of gas plumes against a cluttered background. *Remote Sensing of Environment*, *260*, 112443. https://doi.org/10.1016/j.rse.2021.112443

Shaw, G. A., & Burke, H.-h. K. (2003). Spectral imaging for remote sensing. *Lincoln Laboratory Journal*, *14*(1), 3–28. https://archive.ll.mit.edu/publications/journal/journalarchives14-1.html

Shindell, D., Kuylenstierna, J. C. I., Vignati, E., van Dingenen, R., Amann, M., Klimont, Z., Anenberg, S. C., Muller, N., Janssens-Maenhout, G., Raes, F., Schwartz, J., Faluvegi, G., Pozzoli, L., Kupiainen, K., Höglund-Isaksson, L., Emberson, L., Streets, D., Ramanathan, V., Hicks, K., … Fowler, D. (2012). Simultaneously mitigating near-term climate change and improving human health and food security. *Science*, *335*(6065), 183–189. https://doi.org/10.1126/science.1210026

Siegel, T.-A. (2023). *Matched filter sensitivity studies for spectral greenhouse gas imagery* [Unpublished bachelor's thesis]. Heidelberg University.

Sindram, M. (2021). *Qualifizierung und Charakterisierung eines Lagesensors für stationäre Hyperspektralkameras [Qualification and characterization of a level sensor for stationary hyperspectral cameras]* [Unpublished bachelor's thesis]. Heidelberg University.

Smith, C., Nicholls, Z. R. J., Armour, K., Collins, W., Forster, P., Meinshausen, M., Palmer, M. D., & Watanabe, M. (2021). The earth's energy budget, climate feed-

backs, and climate sensitivity supplementary material. In V. Masson-Delmotte, P. Zhai, A. Pirani, S. L. Connors, C. Péan, S. Berger, N. Caud, Y. Chen, L. Goldfarb, M. I. Gomis, M. Huang, K. Leitzell, E. Lonnoy, J. B. R. Matthews, T. K. Maycock, T. Waterfield, O. Yelekçi, R. Yu, & B. Zhou (Eds.), *Climate change 2021: The physical science basis. Contribution of working group I to the Sixth Assessment Report of the Intergovernmental Panel on Climate Change*. https://www.ipcc.ch/report/ar6/wg1/downloads/report/IPCC_AR6_WGI_Chapter07_SM.pdf

Solomon, S., Plattner, G.-K., Knutti, R., & Friedlingstein, P. (2009). Irreversible climate change due to carbon dioxide emissions. *Proceedings of the National Academy of Sciences*, *106*(6), 1704–1709. https://doi.org/10.1073/pnas.0812721106

Tu, Q., Hase, F., Schneider, M., García, O., Blumenstock, T., Borsdorff, T., Frey, M., Khosrawi, F., Lorente, A., Alberti, C., Bustos, J. J., Butz, A., Carreño, V., Cuevas, E., Curcoll, R., Diekmann, C. J., Dubravica, D., Ertl, B., Estruch, C., … Torres, C. (2022). Quantification of CH_4 emissions from waste disposal sites near the city of madrid using ground- and space-based observations of COCCON, TROPOMI and IASI. *Atmospheric Chemistry and Physics*, *22*(1), 295–317. https://doi.org/10.5194/acp-22-295-2022

USEPA. (2016). *Inventory of U.S. greenhouse gas emissions and sinks: 1990–2014* (EPA 430-R-16-002). United States Environmental Protection Agency, Washington, DC. https://www.epa.gov/ghgemissions/inventory-us-greenhouse-gas-emissions-and-sinks-1990-2014

Vicente-Hernández, Í., Martínez, F., & Blanco, G. (2023). Rabbits or refuse? Landfill use and relevance as a food source for an increasing wintering population of the red kite. *Diversity*, *15*(6), 704. https://doi.org/10.3390/d15060704

Wang, Y., Fang, M., Lou, Z., He, H., Guo, Y., Pi, X., Wang, Y., Yin, K., & Fei, X. (2024). Methane emissions from landfills differentially underestimated worldwide. *Nature Sustainability*, *7*(4), 496–507. https://doi.org/10.1038/s41893-024-01307-9

Acknowledgments

Working on this master's thesis has been a rewarding journey, and I am deeply grateful for the support and guidance I received along the way. Many people have contributed to this achievement, and I would like to acknowledge them for their invaluable assistance and encouragement. In particular, I would like to thank:

- Prof. Dr. André Butz for the opportunity to carry out this thesis, for his supervision, for always being available to discuss my data and findings, and for providing me with helpful ideas and feedback.
- Prof. Dr. Werner Aeschbach for serving as my second examiner.
- Dr. Marvin Knapp for taking me by the hand from the very beginning of this thesis, for introducing me to everything I needed to know to work with the camera and its data, and for always being approachable to answer any of my questions.
- Prof. Dr. André Butz, Dr. Marvin Knapp, and Dr. Cristina Prados Román for carrying out major parts of the campaign planning.
- The Madrid campaign group: Alberto Álvaro Díaz, Adela Collado Rodríguez, Lukas Häffner, Dr. Marvin Knapp, Dr. Christian Mielke, and Louisa-Marie Rüther for collecting all the data without which this thesis would not have been possible. For making a great team to work with in the field, for being a great group to spend time with, and for making these two weeks exceptionally fun and memorable.
- Lukas Häffner, Johannes Hiller, Dr. Benedikt Löw, Dr. Marvin Knapp, Leonie Olivia Scheidweiler, and Moritz Sindram for engaging in fruitful discussions about the matched filter and my data analysis.
- Ralph Kleinschek for being an excellent and very knowledgeable solver of my hardware problems.
- Lukas Pilz for readily helping me with programming and software problems, and for providing me with a lot of knowledge about good coding practices.
- Lukas Weis for answering all the tiny questions I had when I was very new to the Atmo group.

- Dr. Harikrishnan Charuvil Asokan, Lukas Häffner, Ralph Kleinschek, Dr. Marvin Knapp, Dr. Benedikt Löw, Marlene Matzke, Kenneth Murai von Bünau, Dr. Cristina Prados Román, Louisa-Marie Rüther, Leonie Olivia Scheidweiler, Moritz Sindram, and Lennart Thiemann for proofreading this thesis and providing me with helpful feedback.
- Everyone with whom I shared an office for creating a great work environment, motivating me to work, and also being available for fun conversations: Ken, Jana, Lukas W., Louisa, Silke, Pia, Johannes, Vincent, Helge, Sebastian, Marlene, Nic, and Joeri.
- The entire Atmo group for being so welcoming and supportive, and for enjoyable lunch breaks playing Doppelkopf.
- The personnel of the Mancomunidad del Sur for their support regarding our measurements at the Pinto landfill.
- The GFZ German Research Centre for Geosciences, Nicole Köllner and colleagues, for their support with the measurement equipment.
- The German Aerospace Center DLR, and in particular Veronika Gstaiger, for providing aerial photographs of the Pinto landfill.
- The AERONET PIs José María San Atanasio, Ana Díaz Rodríguez, and Aleksander Pietruczuk for their effort in establishing and maintaining the Madrid and Racibórz AERONET sites.
- The state of Baden-Württemberg through bwHPC and the German Research Foundation (DFG) through grant INST 35/1597-1 FUGG.
- The data storage service SDS@hd supported by the Ministry of Science, Research and the Arts Baden-Württemberg (MWK) and the German Research Foundation (DFG) through grant INST 35/1503-1 FUGG.

Statement on the Use of AI-Based Tools

Within my thesis, I used the following AI-based tools:

DeepL Write by DeepL SE (https://deepl.com/write)

Le Chat by Mistral AI SAS (https://chat.mistral.ai)

Grammarly by Grammarly, Inc. (https://grammarly.com)

Tabnine by Tabnine Ltd. (https://tabnine.com)

Perplexity AI by Perplexity AI, Inc. (https://perplexity.ai)

To improve the phrasing of this thesis and check it for grammatical correctness, I used DeepL Write, Le Chat, and Grammarly.

For code completion, I used Tabnine. Le Chat and Perplexity AI were used for simple programming tasks and help in debugging code.

All AI-generated output has been checked for correctness.

Selbstständigkeitserklärung

Ich versichere, dass ich diese Arbeit selbstständig verfasst habe und keine anderen als die angegebenen Quellen und Hilfsmittel benutzt habe.

Heidelberg, den 2. August 2025